Influence of Ionization Quenching in Plastic Scintillator Particle Dosimetry

Christensen, Jeppe Brage

Publication date:
2019

Document Version
Publisher's PDF, also known as Version of record

Influence of Ionization Quenching in Plastic Scintillator Particle Dosimetry

Jeppe Brage Christensen

Center for Nuclear Technologies
Technical University of Denmark

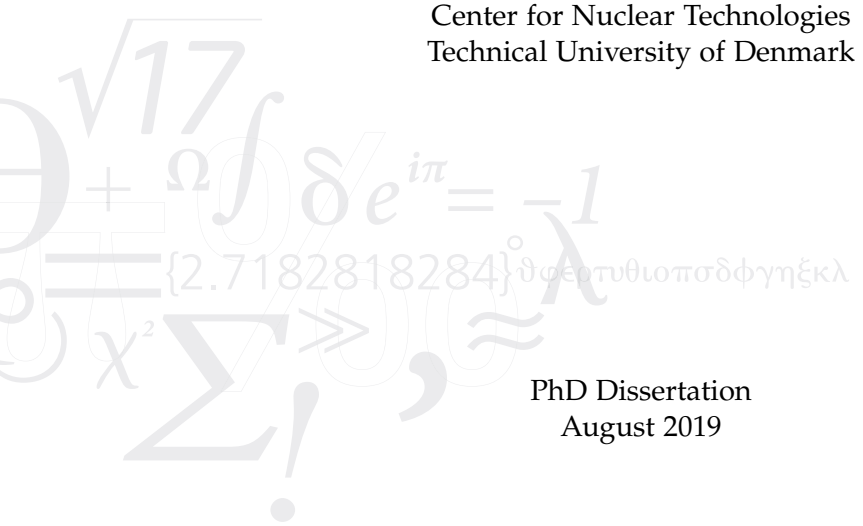

PhD Dissertation
August 2019

Supervised by:

Senior scientist Claus Erik Andersen, head of the dosimetry section at DTU Nutech, Technical University of Denmark, Roskilde, Denmark.

Professor Cai Grau, Department of Oncology and Danish Centre for Particle Therapy, Aarhus University Hospital, Aarhus, Denmark.

The work presented in this thesis was co-financed by the Danish Cancer Society (Kræftens Bekæmpelse).
The development of the calorimeter was supported by the Danish Council for Independent Research (grant FTP, DFF–4184-00151).

This thesis is typeset with LaTeX and the `memoir` class by the author. The bibliography was typeset with `biber`. The figures are created with TikZ and `PGF` plots.

DTU Nutech
Center for Nuclear Technologies
Technical University of Denmark
Risø Campus, Frederiksborgvej 399
DK-4000, Roskilde, Denmark

Danish Cancer Society

Preface

Radiotherapy is an essential part of cancer treatments and the number of particle therapy centres has been rapidly increasing worldwide the past decade. The aim of this work is to further the use of plastic scintillation detectors (PSDs) in particle dosimetry with a focus on protons. This PhD project started in August 2016 and is related to the establishment of the Danish Centre for Particle Therapy (DCPT) in Aarhus, Denmark, which was inaugurated in the beginning of 2019.

The majority of the present work was conducted at DTU Risø under supervision of Claus E. Andersen, who has a remarkable ability to always find a solution to any kind of problem. The feasibility of experiments was generally assessed with Monte Carlo methods and tested in photon and electron beams at Risø due to a lack of protons at clinically relevant energies in Denmark until 2019. Several people assisted with the experiments at Risø, especially Grichar V. Santurio and Lars R. Lindvold. Most of the experiments at Risø were subsequently repeated in the scanning proton beam at the Swedish proton therapy center, Skandionkliniken, in Uppsala during 2017–18. I fortunately got to spend the hours in the lab at Skandionkliniken with Håkan Nyström, Erik Almhagen, and Liliana Stolarczyk who always helped with the irradiations and improved our experiments.

I later got the chance to substitute the Danish 2018–19 winter with a warmer Texan version during a four month stay in the group of Sam Beddar at the MD Anderson Cancer Center. I had the pleasure to work with Fahed Alsanea in Houston who introduced me to liquid scintillators.

The first treatment with protons in Denmark took place at DCPT in January 2019, just before my return to Risø, and a proton beam line was suddenly nearby. I joined a fruitful collaboration with Anne Vestergaard (DCPT) in 2018 with the objective of mapping ion recombination in scanning ion beams, which continued at DCPT in February 2019. Anne and Christian Søndergaard came to our aid again by the end of July 2019 as Claus and I were in urgent need of proton beam time to test the newly assembled graphite calorimeter.

I appreciate the many advices from Gustavo Kertzscher who also shared his expertise regarding the assembling of fibre-coupled PSDs. Niels Bassler is fortunately still involved in my projects and has always been available for feedback and ideas. I owe Jakob Hjørringgaard—to whom I dedicate any remaining typos—plenty of hours of work as he almost voluntarily proofread my drafts.

I acknowledge the entire Stack Exchange Network and its users for saving me from numerous hours of debugging and I am indebted to the person who maintained the coffee machine in building 201 at Risø. Also a great thanks to Anders, Alexander, and the Risø Cycling Club for suffering the notorious headwind with me during our commute from Copenhagen and to *Han Solo* camp (you know who you are) for wasting much of my leisure time.

Thanks to Bent, Nicolò, Claire, Ashkhen, and Jakob for discussing the world situation on a daily basis during the lunch, to Xiao Xiao and Raju from the office, Martin and Magdalena from the wrong office, Pia and Merete for their assistance and patience, and everybody else who helped me during my time at Risø.

If this thesis is accepted, I dedicate it to Matilde for travelling the world with me. If not, I dedicate it to the DTU office for Legal and Contracts.

Risø, August 14, 2019
Jeppe Brage Christensen

Abstract

Radiotherapy has been used for more than a century to treat cancer and an important part of the treatment with radiation is to direct a sufficiently high dose to the tumour without damaging the neighbouring tissue. The recently commissioned Danish Centre for Particle Therapy (DCPT) features a scanning proton beam that enables the delivery of a more conformal dose to the tumour than what can be achieved with conventional radiotherapy.

The present work investigates the use of plastic scintillation detectors (PSDs) coupled to optical fibres as a radiation detector in ion beams. PSDs are attractive for particle dosimetry and particularly *in vivo* measurements due to a prompt response, small size, and near water-equivalence. It is demonstrated how a single PSD can detect the spots in a scanning beam and measure the scattering of the spots.

The conversion from the PSD luminescence response into an energy deposition is, however, challenging. The PSDs exhibit a non-linear response—termed ionization quenching—to charged particles. A theoretical formalism is developed in order to predict and correct the quenched luminescence of PSDs irradiated with ions at clinically relevant energies. The algorithm is based on fundamental scintillator properties and track structure theory and validated relative to a gas-filled detector and Monte Carlo simulations. The combination of a theoretical quenching model, experiments, and Monte Carlo calculations provides a new insight into the quenching of plastic scintillators.

Finally, a graphite calorimeter was constructed and subsequently tested in the proton beam at DCPT. The portable calorimeter showed an excellent stability and reproducibility and enables the measurement of more accurate quenching corrections for PSDs.

Resumé (Danish)

Stråleterapi har i mere end ét århundrede været anvendt til kræftbehandlinger. En essentiel del af behandlingen sigter mod at afsætte tilstrækkelig stor energi i tumoren mens det omkringliggende væv skånes. Dansk Center for Partikelterapi (DCPT) åbnede i Aarhus i indeværende år, hvor man for første gang i Danmark kan behandle tumorer med protoner. Protoner muliggør mere konforme strålefelter, end hvad der normalt kan opnås med konventionel stråleterapi, og minimerer således risikoen for stråleinducerede følgevirkninger.

Denne afhandling omhandler brugen af optiske fibre påsat plastikscintillatorer til at detektere protonstråler. Scintillatorerne er små og har en hurtig responstid, og muliggør dermed en måling af protonerne med stor nøjagtighed. Det vises hvordan en enkelt plastikscintillator kan detektere en protonstråle i rum og tid og bruges til at beregne spredningen af protoner i vand med stor præcision.

Lyset fra scintillatorerne er dog svært at omsætte til en måling af energiafsættelsen, da det opsamlede lys ikke er proportionelt med den afsatte energi, men varierer med protonernes fart. En numerisk algoritme er derfor udviklet til at korrige det målte lys. Algoritmen er baseret på fundamentale scintillatoregenskaber og den radiale energifordeling i protonernes spor gennem plastikken. Metoden er valideret med scintillator- og et ionkammermålinger i forskellige protonstråler. Kombineret med Monte Carlo-simuleringer udgør algoritmen et nyt værktøj, og har bl.a. givet ny viden om lysudsendelsen i et blandet strålefelt.

Slutteligt blev et grafitkalorimeter udviklet, der kan måle den afsatte energi via en temperaturstigning i grafitten med meget høj nøjagtighed. Kalorimetret blev afprøvet på DCPT og muliggør målinger af bedre korrektioner af lysudsendelsen i plastikscintillatorer under protonbestråling.

List of Publications

Publications in peer-reviewed journals constituting the basis of this thesis:

I **Christensen JB**, Almhagen E, Nyström H and Andersen CE (2018).
Quenching-free fluorescence signal from plastic-fibres in proton dosimetry: understanding the influence of Čerenkov radiation.
Published in: Physics in Medicine and Biology **63** 065001
DOI: 10.1088/1361-6560/aaafad

II **Christensen JB** and Andersen CE (2018).
Relating ionization quenching in organic plastic scintillators to basic material properties by modelling excitation density transport and amorphous track structure during proton irradiation.
Published in: Physics in Medicine and Biology **63** 195010
DOI: 10.1088/1361-6560/aadf2d

III **Christensen JB** and Andersen CE (2019).
Applications of amorphous track structure models for correction of ionization quenching in organic scintillators exposed to ion beams.
Published in: Radiation Measurements **124** 158–162
DOI: 10.1016/j.radmeas.2019.01.003

IV **Christensen JB**, Almhagen E, Stolarczyk L, Vestergaard A, Bassler N and Andersen CE (2019).
Ionization quenching in scintillators used for dosimetry of mixed particle fields.
Published in: Physics in Medicine and Biology **64** 095018
DOI: 10.1088/1361-6560/ab12f2

Manuscripts outside the scope of this work:

V **Christensen JB**, Almhagen E, Stolarczyk L, Liszka M, Hernandez GG, Nørrevang O and Vestergaard A
Mapping of initial and general recombination in scanning proton beams.
Enclosed manuscript to be submitted.

VI Markovic N, **Christensen JB** and Pommé S
On photon-photon coincidence standardisation of ^{125}I
Manuscript in preparation.

VII Lange SL, **Christensen JB**, Lindvold LR and Jepsen PU
Direct injection of ultrashort electron bunches into a solid material using terahertz-driven electron field emission
Manuscript in preparation.

Popular science contribution:

- **Christensen, JB**.
Partikelterapi: Fysikkens bidrag til en mere skånsom kræftbehandling.
www.videnskab.dk [In Danish, published March 30, 2018].

Oral presentations at conferences and workshops related to the content:

- 5th Øresund Workshop on Radiotherapy, Helsingborg 2017
- DOTSKAN Workshop, Therapy with scanned ion beams, Uppsala 2017
- NEUDOS 13, Neutron and Ion Dosimetry Symposium, Krakow 2017
- WONP–NURT Medical Physics conference, Havana 2017
- Radiation Detection in Medical Physics, Aarhus 2018
- Luminescent Detectors and Transformers of Ionizing Radiation, Prague 2018
- 7th Øresund Workshop on Radiotherapy, Helsingborg 2019
- ESTRO 38, Milan 2019
- International Symposium on Standards, Applications and Quality Assurance in Medical Radiation Dosimetry, Vienna 2019
- Solid State Dosimetry 19, Hiroshima, 2019

List of Abbreviations

ATSM	amorphous track structure model
CSDA	continuous slowing down approximation
DCPT	Danish Centre for Particle Therapy
DoF	degrees of freedom
FDM	finite difference method
FEM	finite element method
FWHM	full width at half maximum
HCP	heavy charged particle
LET	linear energy transfer
PDE	partial differential equation
PMMA	polymethyl methacrylate
PMT	photo multiplier tube
PSD	plastic scintillation detector
QA	quality assurance
QCF	quenching correction factor
RBE	relative biological effectiveness
RDD	radial dose distribution
RE	relative effectiveness
SOBP	spread-out Bragg peak
SW	solid water
TPS	treatment planning system
WET	water equivalent thickness

Contents

Part I

Summary Report

Chapter 1

Introduction

Cancer is the leading cause of death at ages below 70 years in the developed[1] countries (Bray et al. 2018), and is globally responsible for about 1 in 6 deaths or 9.6 million per year (WHO 2019). Cancer is often treated with a combination of surgery, chemotherapy, and radiation therapy. The field of therapy using ionizing radiation emerged shortly after Röntgen (1895) discovered the x-rays, and Despeignes (1896) is traditionally credited with the first cancer treatment with x-rays as well as the first publication on radiation therapy (Wagener 2009). Emil Grubbé assembled the first x-ray tube outside Europe in 1896—remarkably at a homeopathic clinic (Grubbé 1949)—and pioneered the cancer treatment. Ironically, Grubbé's intense work with the x-ray tube exposed him to high doses and he went through almost 100 operations to remove cancers. The use of radiation therapy to deliver a lethal radiation dose to the diseased cancer tissue while sparing the healthy surrounding tissue has ever since experienced a remarkable development.

1.1 Particle therapy

Bragg and Kleeman (1904) demonstrated how heavy charged particles (HCPs)[2] deposit most of the energy at the end of the trajectory, referred to as the Bragg-peak. Decades later and after the invention of the cyclotron, Wilson (1946) proposed how the Bragg-peak could be utilised to deliver a more conform dose deposition to the tumour than what can be achieved with conventional photon or electron radiation. Hence, Wilson demonstrated that particle therapy has the potential to reduce the risk of acute radiation damages as well as long term effects. The first patient was subsequently treated with proton therapy in 1954 in Berkeley, California.

The first treatment with protons in Europe took place at a research beam line in 1957 in Uppsala, Sweden, which decades later would host the Swedish proton therapy centre (Skandionkliniken) where most the of the experimental work in

[1] Albeit the term *developed* is misleading as no countries are *undeveloped* (Rosling 2018).
[2] A HCP shall in this work refer to a proton as well as heavier ions.

this thesis was conducted. The modern particle therapy era began in 1990 in California as the first hospital-based proton beam line was commissioned at Loma Linda. The number of cancer therapy centres using protons and heavier ions has increased rapidly throughout the past decade with 92 particle centres in operation and 46 under construction as of July 2019 (PTCOG 2019). The Danish Centre for Particle Therapy (DCPT) treated the first patient with protons in Denmark on January 29, 2019.

1.1.1 Quality assurance and *in vivo* dosimetry

The process of accurately delivering radiotherapy is complex and involves a variety of fields ranging from radiobiology over treatment planning simulations to machine quality assurance (QA). The QA of a specific treatment plan is complicated and often involves pre-irradiation of gas-filled ionization chambers. Ionization chambers remain the golden standard for reference dosimetry in protocols such as the IAEA TRS-398 (Andreo, Burns, Hohlfeld, et al. 2000) or AAPM TG-51 (Almond et al. 1999) and are essential to establish traceability to standards. However, ionization chambers are difficult—if feasible at all—to use for *in vivo* dosimetry. *In vivo* dosimetry, where the dose delivery is monitored directly during a treatment, has the potential to reduce mistakes and improve treatments (Tanderup et al. 2013). Patient specific QA is however not commonly applied in clinics, partly due to a lack of detectors suitable for *in vivo* dosimetry.

1.1.2 Scintillation detectors

Scintillators, materials emitting light upon excitation by ionizing radiation, are attractive for *in vivo* dosimetry with a prompt response and small (often sub-millimetre) sizes (Beddar, Mackie, and Attix 1992b,c; Kertzscher et al. 2014). Scintillators coupled to optical fibres guide the emitted photons to a photodetector, typically a charge-coupled device or a photo multiplier tube (PMT), where the amount of light is related to the energy deposition in the scintillating material.

Andersen et al. (2009) demonstrated the use of radio luminescence to *in vivo* brachytherapy dosimetry in Denmark. MD Anderson Cancer Center successfully tested a plastic scintillation detector (PSD) system for *in vivo* dosimetry on five patients treated with intensity-modulated radiotherapy for prostate cancer (Wootton et al. 2014). Recently, Aarhus University Hospital started using an end-to-end scintillator system to monitor brachytherapy (Johansen et al. 2018).

The use of PSDs enable measurements and validations of the delivery of complex particle therapy plans: the PSDs are almost perturbation free and allow online measurement of the radiation (Sibolt et al. 2017), as opposed to the large ionization chambers or integrating alanine pellets. The PSDs can be fitted into anthropomorphic phantoms or used for *in vivo* dosimetry with animals.

The PSDs possess several attractive advantages but the energy dependence remains a drawback. The high linear energy transfer (LET) from a HCP is in radiobiology known to cause an elevated relative biological effectiveness (RBE) relative to photons (Grassberger and Paganetti 2011; Sørensen, Overgaard, and Bassler 2011). The situation is reversed in dosimetry where the non-proportional PSD response is problematic for *in vivo* measurements for particle therapy and requires careful corrections. The non-linear detector response related to high ionization densities is termed ionization quenching and is the main focus of this thesis.

1.1.3 Ionization quenching

Most of the present work is related to the development of a general and robust algorithm to calculate and correct the quenching in PSDs irradiated with ion beams. Quenching corrections are generally conducted with PSD measurements relative to a non-quenching detector, typically an ionization chamber. The quenching is mapped for different beam qualities where the Monte Carlo calculated LET is used to model and correct the quenching. Ionization chambers, on the other hand, suffer from ionic recombination which is difficult to correct for as the LET and dose-rate differ greatly from the entrance region to the Bragg peak[3] or even more complexly in spread-out Bragg peaks (SOBPs). The issue of ion recombination is avoided with the use of calorimetry where the radiation induced heat is related to the absorbed dose. The last part of the thesis is dedicated to the design and use of a graphite calorimeter to accurately measure the dose and correct the quenching in PSDs.

The present work investigates how fibre-coupled PSDs are applicable to extract information about the LET, dose, and beam structure in proton beams with a brief outlook to heavy ion beams.

[3]The problem with ion recombination in scanning beams is treated in paper V, outside the scope of this thesis.

1.2 Thesis outline

Part I contains the summary report:

Chapter 2 treats the physics of fibre-coupled PSDs in regard to radioluminescence and Čerenkov radiation induced in both the scintillator and the optical fibre. It is demonstrated how a single optical fibre can extract beam spot sizes and the spot deposition time in a scanning pencil proton beam. The chapter is based on results presented in paper I.

Chapter 3 accounts for the stopping of charged particles through matter and models the local ionization density through track structure theory. The ionization density is necessary to model the detector response and is traditionally related to the quenching of scintillators.

Chapter 4 presents the open-source code `ExcitonQuenching` as detailed in paper II. `ExcitonQuenching` relies on fundamental properties as the scintillation decay time and light yield and applies track structure theory to predict the quenching in HCP tracks. `ExcitonQuenching` is validated in proton beams and used to probe the temporal structure of quenching in PSDs.

Chapter 5 validates the use of `ExcitonQuenching` to compute the ionization quenching in HCP tracks which is the focus of paper III. The quenching in a PSD exposed to a proton beam is scrutinised in paper IV with an emphasis on the quenching in mixed fields, nuclear fragments, and the information provided by energy spectra.

Chapter 6 investigates the design and use of a graphite calorimeter with a small and large graphite core. The calorimeter is operated in a quasi-adiabatic mode and designed to minimize the heat losses. The use of a small graphite core facilitates a direct comparison between the quenched PSD response and the graphite calorimeter.

Part II contains the publications I through IV and manuscript V.

Chapter 2

Scintillation

Scintillation is the emission of light in certain materials by the passage of a particle depositing energy. Scintillators are categorized as inorganic or organic according to the mechanism of light production and atomic composition (Birks 1964). The present chapter gives a brief introduction to organic scintillators based on literature reviews and selected results from paper I.

2.1 Physical scintillation mechanism

Organic scintillators consist of aromatic organic molecules where the ring shaped chains of carbon atoms bonded to hydrogen atoms (hydrocarbons) are responsible for the luminescence properties. Each carbon atom in the s^3p^1 configuration forms a weak π-bond with a neighbouring carbon atom and three σ-bonds with two adjacent carbon atoms and a hydrogen atom as shown in figure 2.1(a). The π-bonds parallel to the plane of the molecule in figure 2.1(b) form a ring where the π-electrons from each carbon atom is free to move as outlined in figure 2.1(c).

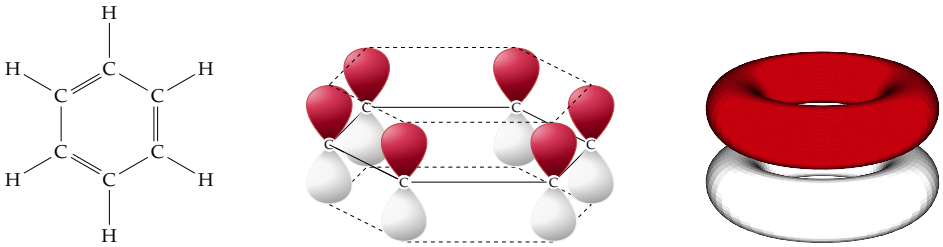

Figure 2.1: (a) Diagram of the planar benzene molecule. (b) The π-electrons responsible for the luminescence of the molecule constitute the parallel rings illustrated in (c) where they are free to move. Adapted from Birks (1964).

The π-electrons are bound less tightly to the parent carbon atom than the localized σ-electrons. Hence, less energy is required for transitions in the π-electronic absorption band and excitation and de-excitation of the π-electrons are generally responsible for the luminescence. The photons emitted following energy deposition by ionizing radiation are typically in the UV range with a relatively short absorption length reducing the applicability of the scintillators. Other scintillating materials are typically mixed and cast into an amorphous material to avoid complete absorbance, as the different scintillators are chosen to ensure that the UV photons first are converted into blue photons and occasionally further converted into green photons in a wavelength shifter (Lindvold, Beierholm, and Andersen 2010). Even though each conversion decreases the number of photons, it allows more optical photons to be transmitted through the amorphous scintillator.

The energy levels of an organic molecule with π-electronic structure is shown in figure 2.2. The difference in energy levels between the ground state (S_0) and the first excited singlet state (S_1) is typically around 3 eV to 4 eV whereas the vibrational states, subdividing each singlet and triplet state, are spaced of the order of 0.15 eV (Beddar and Beaulieu 2016). A typical plastic scintillator emits of the order of 8000 photons MeV^{-1} which corresponds to a conversion efficiency around 2 %, where most of the deposited energy is lost as heat.

The average thermal energy at room temperature about 25 meV is much smaller than the spacing between the vibrational states (Knoll 2010), and the majority of the organic molecules will occupy the S_{00} state. The energy absorption is shown in figure 2.2 with solid arrows to the left. Excited higher-lying singlet electronic states are on a picosecond time scale de-excited to the S_1 singlet state as depicted with vertical, dashed arrows.

The fluorescence is emitted in transmissions from the S_{10} state to one of the S_{0x} electronic vibrational states illustrated with solid arrows pointing downward. The fluorescence decay time τ is of the order of a few nanoseconds for most organic scintillators and enables an excellent temporal resolution for particle dosimetry. The lifetime of the triplet states is characteristically much longer than the singlet states. Some excited singlet states can make a transition to the triplet states through inter-system crossing. The delayed light emission, termed phosphorescence, from the triplet states occurs at longer wavelengths than the fluorescence emission. However, some molecules in the triplet state may be thermally excited back to the singlet states and de-excite normally through (delayed) fluorescence (Knoll 2010).

While excitations of π-electrons thus may be followed by emission of optical photons, the ionization of π- or σ-electrons normally renders the molecule incapable of scintillation. The ionization events generate free radicals which can emit UV photons via recombination, undergo photochemical reactions, or non-radiative de-excitation. The energy spent on excitation of a σ-electron is similarly dissipated as heat rather than via scintillation (Birks 1964).

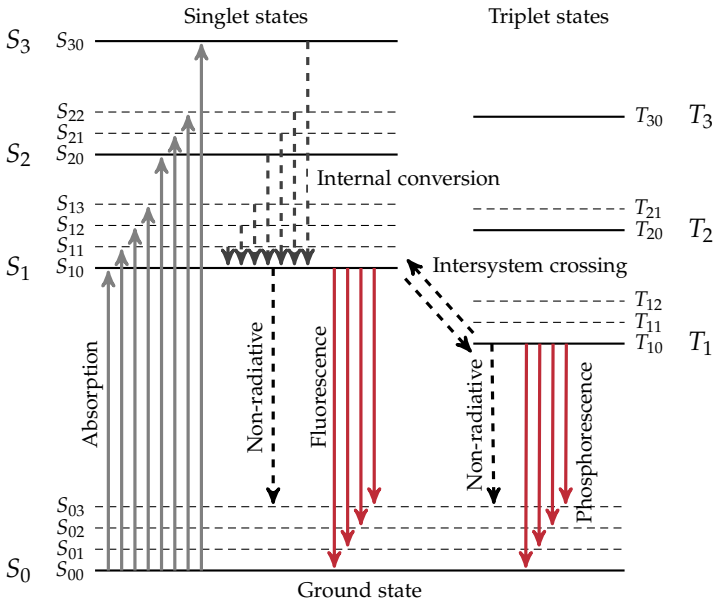

Figure 2.2: Jablonski diagram of the energy levels of an organic molecule with π-electron structure where the vibrational states are arbitrarily scaled. Redrawn from Birks (1964).

2.2 Fibre-coupled plastic scintillators

Organic PSDs are commercially available in sizes from point sources to huge bulk volumes. The combination of good water-equivalence, a prompt scintillation response, and a sub millimetre size enables particle dosimetry with great temporal and spatial resolution (Beddar, Mackie, and Attix 1992b,c). One way to use a PSD is by coupling it to an optical fibre: the in-house built ME-40 system (Beierholm et al. 2011) is unique with a fast (kHz) sampling rate. The system consists of a plastic scintillator coupled to an optical fibre with optical glue as shown in figure 2.3 and is used extensively throughout this work. The light is guided from the PSD through the optical fibre to two PMTs. The following sections present the results published in paper I.

The optical fibre typically consists of a 480 µm diameter polymethyl methacrylate (PMMA) core (refractive index $n = 1.49$) and fluorinated polymer ($n = 1.40$) cladding with a 500 µm outer diameter as outlined in figure 2.3. A black polyethylene jacket protects the core and cladding from external light.

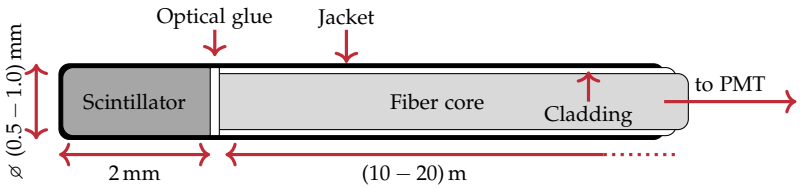

Figure 2.3: A plastic scintillator coupled to an optical fibre. The optical photons emitted from the scintillator are guided to a PMT.

2.2.1 Volume averaging

The PSD volume with a diameter of 0.5 mm to 1 mm water equivalent thickness (WET) cause a slight volume averaging over steep dose gradients. The effect of volume averaging along the central axis of a 100 MeV proton beam was investigated in paper IV. The signal volume averaging was shown to be negligible provided the analysis was truncated at the 80 % distal dose point.

2.3 Optical fibre cable

The optical fibre is a scintillating material capable of undergoing molecular transitions in the singlet manifold based on the PMMA core, although the scintillation efficiency is much lower than polystyrene based plastics. Consequently, fluorescence induced in the optical fibre may contaminate the PSD signal. Čerenkov radiation emitted in the optical fibre and transmitted to the PMT may similarly give rise to a background signal (Beddar, Mackie, and Attix 1992a). The optical fluorescence and Čerenkov photons induced in the optical fibre are collectively termed the *stem signal* and subject to investigation below.

2.3.1 Luminescence in the optical fibre

Jang et al. (2012) published measurements of the response of an optical PMMA-based fibre exposed to both a pristine proton Bragg peak and a SOBP in a water phantom. The optical fibre was placed perpendicular to the beam direction and the PMMA luminescence response was compared to an ionization chamber measurement along the same axis. The response of the optical fibre was in perfect agreement with the ionization curve along the central beam axis, indicating the luminescence signal from the optical fibre is proportional to the energy deposition. The conclusion that scintillators exhibit a linear response in proton beams contradicts decades of experiments (Birks 1964; Beddar and Beaulieu 2016) and, furthermore, Jang et al. (2012) concluded the optical signal generated in the optical fibre to be Čerenkov radiation rather than fluorescence.

The emission of optical Čerenkov photons decreases with the speed of the primaries, i.e. the Čerenkov emission is expected to be inversely correlated with the LET as a function of depth in the water phantom rather than matching the ionization curve perfectly.

The remarkable experimental results and conclusions by Jang et al. (2012) motivated an investigation of the emission and guidance of optical photons through an optical fibre exposed to a proton beam. The following section investigates the origin of the optical photons in an optical fibre irradiated with proton at different energies followed by a discussion on fluorescence and Čerenkov radiation.

2.3.2 Spot scanning proton beam

The luminescence arising from a PMMA-based optical fibre exposed to a spot scanning proton beam was investigated at the Skandion Clinic, Uppsala. The optical fibre was placed in the 10 cm × 10 cm field consisting of 41 × 41 spots as sketched in figure 2.4(a) and connected to the ME-40 system. The fibre was irradiated with 180 MeV protons at different depths in a water phantom which enabled a comparison of the optical response relative to a reference ionization curve along the central beam axis. An example of the PMT signal at 6 cm depth is shown in figure 2.4(b).

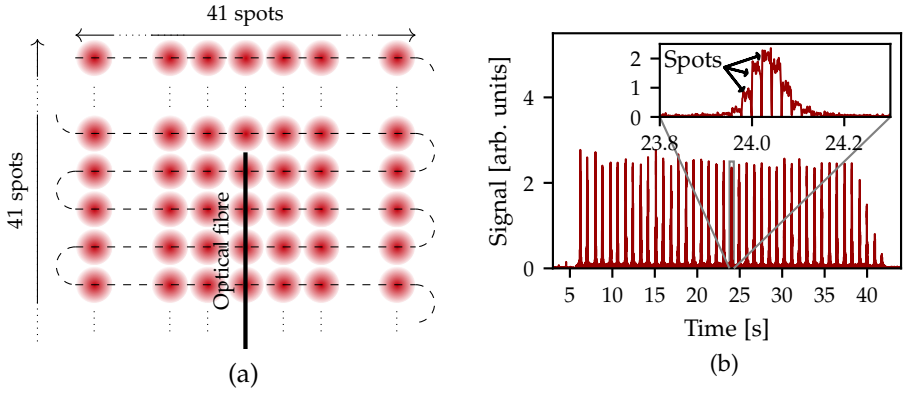

Figure 2.4: The pencil beam scans (dashed line) over the optical fibre (solid line) in (a) which gives rise to a signal detected at the PMT. The PMT signal is shown in (b) where each peak corresponds to a horizontal scan line in (a). Figures from paper I.

Each time the proton beam scans horizontally across the fibre in figure 2.4(a) it gives rise to an optical signal measured by the PMT in (b). An insert in figure 2.4(b) shows the structure of a single scan line where approximately 8 of the 41 spots were detected. The optical fibre did not reach through the entire

field as illustrated in figure 2.4(a) and measured in (b): the signal after 37 s is fading as the beam no longer scans directly across the fibre.

The prompt fibre response and the 0.5 mm fibre diameter enable an extraction of the beam spot size and the spot deposition time: the insert in figure 2.4(b) indicates an average spot deposition time of 21 ms in agreement with the actual 22 ms spot deposition time extracted from the cyclotron log-files. Furthermore, a Gaussian fit to the spots shown in the insert gives a full width at half maximum (FWHM) of $\simeq$ 10 mm in agreement with FWHM $=$ 9.4 mm measured with an ionization chamber array.

The measurement of the response of the optical fibre as a function of depth in the water phantom is compared to the ionization curve of a Roos-type ionization chamber in figure 2.5. The optical fibre response is obtained from an integration over the PMT signal as a function of water depth. The PMMA phantom wall slows the protons from the fixed horizontal research beam line causing the observed range shift in figure 2.5, where a 180 MeV proton in water otherwise would have a continuous slowing down approximation (CSDA) range of 21.7 cm.

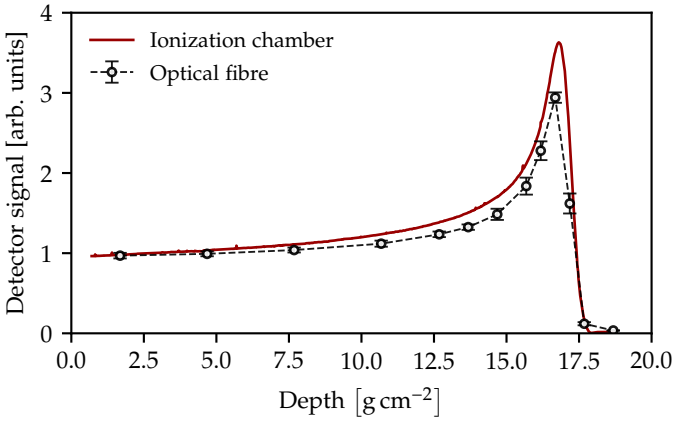

Figure 2.5: The luminescence response of the bare optical fibre ($k = 2$ statistical uncertainties) and an ionization chamber measurement in a water phantom irradiated with 180 MeV protons. Figure adapted from paper I.

The optical fibre response in figure 2.5 exhibits a non-linear response relative to the ionization chamber measurement—i.e. it quenches in line with traditional measurements and conclusions (Birks 1964). The relative amount of Čerenkov radiation and fluorescence constituting the origin of the optical photons in the PMMA fibre during proton irradiations is to be investigated next.

2.4 Čerenkov radiation

Čerenkov radiation (Čerenkov 1934, 1937; Frank and Tamm 1937) is the coherent emission of optical photons by charged particles exceeding the phase velocity of light in a dielectric medium. The energy threshold E_{TH} depends on the refractive index n as

$$E_{\mathrm{TH}} = m_0 c^2 \left(\frac{1}{\sqrt{1 - n^{-2}}} - 1 \right), \tag{2.1}$$

where m_0 is the rest-mass of the charged particle and c the speed of light in vacuum (Jelley 1958). The energy thresholds for electrons in PMMA and water are cf. eq. (2.1) 178 keV and 264 keV, respectively. Protons are too heavy to directly emit Čerenkov radiation in clinically relevant proton beams but liberate electrons above E_{TH}. Specifically, a proton of rest-mass m_p may transfer an energy (Andreo, Burns, Nahum, et al. 2017)

$$\mathcal{W}_{\max} = \frac{2 m_e c^2 \beta^2 \gamma^2}{1 + 2\gamma \frac{m_e}{m_p} + \left(\frac{m_e}{m_p} \right)^2} \approx \begin{cases} 2 m_e c^2 \beta^2 \gamma^2 & \text{for} \quad \gamma m_e \ll m_p \\ \gamma m_p \beta^2 c^2 & \text{for} \quad \gamma \to \infty \end{cases}, \tag{2.2}$$

to an electron with rest-mass m_e. As usually,

$$\gamma = \frac{1}{\sqrt{1 - \beta^2}}, \qquad \text{and} \qquad \beta = \frac{v}{c}, \tag{2.3}$$

where v denotes the speed of the proton. Hence, a proton above 80 MeV in PMMA and 115 MeV in water may liberate electrons above E_{TH} or via nuclear interactions at lower energies (Helo et al. 2014). The angular dependency of Čerenkov radiation constitutes—besides the emission spectrum—a crucial difference compared to the fluorescence. Fluorescence is emitted isotropically whereas Čerenkov photons are emitted at an angle

$$\theta = \arccos \left(\frac{1}{\beta n} \right). \tag{2.4}$$

relative to the particle track. The number of optical photons $\mathrm{d}N$ emitted per unit length $\mathrm{d}x$ in the spectral region $\lambda_1 < \lambda_2$ by a particle with charge z is given by the famous Frank-Tamm equation

$$\frac{\mathrm{d}N}{\mathrm{d}x} = 2\pi z^2 \alpha \left(\frac{1}{\lambda_1} - \frac{1}{\lambda_2} \right) \sin^2 \theta, \tag{2.5}$$

where $\alpha = 1/137$ is the fine structure constant (Jelley 1958). Equation (2.5) gives $\mathrm{d}N/\mathrm{d}x \simeq 470 z^2 \sin^2 \theta$ photons cm^{-1} for the optical window $\lambda_1 = 400$ nm

and $\lambda_2 = 700\,\text{nm}$. The number of fluorescence photons emitted from an electron in a typical PSD with light yield per energy deposition $\approx 8000\,\text{photons}\,\text{MeV}^{-1}$ and LET $\approx 2\,\text{MeV}\,\text{cm}^{-1}$ thus greatly exceeds the number of Čerenkov photons. The emission angle and transmission trough an optical fibre may nonetheless favour the guidance of Čerenkov radiation.

The relative intensity of Čerenkov radiation is approximately proportional to the frequency as given by eq. (2.5), i.e. dominated by blue light in contrast to a fluorescence spectrum with a characteristic spectral peak (Therriault-Proulx et al. 2013). The energy loss due to Čerenkov radiation at therapeutic relevant energies is typically $< 0.1\,\%$ of the energy spent in soft collisions (Andreo, Burns, Nahum, et al. 2017).

2.4.1 Čerenkov spectra

The emission angle θ in eq. (2.4) affects the number of Čerenkov photons emitted within the acceptance cone of the optical fibre as outlined in figure 2.6, where the optical fibre is placed at an angle φ with respect to the beam axis. Detailed analyses on the emission and guidance of Čerenkov radiation in multicladding fibres are available (Beddar, Suchowerska, and Law 2004) but out of the scope of this work.

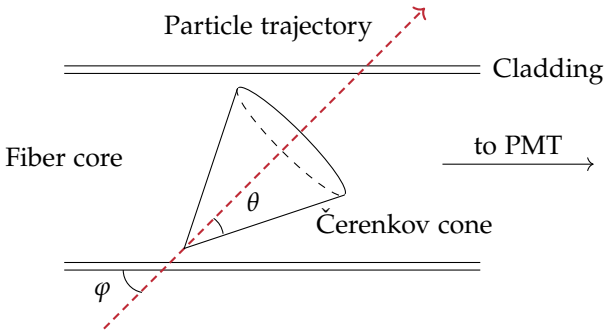

Figure 2.6: A charged particle traversing the optical fibre at an angle φ relative to the fibre axis emits Čerenkov radiation at an angle θ with respect to the trajectory (dashed line). The fraction of Čerenkov photons guided to the PMT is highly angle dependent.

An example of measurements of Čerenkov and fluorescence spectra is shown in figure 2.7. The spectra are convolved with the transmission profile of the optical fibre cable where the PMMA core absorbs most light below 380 nm. The figure includes two spectra obtained with 20 MeV electron irradiations at $\varphi_1 = 45°$ and $\varphi_2 = 135°$ relative to the optical fibre as defined in figure 2.6.

The Čerenkov emission angle for 20 MeV electrons in PMMA is about $\theta \simeq 47.8°$ cf. eq. (2.4). Consequently, φ_1 favours the guidance of Čerenkov photons

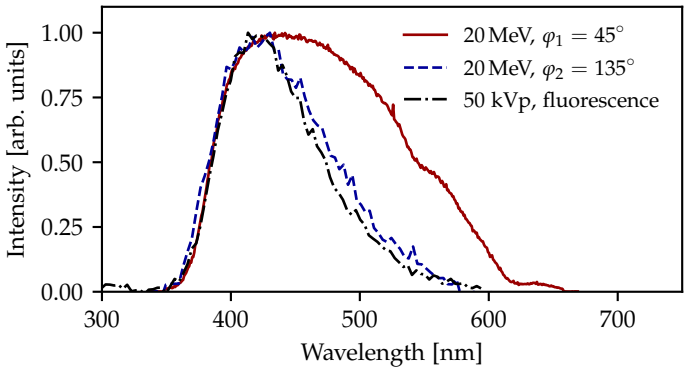

Figure 2.7: An optical fibre irradiated at two angles φ_1 and φ_2 with 20 MeV electrons and with an kV x-ray source below the Čerenkov energy threshold. Figure from paper I.

towards the PMT while φ_2 corresponds to the case where the Čerenkov photons are emitted towards the dead fibre end and are absorbed.

The fluorescence spectrum is obtained with an in-house constructed 50 kVp x-ray source which is unable to generate Čerenkov radiation. The coinciding spectra obtained with φ_2 and 50 kVp shows that Čerenkov photons are absorbed at such an angle in contrast to φ_1 which is completely dominated by Čerenkov radiation.

2.4.2 Monte Carlo calculations

The optical fibre in figure 2.3 was implemented in the Monte Carlo code `Geant4` (Agostinelli et al. 2003) without the scintillator. `Geant4` enables a simulation of both the emission and guidance of Čerenkov and fluorescence photons in the optical fibre.

The `Geant4` model with the fluorescence spectrum measured in figure 2.7 and the transmission profile of PMMA was assessed against measurements in an electron beam. The agreement between the Monte Carlo model results and the Čerenkov measurements is described in paper I and validates the use of the Monte Carlo model to simulate the emission and guidance of optical photons in a proton beam.

2.4.3 Čerenkov radiation in a proton beam

The `Geant4` simulations of the emission and guidance of Čerenkov and fluorescence photons in an optical fibre placed perpendicular to the central beam axis are shown in figure 2.8(a). The number of emitted Čerenkov photons per

primary proton exceeds the number of guided fluorescence photons at the entry channel. Most of the Čerenkov photons are however absorbed in the fibre rather than guided through the fibre. The primary protons are at about half the CSDA range unable to liberate electrons above the Čerenkov threshold E_{TH}. The Čerenkov emission following nuclear interactions is isotropic but negligible relative to the fluorescence signal.

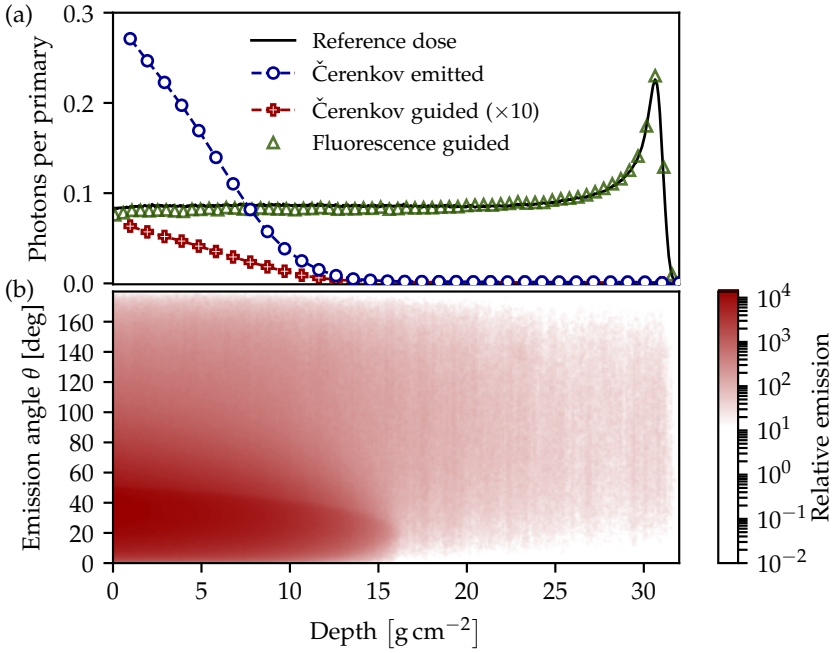

Figure 2.8: `Geant4` simulations of fluorescence and Čerenkov photon during irradiation with 225 MeV protons. (a) The emission and guidance of Čerenkov and fluorescence photons in an optical fibre placed perpendicularly to the beam direction. The number of Čerenkov photons guided through the fibre per primary (crosses) is in the figure multiplied by 10 for visibility. (b) The Čerenkov emission angle in a 225 MeV proton beam in water. The angle is given relative to the beam direction. Figures modified from paper I.

The Čerenkov emission angle θ along the central beam axis is shown in figure 2.8(b). An optical fibre placed with its axis at an angle $\approx 20°$ relative to the beam direction would favour the guidance of the Čerenkov photons. An optical fibre placed perpendicular to the beam (as in Jang et al. (2012)) will absorb most of the emitted Čerenkov photons as evident from figure 2.8(a).

The fluorescence distribution in figure 2.8(a) matches the ionization curve as the non-linear response is unaccounted for in the `Geant4` implementation. The

neutron activation cross section is low for plastics (Otuka et al. 2014) and the Čerenkov radio peak at the Bragg peak (Helo et al. 2014) is negligible relative to fluorescence. Hence, it can be concluded that the optical signal—reported to be Čerenkov radiation by Jang et al. (2012)—is fluorescence.

2.5 Stem signal in a proton beam

The conclusion that fluorescence dominates the signal in an optical fibre can be transferred to the PSD where approximately the same amount of Čerenkov radiation per volume is guided: the scintillation light yield in the PSD is much larger than the light yield of the optical fibre and the Čerenkov in the PSD is negligible.

Archambault et al. (2006) investigated the fluorescence and Čerenkov stem signal in a proton beam. The stem signal is concluded to be negligible at clinically relevant energies for PSD sizes comparable to the one presented in figure 2.3. Consequently, the stem signal during proton beam irradiations is not removed as it would have to be for electron and photon beams.

The reason for the non-linear response of scintillators is scrutinized in the following chapters.

Chapter 3

Radial dose distributions

The luminescence response of an HCP traversing a scintillator is related to the local energy deposition which excites the molecules. Some response models rely solely on the LET of the particle whereas other models account for the radial dose distribution (RDD) through track structure theory. The track structure of an HCP has historically been modelled in several ways, typically with a distinction between stochastic or amorphous approaches.

Stochastic models track the emission of each secondary particle and the tortuous electron paths (see e.g. Ogawa, Yamaki, and Sato (2018)) often result in local ionization densities consisting of dense cluster regions.

Amorphous track structure theory models the RDD as a continuous distribution, i.e. averaged over all energy depositions (Katz and Varma 1991). Amorphous track structure models (ATSMs) were developed in radiobiology (Butts and Katz 1967) to model the cell response during HCP irradiations, and are still used to model the RBE in particle therapy. The following sections relate the stopping of HCPs in matter to ATSMs in order to predict the scintillation response.

3.1 Stopping of swift particles

Shortly after Rutherford (1911) concluded that the atom is made up of a heavy nucleus surrounded by electrons, Thomson (1912) and Bohr (1913, 1915) developed theories of particle penetration of matter from first principles. The total mass stopping force[1] in a medium of density ρ is given as

$$\frac{S_{\text{total}}}{\rho} = \frac{S_{\text{elec}}}{\rho} + \frac{S_{\text{nuc}}}{\rho} + \frac{S_{\text{rad}}}{\rho}, \tag{3.1}$$

where the terms on the right-hand side denote the contributions from electronic, nuclear, and radiative interactions, respectively. The radiative energy loss (bremsstrahlung interactions) for HCPs is negligible relative to the energy

[1] This work adheres to the use of *stopping force* rather than *power*. Sigmund (2000) and ICRU (2005) emphasize *power* would be more appropriate for an energy loss per unit time.

lost through multiple inelastic scattering processes (ICRU 1993). The energy lost through elastic collisions with atomic nuclei, where the primaries are deflected considerably, contributes less than 1 % to the total energy loss above the orbital velocities of the atomic electrons in the target (ICRU 2005; Andreo, Burns, Nahum, et al. 2017). Elastic nuclear interactions in light ion beams should generally only be considered below 0.1 MeV/n (Cucinotta, Nikjoo, and Goodhead 1999), i.e. below the energy region of interest in this work. Hence, with the focus on 1 MeV to 250 MeV protons in water-equivalent materials, the stopping force is approximated as $S_{\text{total}} \approx S_{\text{elec}}$.

The classically derived electronic stopping force equation by Bohr (1913, 1915) was extended to a quantum mechanical version by Bethe (1930) and later to a relativistic version by Møller (1932)[2] and Bethe (1932)[3]. The stopping of a swift HCP takes on the form

$$\frac{S_{\text{elec}}}{\rho} \simeq \frac{e^4}{4\pi\epsilon_0^2 m_e c^2} N_{\text{A}} \frac{Z}{A} \frac{z^2}{\beta^2} \left(\ln \frac{2m_e c^2 \beta^2}{I} - \ln(1-\beta^2) - \beta^2 - \frac{C(\beta)}{Z} - \frac{\delta(\beta)}{2} \right), \tag{3.2}$$

where I is the mean ionization potential, N_{A} is Avogadro's constant, Z/A is the ratio of the number of protons to the number of nucleons in the target material, z is the charge of the projectile with relative speed β, and ϵ_0 the vacuum permittivity. The term outside the brackets is related to the electron density of the target material and the speed and charge of the projectile, while the terms $-\ln(1-\beta^2) - \beta^2$ account for the relativistic stopping force rise (Sigmund 2006, 2014).

The shell correction term $C(\beta)/Z$ contributes a few percent for energies below 10 MeV and corrects that the projectile no longer has a velocity much larger than that of the atomic electrons in the target material. The shell correction is the same for all charged particles for a given velocity β and in the present work extracted from data published by Emfietzoglou et al. (2009). The density-effect correction $\delta(\beta)$ due to polarizations in condensed media affects the stopping force in eq. (3.2) less than 0.1 % for protons below 800 MeV (Andreo, Burns, Nahum, et al. 2017) and is henceforth omitted.

3.1.1 Stopping in compounds

The stopping force in plastic compounds of n constituents is approximated by Bragg's additive rule (Bragg and Kleeman 1905) as

$$\frac{S}{\rho} = \sum_{i=1}^{n} w_i \left(\frac{S}{\rho} \right)_i, \tag{3.3}$$

[2] Whose 24-page paper became the shortest dissertation in Denmark (Ekstrabladet 1932), and it has been argued that the *Bethe-Møller* equation would be a more appropriate name for eq. (3.2).

[3] Møller submitted his manuscript to *Annalen der Physik* the day before Bethe submitted his to *Zeitschrift für Physik*. The latter journal had a faster review process and Bethe alone was credited with the formula (Kragh 1992).

where w_i is the weight fraction and $(S/\rho)_i$ the mass stopping force of the ith constituent. Similar weightings are applied to calculate the mean ionization energy, atomic number and weight of the compound (Attix 1986).

A note on stopping force libraries

Several libraries and codes are available for stopping force data for particles and materials (Paul 2010): the National Institute of Standards and Technology provides tables for the stopping force and range (`STAR`) of protons (`PSTAR`) and alpha particles (`ASTAR`) from 1 keV to 1 GeV. Tables for heavier ions are available through `MSTAR` (Paul and Schinner 2001, 2002), `SRIM` (Ziegler, Ziegler, and Biersack 2010) or the open-source code `libdEdx` (Toftegaard et al. 2014). The electronic mass stopping force for protons and heavier ions in plastic scintillators is in this work computed with eq. (3.2) rather than loaded from the libraries in order to include various scintillator compounds.

3.1.2 The linear energy transfer

The mass electronic stopping force in eq. (3.2) is the average rate of energy loss where some collisions may liberate electrons with enough kinetic energy to deposit energy far from the primary particle trajectory—a feature covered in the next section on track structure theory. The scaling of the mass stopping force with the mass density ρ equals the linear stopping force. The idea of a local energy deposition, in contrast to total energy deposition, leads to the introduction of the restricted linear electronic stopping force L_Δ, called the linear energy transfer (LET). The L_Δ excludes energy losses between Δ and the maximum energy transferred to a particle $\mathcal{W}_{\max}$ from eq. (2.2) (ICRU 1970). The unrestricted LET, for the case where $\Delta \to \mathcal{W}_{\max}$, equals the linear electronic stopping force S_{elec} and is used throughout this work.

LET calculations

The LET at a point in the radiation field may consist of contributions from several particles and energies. Averaging the LET at a single point is possible in multiple ways where the two most common approaches include the fluence-averaged (or track-averaged) LET (LET_Φ) and the dose-averaged LET (LET_D). The intensity of the fluence spectrum φ for a particle with energy E and linear stopping force S at a point x enables a calculation of the arithmetic mean as

$$\text{LET}_\Phi(x) = \frac{\int_0^\infty \varphi(E,x)\, S(E)\, \mathrm{d}E}{\int_0^\infty \varphi(E,x)\, \mathrm{d}E}, \tag{3.4}$$

whereas the dose-averaged LET is given by

$$\text{LET}_\text{D}(x) = \frac{\int_0^\infty \varphi(E,x)\, S^2(E)\, \mathrm{d}E}{\int_0^\infty \varphi(E,x)\, S(E)\, \mathrm{d}E}. \tag{3.5}$$

The Monte Carlo scoring of LET_Φ and LET_D in ion beams relies on the recommendations in Cortés-Giraldo and Carabe (2015), where the stopping force S for the LET_D calculations is extracted from stopping force tables in the Monte Carlo code.

The energy deposition and LET are scored in `Geant4` version 10.3 (Agostinelli et al. 2003). An example of the `Geant4` calculations of the dose deposition and the difference between LET_Φ and LET_D along the central beam axis is shown in figure 3.1 using the beam parameters (Almhagen et al. 2018) for the 100 MeV scanning proton beam at the Skandion Clinic, Uppsala.

The analyses of the detector response as a function of energy deposition and LET are in the following parts truncated at the 80 % distal dose point to avoid too large biases and uncertainties (Bortfeld 1997). For instance, Grzanka, Ardenfors, and Bassler (2018) demonstrated how the LET scored as either LET_Φ or LET_D and by in- or excluding secondary particles may vary 300 % in a clinically relevant proton SOBP.

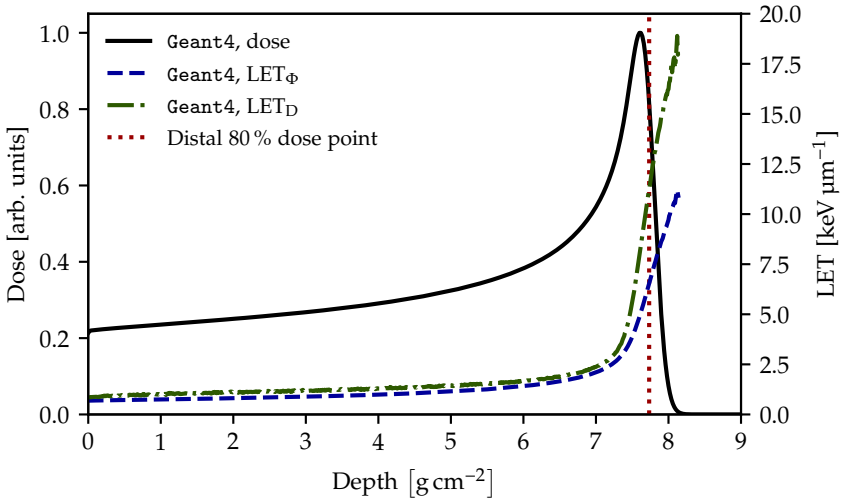

Figure 3.1: The `Geant4` simulations of the dose deposition (left ordinate) and LET_Φ and LET_D (right ordinate) in water irradiated with a 100 MeV proton beam.

Grün et al. (2018) recently demonstrated that the LET_D often is an insufficient predictor for the RBE. Bertolet et al. (2019) recommend a new approach to calculate the LET based on track segmentation. This work adheres to the use of the arithmetic mean of the LET spectrum—the LET_Φ—as a quenching predictor rather than LET_D or other means of LET scoring but includes the LET_D in calculations for comparison. The LET will henceforth be given as the LET in

water unless otherwise stated.

3.2 Amorphous track structure theory

Several analytical ATSMs have successfully applied to model the response of detectors or biological systems to HCP irradiations (Chatterjee and Schaefer 1976; Hansen and Olsen 1984; Kiefer and Straaten 1986; Katz and Varma 1991; Scholz and Kraft 1996; Geiß, Krämer, and Kraft 1998). The approaches generally distinguish between a dense core region smaller than $10^{-6}\,\mathrm{g\,cm^{-2}}$ enclosed by a penumbral region.

3.2.1 Amorphous track structure models

The amount of energy deposition in the core and penumbral regions varies between the ATSMs but the integral over the RDD equals the mass stopping force, i.e.

$$\int_0^{2\pi}\int_0^{r_\mathrm{pen}} D(r)\, r\,\mathrm{d}r\,\mathrm{d}\theta = \frac{\mathrm{LET}}{\rho}, \tag{3.6}$$

where r_pen is the penumbral radius corresponding to the range of the most energetic electrons. The range of the electrons fluctuate and the mean range r_pen is normally approximated as a power function of the kinetic energy of the ion E (Scholz and Kraft 1996; Geiß, Krämer, and Kraft 1998), whereas Chatterjee and Schaefer (1976) suggested a penumnral radius in water as

$$r_\mathrm{pen} = 0.768\,\mu\mathrm{m\,MeV^{-1}}E - 1.925\,\mu\mathrm{m\,MeV^{-0.5}}\sqrt{E} + 1.257\,\mu\mathrm{m} \tag{3.7}$$

and a radius of the core region as

$$r_\mathrm{core} = \beta\, r_\mathrm{min}, \quad \text{for} \quad r_\mathrm{min} = 11.6\,\mathrm{nm}, \tag{3.8}$$

ensuring $r_\mathrm{core} \to r_\mathrm{min}$ for $\beta \to 1$. All ions at a given velocity β liberate electrons with the same energy and the track radius r_pen in eq. (3.7) is thus independent of the charge of the ion.

The ATSM for ions given by Chatterjee and Schaefer (1976), henceforth referred to as the Chatterjee-Schaefer model, models the RDD as

$$D(r) = \begin{cases} \dfrac{D_0}{r_\mathrm{core}^2}\,(1+C) & \text{for} \quad r < r_\mathrm{core} \\ C\dfrac{D_0}{r^2} & \text{for} \quad r_\mathrm{core} \le r \le r_\mathrm{pen} \\ 0 & \text{for} \quad r > r_\mathrm{pen} \end{cases} \tag{3.9}$$

with the parameters

$$D_0 = \frac{\mathrm{LET}}{2\pi\rho} \quad \text{and} \quad C = \left[2\ln\left(\sqrt{e}\,\frac{r_{\mathrm{pen}}}{r_{\mathrm{core}}}\right)\right]^{-1} \tag{3.10}$$

satisfying eq. (3.6). Another popular ATSM due to Scholz and Kraft (1996) included in this work is given in the appendix of paper II.

The Chatterjee-Schaefer model is plotted for two proton tracks in water in figure 3.2 along with the Scholz-Kraft model and the purely numerical calculations of Wang and Vassiliev (2017) relying on `Geant4`-DNA (Chauvie et al. 2006). The numerical ATSM model by Wang and Vassiliev (2017) is presented for protons between 10 MeV to 100 MeV in water and not used any further as the traditional analytical ATSMs enable a general implementation to model the RDD for a given HCP and plastic composition.

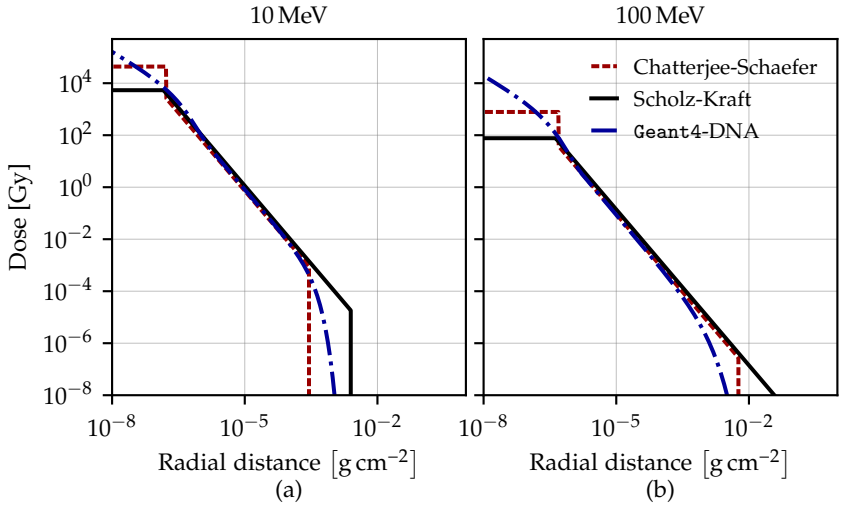

Figure 3.2: Radial dose distributions using the analytical Chatterjee-Schaefer ATSM (dashed line) in eq. (3.9), the Scholz-Kraft ATSM (solid line), and `Geant4`-DNA calculations (dashed-dotted line) for a (a) 10 MeV and (b) 100 MeV proton in water. The `Geant4`-DNA calculations are extracted from Wang and Vassiliev (2017).

An integration over the Chatterjee-Schaefer model in eq. (3.9) from the track centre to r_{core} shows that more than half the energy is deposited in the core region. The Scholz-Kraft model consists of a less dense core region and is henceforth used to investigate the response of PSDsirradiated with ion beams. Furthermore, the continuous transition from the core to the penumbral region

in the Scholz-Kraft model, as opposed to the Chatterjee-Schaefer model, enables a more stable numerical investigation of the detector response.

3.3 Relative effectiveness

Different detectors and in particular scintillators exhibit different responses in the same beam quality. The relative effectiveness (RE) is a useful quantity to compare the responses between two detectors, and can be be defined as

$$\eta = \frac{R_{\text{ref}}(D_0)}{R_{\text{PSD}}(D_0)}, \tag{3.11}$$

where R_{PSD} is the response of a PSD to a dose D_0 and R_{ref} is the response of a reference detector under the same radiation conditions. The reference detector is an ionization chamber or a graphite calorimeter in this work. η is approximately constant for high-energy photons—which enables the use of scintillators for *in vivo* dosimetry during brachytherapy—but varies with the LET and RDD in ion beams. The RBE is a similar quantity in radiobiology where its value for protons relative to high-energy photons has been a catalyst for debates (Paganetti et al. 2002).

The non-linear response of a PSD is in the following referred to as *quenching* and the RE in (3.11) is henceforth referred to as the quenching correction factor (QCF) to avoid confusion with saturation effects.

Chapter 4

Ionization Quenching

Two ions with the same LET but different atomic number will exhibit different radial dose distributions (RDDs) and ionization densities. Hence, the LET alone is an insufficient quenching predictor and the RDD is required to model the local energy density and predict the detector response. This chapter relates ATSMs and scintillator properties to the luminescence response for PSDs in ion beams based on results in papers II and III.

4.1 Physics of quenching

The luminescence response of a PSD (BCF-12, Saint-Gobain, France) irradiated with a 100 MeV proton beam is compared to the ionization curve along the central beam axis in figure 4.1. The PSD response is normalized at the entry channel and has been subject to a peak match relative to the ionization curve simulated with `Geant4`.

While the luminescence response essentially is proportional to the energy deposition at the entry channel, the ionization quenching is evident as the track narrows along the beam axis resulting in an increasing energy density. Numerous models and algorithms have been suggested in the past century to correct the quenching in inorganic and organic scintillators. The quenching is traditionally corrected as a function of the LET while few models account for the variations in the RDD.

4.1.1 Physical mechanism

It has for decades been established that the luminescence response depends on the local energy density (Murray and Meyer 1961) but the reason *why* the increasing local energy density reduces the light emission remains a challenge. Early explanations suggested that quenching is caused by a saturation effect where all scintillation centres in the region were excited and the excess energy thus would be lost through non-radiative means as depicted in figure 2.2. However, Blue and Liu (1962) showed that a relative increase in the number

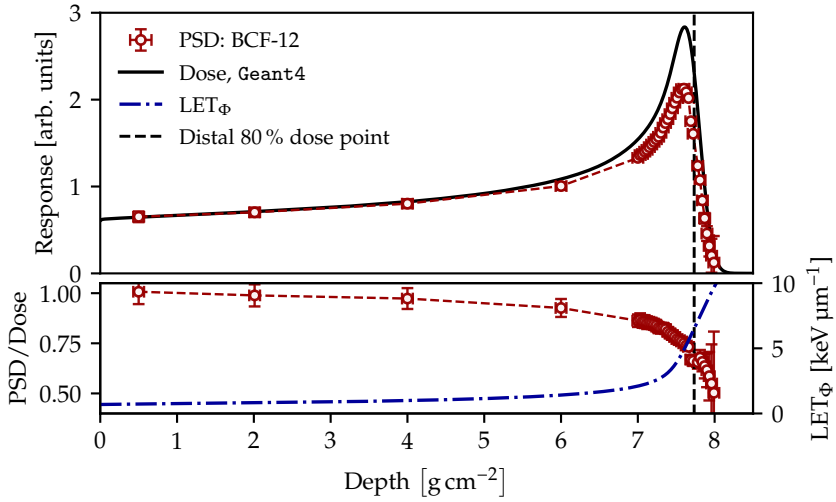

Figure 4.1: The `Geant4` simulated ionization curve and measured PSD response in a 100 MeV proton beam in water. The ratio of the PSD response to the energy deposition is shown in the figure below on the left ordinate (connected with a dashed line), where the LET$_\Phi$ is plotted for reference with a dot-dashed line on the right ordinate.

of scintillation centres did not decrease the relative amount of quenching for a specific beam quality and excluded that explanation.

Another approach was suggested by Galanin and Chizhikova (1958) where the ionization density in an ion track is said to rapidly increase the temperature in the ionization column, causing the energy to be lost through thermal dissipation rather than via fluorescence. The idea to understand quenching as a thermal flash never received much attention in Western journals[1] and the model is—at best—challenging to apply for quenching corrections.

Traditional quenching explanations pivot about a reduction of the primary excitation efficiency, i.e. that several processes compete about the energy and more energy is lost through ionic recombination or to radiation damages at high energy density cases than for low energy density cases. Birks (1951, 1964) suggested that the reduction of the excitation efficiency occurs through ionization and excitation damages to the molecules.

The present work assumes—in line with Birks (1964) and Beddar and Beaulieu (2016)—that ionization quenching can be categorized according to the number of molecules involved in the quenching process. Specifically, a

[1] Albeit the approach of modelling the quenching as a thermal process can have received significant attention in Soviet-based journals.

case involving j molecules is referred to as a j-molecular quenching interaction. The focus here is mainly limited to unimolecular ($j = 1$) and bimolecular ($j = 2$) quenching interactions due to the moderately low LET of protons. Unimolecular quenching is the case where a single excited molecule undergoes a non-radiative de-excitation whereas bimolecular quenching is an interaction between two excited molecules where at least one of them is de-excited in a non-radiative way. Hence, the events involving more than one excited molecule is inherently dependent on the ionization density and the particle RDD.

Kallmann and Brucker (1957) showed that ionization quenching in organic scintillators mainly occurs within the first nanoseconds and thus precedes the main emission with typical decay times $> 1\,\mathrm{ns}$. The exact mechanisms for the occurrence of ionization quenching remain unexplained (Birks 1964; Beddar and Beaulieu 2016). Since the exact mechanisms of quenching on a microscopic scale cannot be accounted for, the following sections treat the quenching on a macroscopic scaled modelled by the local densities of excited states. The system of excited and de-excited states is assumed to be reversible in order to model the interaction between excited states.

4.1.2 The Birks formalism

The historically most successful approach to correct the ionization quenching in scintillator dosimetry is the semi-empirical Birks formalism (Birks 1951). The model corrects the luminescence signal $\mathrm{d}L$ per unit length $\mathrm{d}x$ with a quenching correction factor (QCF) as

$$\frac{\mathrm{d}L}{\mathrm{d}x} = A\,\frac{\mathrm{LET}}{\mathrm{QCF}}, \tag{4.1}$$

where A is the light yield per deposited energy of the scintillator. The QCF is typically taken to be a first- or second-order function of the LET as

$$\mathrm{QCF}_{\mathrm{Birks}} = 1 + kB \cdot \mathrm{LET}, \tag{4.2a}$$

$$\mathrm{QCF}_{\mathrm{Chou}} = \mathrm{QCF}_{\mathrm{Birks}} + C \cdot \mathrm{LET}^2, \tag{4.2b}$$

where kB is the Birks parameter and C the extra model parameter due to Chou (1952). Eq. (4.1) in combination with the QCF given as in eq. (4.2a) is termed the Birks model, whereas the use of eq. (4.1) with the extended version eq. (4.2b) with an additional free parameter is referred to as the Chou model. Birks (1964) investigated both models and concluded that eq. (4.2b) with $C = 0$, thereby reducing it to eq. (4.2a), gave the best fit to data. Torrisi (2000), on the other hand, reported that the Chou model with $C \neq 0$ gave a more accurate correction for high-LET. The contradicting conclusions reflect the large experimental uncertainties at the Bragg peak along with both LET scoring biases and uncertainties in HCP beams.

Experimentally calculated QCFs are plotted as a function of the `Geant4` calculated LET_Φ in figure 4.2. The QCFs are determined as the ratio of an ion-

ization chamber measurement to the PSD response in figure 4.1. The Birks and Chou models in eq. (4.2a) and (4.2b) are fitted to the data to estimate the quenching as a function of the LET_Φ. The residuals between the two models and the data in figure 4.2 are generally within 2.5 % at the plateau region but increases to 5 % near the Bragg peak around 5 keV µm^{-1}. The results illustrate the uncertainties related to LET calculations where even a 1 mm PSD positioning error may result in more than 10 % response discrepancy.

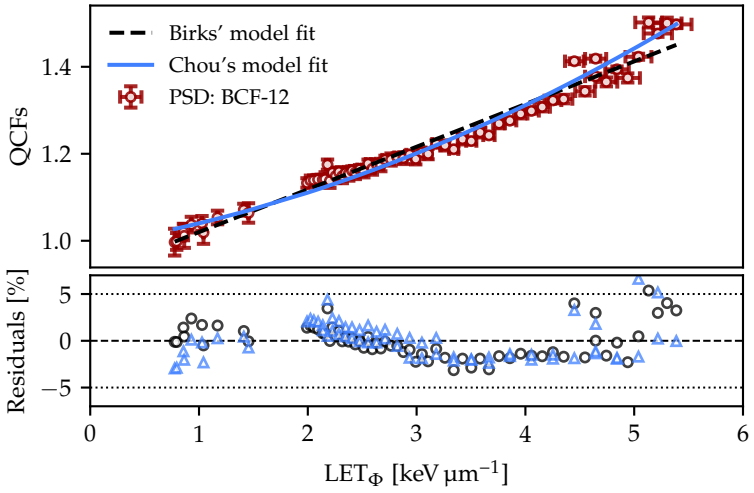

Figure 4.2: Quenching correction factors calculated as the ratio of the ionization chamber response to the PSD response in figure 4.1 plotted as a function of the LET_Φ. The analyses are truncated at the 80 % distal dose point. The Birks model in eq. (4.2a) and Chou model in eq. (4.2b) are fitted to the data. The lower figure shows the residuals of the experimental data to the Chou model (triangles) and the Birks model (circles).

The Birks and Chou quenching model parameters kB and C obtained from the fits to the data in figure 4.2 can subsequently be used to predict the quenching in that particular PSD and ion beam. The quenching corrected PSD measurements using the Birks and Chou parameters from figure 4.2 are shown in figure 4.3 where the dose and quenched PSD response are shown for reference.

The Chou model provides with its additional free parameter slightly more accurate (or similar) QCFs than the Birks model does and the quality of the corrections may be compared in numerous ways to compensate for the different number of free parameters. The sum of squared errors scaled with the degrees of freedom (DoF) for each model is investigated in paper IV for three PSDs in proton beams. The overall conclusion corresponds to the mixed statements of

Birks (1964) and Torrisi (2000): the additional parameter in the Chou model does only occasionally provide a better fit to the data than the Birks model.

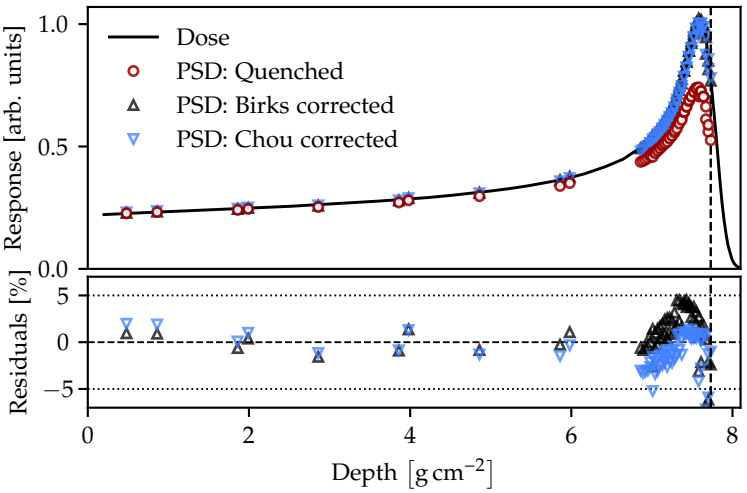

Figure 4.3: The measured quenched response in the BCF-12 PSD compared to the `Geant4` simulated dose along the central axis. The quenching has been corrected with the QCFs from the Birks model (Birks corrected) and with the Chou model (Chou corrected) showed with lines in figure 4.2. The dashed vertical line indicates the 80 % distal dose cut-off.

Both the Birks and Chou quenching models are able to correct the quenched signal to within a few percent once the model parameters have been experimentally determined as illustrated in figure 4.3. However, both models fail to account for the RDD and hence erroneously predict the same QCF for two ions with different RDDs if the LET is the same. Furthermore, the kB and C are parameters to be determined experimentally for each ion and each scintillator type, while the temporal quenching dependence is unaccounted for. Recently, Boivin et al. (2016) showed how the Birks model breaks down in low-energy photon beams. Other popular quenching correction models include modifications to the Birks model as suggested by Voltz et al. (1966) but suffer from the same issues.

Michaelian and Menchaca-Rocha (1994) proposed a luminescence quenching model relying on an ATSM accounting for the backscatter of electrons into the dense ionization column region. Nonetheless, their model is cumbersome to apply, contain free parameters to be estimated from fits to data, and is unable to quantify the temporal behaviour of the quenching (Michaelian, Menchaca-Rocha, and Belmont-Moreno 1995).

4.1.3 The Blanc formalism

A different approach was taken by Blanc, Cambou, and Lafond (1962, 1964) which, in contrast to the Birks model, enables an inclusion of amorphous track structure theory. The Blanc formalism includes a kinematic quenching model where the density of excited states $n(\vec{r}, t)$ (henceforth referred to as excitons) is related to quenching and fluorescence through

$$\frac{\partial n}{\partial t} = \underbrace{D\nabla^2 n}_{\text{diffusion}} - \underbrace{pn}_{\text{fluorescence}} - \underbrace{kn}_{\text{unimol.}} - \underbrace{\alpha n^2}_{\text{bimol.}} - \underbrace{\sum_{j=3}^{\infty} h_j n^j}_{j\text{-mol.}}, \tag{4.3}$$

where $D \simeq 5 \times 10^{-4}\,\mathrm{cm^2\,s^{-1}}$ is the exciton diffusion constant (Kallmann and Brucker 1957; Birks 1964). p and k denote the rates of fluorescence and unimolecular quenching, respectively, while αn, and $h_j n^{j-1}$ are the probabilities per time for bi- and j-molecular de-excitation. Birks (1964) gives $p + k = \tau^{-1}$ where τ is the characteristic scintillator decay time and further estimates $\alpha = 3.2 \times 10^{-9}\,\mathrm{cm^3\,s^{-1}}$. Eq. (4.3) can mathematically be reduced to the semi-empirical Birks model in eq. (4.2a) assuming only unimolecular de-excitation (Birks 1964). The temporal component in eq. (4.3) enables an investigation of temporal structure of ionization quenching treated in the following section 4.3.

While Blanc, Cambou, and Lafond (1962) present the model in eq. (4.3) without a derivation, the quenching model may be interpreted and derived from a physical point of view: the flow of excitons $\vec{J}(\vec{r}, t)$ in the ionization column is depending on the concentration gradient as

$$\vec{J}(\vec{r}, t) = -D\nabla n(\vec{r}, t). \tag{4.4}$$

The exciton flow is related to the exciton losses through fluorescence emission and quenching interactions via the equation of continuity as

$$\frac{\partial n(\vec{r}, t)}{\partial t} + \vec{\nabla} \cdot \vec{J}(\vec{r}, t) = g(\vec{r}, t), \tag{4.5}$$

where the sink term g is a series given as

$$g(\vec{r}, t) = -\sum_{j=1}^{\infty} h_j n(\vec{r}, t)^j \qquad \text{with} \quad h_1 = \tau^{-1} \quad \text{and} \quad h_2 = \alpha \tag{4.6}$$

which is equivalent to the Blanc model in eq. (4.3) when the equations are combined.

The following work focuses on eq. (4.3) where the series is truncated at $j = 2$, i.e. including bimolecular quenching as the highest term.

Recombination analogy

A set of equations similar to (4.4)–(4.5) was suggested by Thomson (1899) to model the ion recombination in an ionization chamber, where (4.4) would be modified to include a drift term in the presence of an external electric field. The recombination equations were famously solved[2] by Jaffé (1913) to calculate the initial ion recombination in a parallel-plate ionization chamber irradiated with HCPs. Jaffé, several decades before amorphous track structure theory gained popularity, relied on a Gaussian-style ATSM, where the ion recombination sink-term was modelled as $g(n_c) \simeq \gamma n_c^2$ for a recombination parameter γ and charge carrier density n_c.

The ion recombination term hence is identical to the bimolecular quenching term in eq. (4.3) and reflects the similar situations: ion recombination cannot be simulated on a microscopic scale as the recombination cross sections are too uncertain. Quenching cannot be predicted on the microscopic scale as the underlying mechanisms are yet to be understood. Hence, both problems are treated on a macroscopic scale in terms of the number of charge carriers or excited states per volume.

4.1.4 Excitation densities

An ion traversing the PSD with a light yield per deposited energy A ionizes and excites the molecules along its track: the exciton density in a segment of the track is estimated by scaling the RDD to a radial exciton density distribution

$$n(r) = A\,\rho\,D(r) \tag{4.7}$$

giving the number of excited states per unit volume n. Eq. (4.7) represents the total number of molecules excited to the first singlet state which all are to emit a photon in the absence of quenching.

4.1.5 Quenching parameters

The bimolecular quenching parameter α is proportional to n^2 in the Blanc model eq. (4.3) and hence greatly dependent on the exciton density: a swift ion with a small LET and broad RDD gives cf. eq. (4.7) a tiny exciton density n in the ion track. That minimizes the bimolecular quenching term αn^2, giving an insignificant fraction of quenching in the ion track. The situation is reversed in slow ions with narrow RDDs and a high LET which cause a huge exciton density n. A dense track leads to quenching contributions from the higher-order quenching terms in eq. (4.6) and an significant amount of quenching in the ion track.

The scintillator response results published by Jang et al. (2012) indicate that the luminescence signal from PMMA is quenching-free, as both the pristine

[2] With the aid of several dubious and contradicting approximations.

Bragg peak and SOBP measured with a PMMA fiber perfectly matched the ionization curve along the central beam axis of a proton beam. While some conclusions and results in the paper certainly arise from misconceptions, the quenching-free result is to some degree in agreement with the Blanc formalism: PMMA is a poor scintillator with a low light yield per deposited energy. Hence, the initial exciton density in eq. (4.7) is somewhat low regardless of the LET and the quenching interactions between molecules are negligible. That would lead to a negligible amount of quenching in the Blanc formalism and could explain the quenching-free conclusion by Jang et al. (2012).

The quenching-free nature of the PMMA-based optical fibre irradiated with protons was, however, not reproducible as shown in figure 2.5. The response of the PMMA exhibits a distinct non-linear response along the central beam axis of the proton beam relative to an ionization chamber measurement, albeit the fraction of quenching is less than for traditional scintillator measurements.

The next section aims at combining ATSMs and the Blanc formalism to numerically calculate the fraction of quenching in an ion track and scintillating material.

4.2 Algorithm development

The initial exciton density in an ion track is modelled by eq. (4.7). The subsequent exciton movements are governed by the partial differential equation (PDE) in eq. (4.3) which evolves the excitons in time and space and accounts for both fluorescence and quenching.

The PDE is solved with a finite difference method (FDM) where the details are specified in paper II. The cylindrical symmetry of RDDs ensures that the azimuth and axial coordinates in the diffusion term of eq. (4.3) vanish. Consequently, only the exciton densities as a function of the radial distance and time need to be accounted for in the FDM solution.

The fluorescence from the PSD is computed as the sum of the emitted fluorescence photons, represented by the pn term in the Blanc model, which varies with the RDD and the scintillator decay time and light yield. The QCF is calculated by solving the PDE twice for the fluorescence emission: firstly without the quenching terms, i.e. eq. (4.3) with $0 = k = \alpha = \cdots$, to calculate the quenching-free response. Secondly, the system is solved again but now including all quenching terms to calculate the quenched response. The QCF is calculated as the ratio of the fluorescence without quenching to the amount of fluorescence reduced by quenching, similar to the RE in eq. (3.11). The reader is referred to paper II for a more detailed description of the algorithm.

The algorithm is implemented in `Python` where numerically demanding routines—as the solution of the PDE—for efficiency is implemented in the `C` based version of `Python`, `Cython`. The open-source code is henceforth referred

to as `ExcitonQuenching` and available for download[3] along with implementations of the stopping force calculations, ATSMs, and the Blanc model.

4.2.1 Quenching calculations

The `ExcitonQuenching` computed QCFs are assessed against experimentally obtained QCFs in paper II, where the influence of the exciton diffusion constant D and quenching parameters k and α in the Blanc model are examined. An example of the correlation between the QCFs and the LET_Φ is shown in figure 4.4 for the BCF-12 PSD exposed to protons below 200 MeV. The theoretical QCFs calculated with `ExcitonQuenching` are shown for reference.

The `ExcitonQuenching` response is calculated and plotted (solid line) with the Blanc model parameters D, τ, α_1 presented in paper II. The theoretical QCFs are re-calculated with `ExcitonQuenching` for different values $\alpha_1/2$ (dashed lines) and $2\alpha_1$ (dot-dashed lines) of the bimolecular quenching parameter α to illustrate the sensitivity of the QCFs.

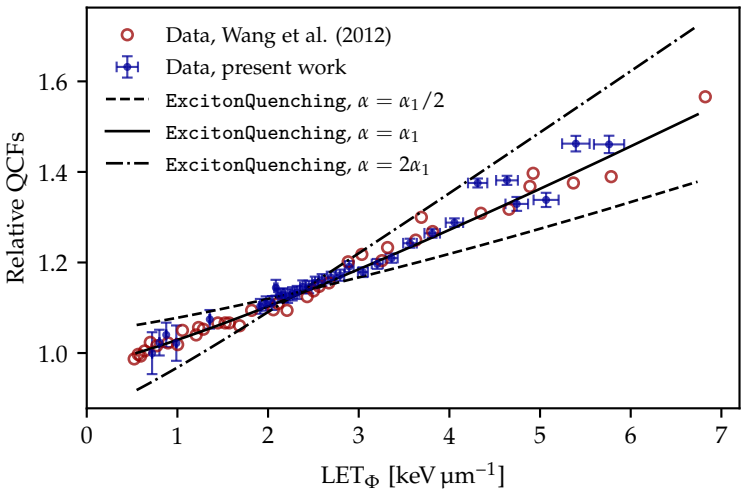

Figure 4.4: Experimentally obtained quenching correction factors for the BCF-12 PSD for protons at different energies: data from Wang, Perles, et al. (2012) (circles) and own measurements (markers with errorbars). The theoretical correction factors (lines) are calculated with `ExcitonQuenching` for different values of the bimolecular quenching parameter α where $\alpha_1 = 9.0 \times 10^{-8}\,\mathrm{cm^3\,s^{-1}}$ to illustrate its importance.

[3] `https://github.com/jbrage/ExcitonQuenching`

4.3 Temporal quenching structure

The Blanc formalism enables, as opposed to other quenching models, an investigation of the temporal structure of ionization quenching. The fluorescent emission is assessed in figure 4.5 for the case of a proton traversing the BCF-12 PSD modelled with the Scholz-Kraft ATSM. The number of photons to be emitted from a thin scintillator slab in the absence of quenching equals the linear exciton density $N = A \cdot \text{LET}$. The main component of the scintillation from the BCF-12 scintillator occurs with a time constant $\tau = 3.2\,\text{ns}$, i.e. the fluorescence emission f decreases with the time t as $f \propto N \exp(-t/\tau)$.

The `ExcitonQuenching` calculated fluorescence emission rates—including quenching—for 3 protons with energies $E_1 = 170\,\text{MeV}$, $E_2 = 9.0\,\text{MeV}$, and $E_3 = 3.7\,\text{MeV}$ are shown in figure 4.5(a). The quenching-free emission (following an exponential decay with time constant τ) is plotted for the E_3 proton for comparison.

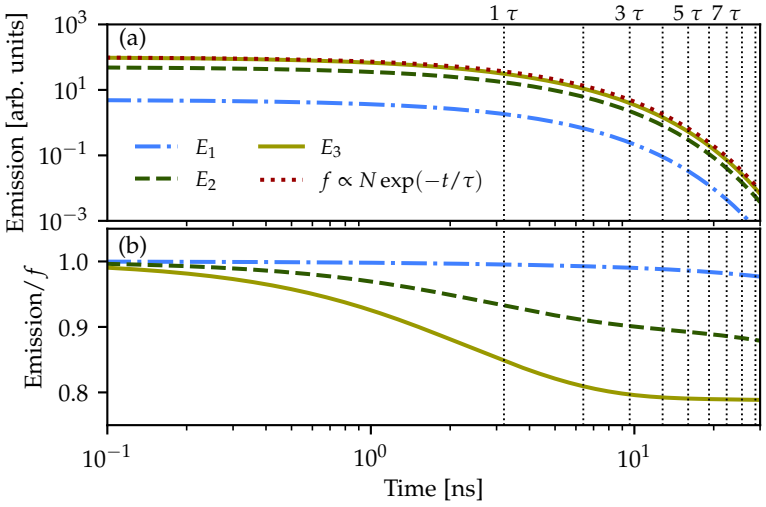

Figure 4.5: (a) `ExcitonQuenching` calculated fluorescence emission for a proton at $E_1 = 170\,\text{MeV}$, $E_2 = 9.0\,\text{MeV}$, and $E_3 = 3.7\,\text{MeV}$ in the BCF-12 PSD including quenching. The unquenched emission f is shown (dotted line) for comparison for the E_3 proton. (b) The fluorescence emission lines E_1, E_2, and E_3 are scaled with the quenching-free fluorescence signal f calculated for each energy. Multiples of the scintillator decay time $\tau = 3.2\,\text{ns}$ is shown with vertical dotted lines for reference.

Each of the fluorescence emission lines in figure 4.5(a) are divided with its non-quenched fluorescence emission in figure 4.5(b). A horizontal line in

figure 4.5(b) corresponds to the case where the quenching in the ion track is negligible.

The fluorescence emission rates as a function of time for the swift E_1 proton almost follows the quenching-free emission, indicating that quenching in such a track is insignificant. The fluorescence rate in the densest track, E_3, with the highest LET decreases rapidly due to quenching and converges slowly towards a horizontal (quenching-free) line. Figure 4.5(b) indicates that most of the quenching occurs within the first nanoseconds after excitation. The fluorescence emission is overall converged to the same rate as the unquenched emission after 3τ. The observation that ionization quenching takes place within the first nanoseconds agrees with experimentally obtained results (Kallmann and Brucker 1957).

The following chapter applies `ExcitonQuenching` as released[4] in `v1.0` to examine the ionization quenching in ion beams.

[4] `https://github.com/jbrage/ExcitonQuenching/releases`

Chapter 5

Quenching Corrections

An energetic HCP in plastics ionizes the atomic electrons and may further liberate heavier particles along its path. Nuclear fragments as well as secondary protons are slower than the primaries with a corresponding denser track structure and elevated quenching. The following chapter is based upon papers III and IV and focuses on the results for quenching in secondary ions and in mixed particle fields.

5.1 Luminescence in heavy ion tracks

The luminescence efficiency of an ion with energy E and relative speed β can be obtained by rewriting eq. (4.1) as

$$\frac{\mathrm{d}L}{\mathrm{d}E} = A \cdot \mathrm{QCF}^{-1}(\beta). \tag{5.1}$$

The efficiency is used to calculate the total luminescence as the ion is completely stopped in a bulk scintillator as

$$L = \int_0^E A \cdot \mathrm{QCF}^{-1}(\beta)\ \mathrm{d}E, \tag{5.2}$$

where all QCFs are calculated with `ExcitonQuenching`. The luminescence efficiencies for isotopes of lithium, helium, and hydrogen traversing a thin slab of the BCF-12 PSD are shown in figure 5.1(a). The scintillation efficiency is found to be the same for all isotopes of an element in agreement with experimental observations (Avdeichikov et al. 2002). The luminescence emission in light ion tracks occurs with a higher efficiency at low velocities but all efficiencies converge towards the light yield of the PSD for $\beta \to 1$.

The luminescence efficiency as a function of ratio of the speed to the projectile charge z is shown in figure 5.1(b). The dependencies of the luminescence efficiencies all coincide which agrees with results reported by Sibczyński et al. (2018) for inorganic scintillators.

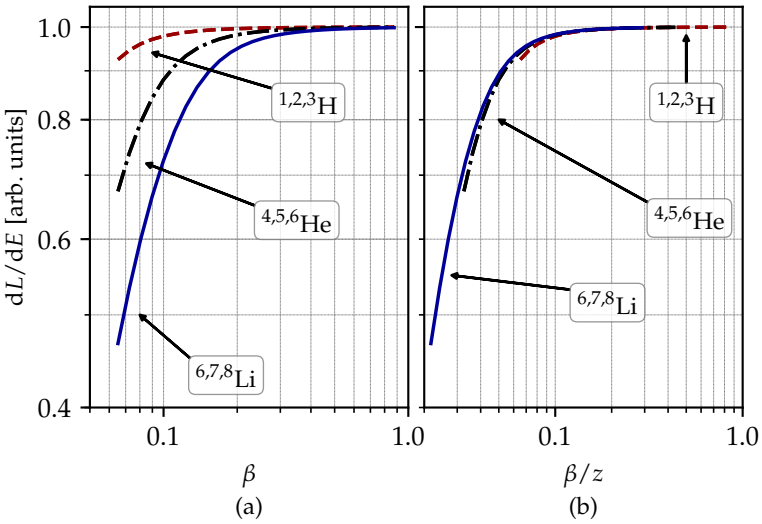

Figure 5.1: Luminescence efficiency for isotopes of hydrogen (dashed lines), helium (dashed-dotted lines), and lithium (solid lines) as a function of (a) the relative speed β and (b) β divided by the projectile charge z. Figure adapted from paper III.

The measured luminescence emitted from an organic scintillator (Pilot-U, Eljen Technology, USA) irradiated with several HCPs is used to validate `ExcitonQuenching`. The scintillator is sufficiently thick to stop the ions completely and the luminescence response—published in Buenerd et al. (1976)—is compared to calculations with `ExcitonQuenching` in figure 5.2. The residuals between `ExcitonQuenching` and the experimental data exhibit a random scatter for helium and lithium ions. The residuals for carbon and oxygen, on the other hand, show a trend indicating that `ExcitonQuenching` is incapable of predicting the quenching correctly for such heavy ions.

5.1.1 Heavy ion deficiency

The quenching calculations with `ExcitonQuenching` shown in figure 5.2 rely on the Chatterjee-Schaefer ATSM. Calculations with the Scholz-Kraft ATSM in paper III show a similar structure of the residuals and discrepancy for all ions which indicates the deviation is related to the Blanc formalism rather than the use of a particular ATSM.

Two elements in the Blanc model in eq. (4.3) implemented in the current version of `ExcitonQuenching` could explain the observed discrepancy with respect to the data:

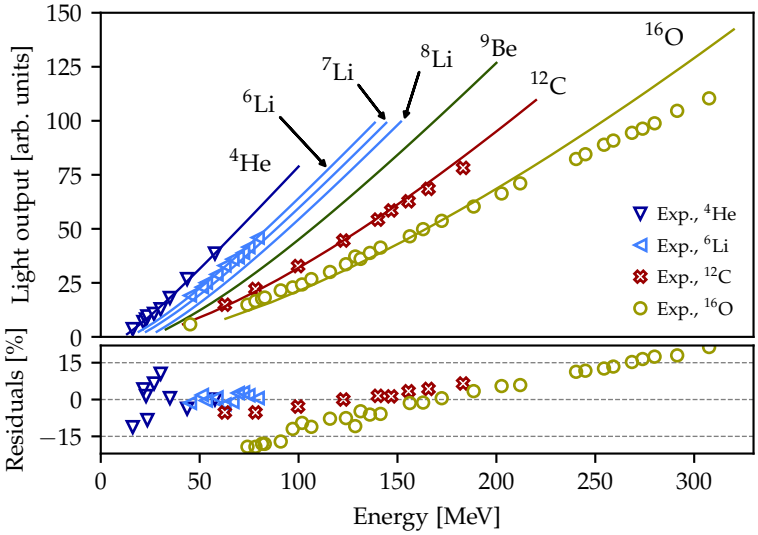

Figure 5.2: The `ExcitonQuenching` predicted luminescence response (solid lines) versus the experimentally measured (markers) luminescence in the Pilot-U scintillator irradiated with several ions stopped in the scintillating material. The experimental data is extracted from Buenerd et al. (1976). The figure is modified from paper III.

(1) The lack of triplet states: The Blanc formalism only includes fluorescence from singlet state de-excitations to the ground state and not the presence of triplet states. The high-LET ions increase the overall density of both excited singlet and triplet states. Two molecules with triplet states may interact and result in one excited singlet state and the other in the ground state (Jain, Blum, and Subramaniam 2009). Hence, the probability for photon emission following a bimolecular *interaction* between two triplet states increases with the density of excited states, i.e. with the LET.

The fluorescence arising from the two triplet state interactions would be delayed relative to the singlet state fluorescence but would still cause the Blanc formalism to underestimate the total luminescence as it is unaccounted for.

(2) Higher-order quenching terms: Uni- and bimolecular quenching is proportional to the exciton density n to the first and second power, respectively. Trimolecular quenching is related to $h_3 n^3$ in eq. (4.3) where h_3 is several orders of magnitude smaller than the bimolecular quenching parameter α. Trimolecular quenching could occur in dense carbon and oxygen tracks but is unaccounted for in the current `ExcitonQuenching` version. The trimolecular quenching com-

petes with the other quenching terms immediately after the HCP induced excitations of the molecules but would be insignificant rapidly after. The inclusion of the higher-order quenching terms in the Blanc formalism would lower the total luminescence.

Both cases (1) and (2) occur primarily in high-LET beams. Nonetheless, the combination of ATSMs and the Blanc formalism enables a numerical calculation of the quenching in proton, helium, and lithium ion tracks.

5.1.2 Proton quenching corrections

The quenched response of a PSD irradiated with protons in figure 4.1 was corrected with the Birks and Chou models in figure 4.3. The residuals of the Birks and Chou model corrected PSD signals were found to exhibit the same structure.

Quenching corrections calculated with the Birks model are compared to quenching predictions by `ExcitonQuenching` in figure 5.3 for the same beam and the BCF-60 PSD. Most of the quenching corrected measurements fall within 5 % of the dose measurement with an ionization chamber with some outliers around 10 % near the Bragg peak.

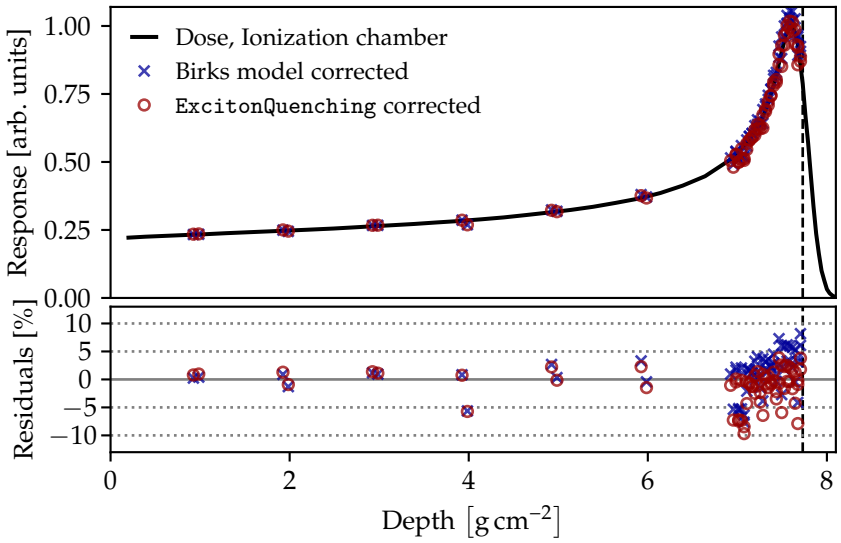

Figure 5.3: A quenched PSD response in a 100 MeV proton beam measured at the Skandion Clinic. The quenched signal has been corrected with fits from the Birks model (crosses) and independent predictions by `ExcitonQuenching` (open circles). The residuals are for each model calculated relative to an ionization chamber measurement. Figure adapted from paper IV.

The ExcitonQuenching predicted QCFs in figure 5.3 exhibit a similar structure and quality as the QCFs obtained with the Birks model from fits to data. The agreement between ExcitonQuenching and the ionization chamber measurements validates the use of the algorithm to predict the quenching in PSDs irradiated with proton beams.

5.2 Mixed particle fields

The energy deposition in a proton beam at clinically relevant energies is heavily dominated by the primary particles. The number of HCPs liberated via nuclear interactions varies with the material compound. The following investigation of the quenching in nuclear fragments is based on Geant4 simulations of a 100 MeV proton beam in water as most PSDs are nearly water equivalent. The dose contribution along the central axis from the primary and secondary protons as well as two isotopes of hydrogen and helium are shown in figure 5.4.

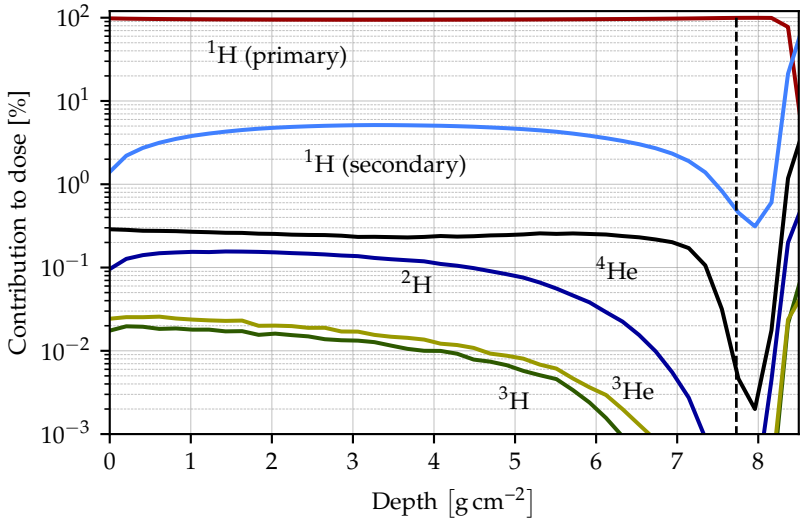

Figure 5.4: Geant4 simulations of the dose contribution from six ions in a water phantom irradiated with 100 MeV protons. The dashed vertical line denotes the 80 % distal dose point. Figure modified from paper IV.

The dose deposition from primary protons generally constitutes more than 92 % of the dose. The dose contribution from secondary protons varies from 1 % at the entrance region to 6 % around half the CSDA range. Heavier particles such as alphas, deuteron ions, and tritium ions are less frequent but with a much higher LET than the primary protons exhibiting an enhanced quenching.

Hence, the total light emission in the mixed particle field differs from that of the primaries alone in terms of an increased quenching.

The LET_Φ and LET_D as defined in eq. (3.4) and (3.5), respectively, are scored in `Geant4` for each of the particles as illustrated in figure 5.5.

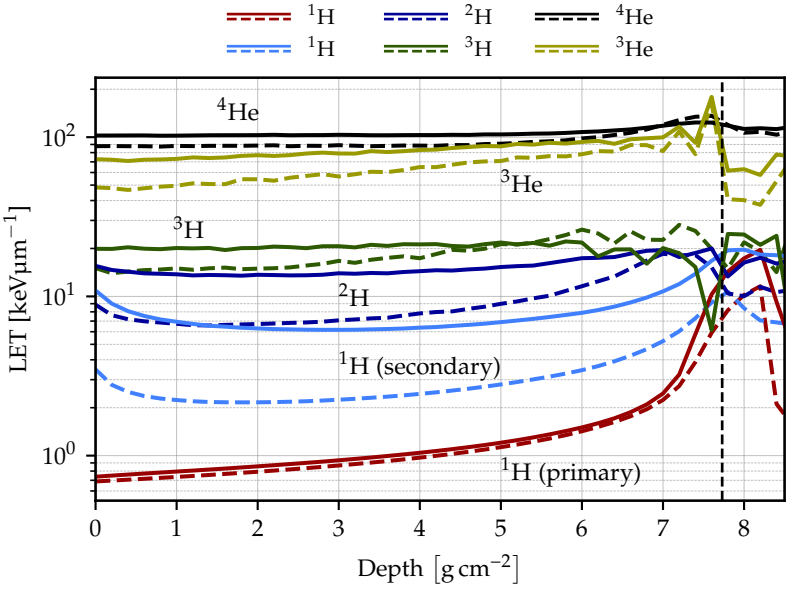

Figure 5.5: `Geant4` calculations of the LET_Φ (dashed lines) and LET_D (solid lines) for primary and secondary protons as well as the two most common isotopes of hydrogen and helium. The dashed vertical line shows the 80 % distal dose point. Figure from paper IV.

5.2.1 Combined quenching correction factor

The concept of a common QCF for a mixed particle field was introduced in paper IV. The six ions contributing the most to the dose in a proton beam quench differently and a total QCF is estimated along the central beam axis. An ion depositing a dose $D_i(x)$ at a depth x will in the case without quenching ($\mathrm{QCF}_i = 1$) emit a fraction $w_i(x) = D_i(x)/D_\mathrm{total}(x)$ of the total light, where $D_\mathrm{total}(x)$ is the sum of all doses at the depth x in figure 5.4. However, the light emission for that particular ion in the presence of quenching ($\mathrm{QCF}_i > 1$) is reduced and proportional to $w_i(x)/\mathrm{QCF}_i < 1$. The total quenching correction

factor in a mixed particle field at the depth x is calculated as

$$\frac{1}{\mathrm{QCF}_{\mathrm{total}}(x)} = \frac{1}{D_{\mathrm{total}}(x)} \sum_i \frac{D_i(x)}{\mathrm{QCF}_i(x)}, \tag{5.3}$$

where $\mathrm{QCF}_i(x)$ is the `ExcitonQuenching` calculated quenching correction using the LET_Φ in figure 5.5, and the sum is over the six ions. Eq. (5.3) corresponds to an extension of the RE in eq. (3.11) to a mixed field.

The `ExcitonQuenching` calculated luminescence from each of the six ions is shown in figure 5.6. The primary ions in figure 5.4 account for more than 92 % of the dose at any point but are responsible for more than 95 % of the luminescence as the secondary ions quench the emission more.

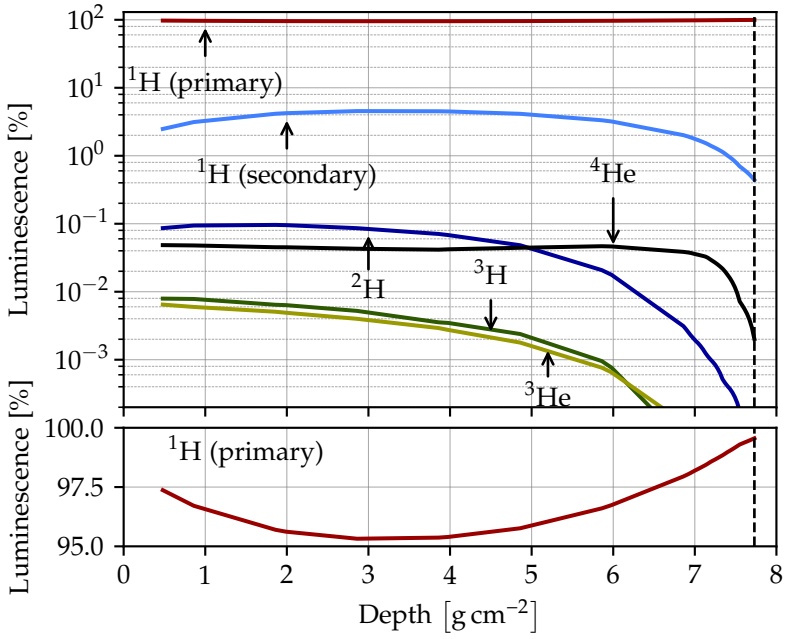

Figure 5.6: `ExcitonQuenching` calculations of the contribution to the total luminescence from each of the six ions based on eq. (5.3). The lower figure is a close-up of the luminescence from the primaries and shows that more than 95 % of the total luminescence arises from the protons at any water depth. Figure modified from paper IV.

5.2.2 Energy spectra

The Geant4 calculations of the LET spectra for the primary and secondary protons in the 100 MeV proton beam is given in figure 5.7. Traditionally, the Birks and Chou models in eq. (4.2a) and eq. (4.2b) are taken to be functions of the LET_Φ or occasionally of the LET_D. The following section assesses the quality of the quenching corrections when the entire proton energy spectrum is taken into account.

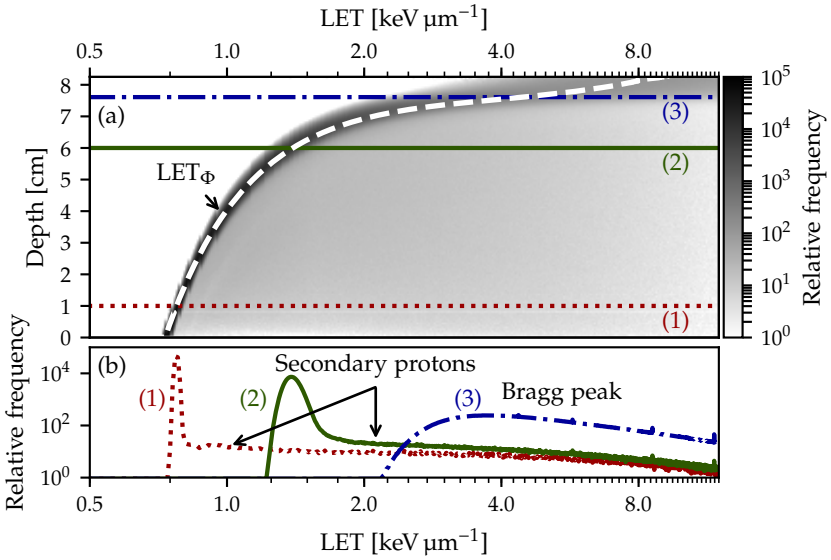

Figure 5.7: Geant4 simulated LET spectrum for primary and secondary protons. The upper figure shows the LET as a function of water depth plotted on the left ordinate. The arithmetic mean of the LET spectrum at each depth, the LET_Φ, is plotted with a white, dashed line. The lower figure shows the LET spectrum at three depths indicated above with the same line styles. Figure modified from paper IV.

The case of quenching corrections using the LET spectrum is treated in paper IV where $\varphi(s,x)$ is the normalized intensity of the LET denoted with s at a depth x. $\varphi(s,x)$ is shown in the lower subfigure of figure 5.7 for spectra at the (1) entry channel, (2) near the Bragg peak, and (3) at the Bragg peak.

The Chou model combined with the full proton LET spectrum gives

$$\mathrm{QCF}(x) = \int_0^\infty \left(1 + kB \cdot s + C \cdot s^2\right)\, \varphi(s,x)\, \mathrm{d}s \tag{5.4a}$$

$$= 1 + kB \cdot \mathrm{LET}_\Phi(x) + C\left(\sigma^2(x) + {\mathrm{LET}_\Phi}^2(x)\right), \tag{5.4b}$$

where $\sigma^2(x)$ is the variance of the spectrum and $\mathrm{LET}_\Phi(x)$ as usually is the arithmetic mean of the spectrum at depth x. The Birks model with $C = 0$ returns—due to its linearity—simply itself as a function of the LET_Φ. The quality of the different QCFs for mixed particle fields and calculated using the full proton energy spectrum in eq. (5.4b) is compared below.

5.2.3 Model comparison

The different quenching models are compared through the sum-of-squares differences between the quenching corrected PSD measurement S_{PSD} with uncertainty σ_{PSD} and an ionization chamber measurement S_{IC} as

$$\chi^2 = \sum_i \frac{(S_{\mathrm{IC},i} - S_{\mathrm{PSD},i})^2}{\sigma^2_{\mathrm{PSD},i}}, \tag{5.5}$$

for each data point i. The χ^2 in eq. (5.5) is divided by the degrees of freedom (DoF), where the DoF is given as the number of data points minus the number of model parameters. The estimates of the scintillator response uncertainty $\sigma_{\mathrm{PSD},i}$ are mainly affected by positioning uncertainties.

The Birks and Chou model corrections

The quality of the different quenching correction methods are given in table 5.1: the quenching corrections relying on the LET_Φ give similar results for method (A) with the Birks model and method (B) the Chou model. The kB and C quenching parameters obtained from linear and quadratic fits are listed in the table for the BCF-12 and BCF-60 PSDs and in agreement with previously reported values (Wang, Perles, et al. 2012; Alsanea and Beddar 2017; Hoehr et al. 2018). Other PSDs have been investigated where the results are presented in paper IV.

Method (C), where the Chou model is applied through eq. (5.4b) to correct the quenching based on the energy spectrum, gives corrections of similar quality as method (B), where it was corrected based solely on the LET_Φ. The similarity could be anticipated as the LET spectrum at the entry channel is narrow and $\mathrm{LET}_\Phi{}^2 + \sigma^2 \approx \mathrm{LET}_\Phi{}^2$. Hence, the narrow spectrum effectively reduces method (C) in eq. (5.4b) to method (B) in eq. (4.2b). The variance σ^2 of the spectrum at the Bragg peak cannot be neglected. However, the LET estimates at the steep dose gradients are related to large uncertainties and the QCFs calculated from the entire spectrum are thus suppressed in the χ^2/DoF estimates. Hence, it is unnecessary to include the energy spectrum for quenching corrections in a proton beam.

`ExcitonQuenching` corrections

The `ExcitonQuenching` QCFs are computed using (D) the LET_Φ from the primary protons and (E) the combined quenching corrections in a mixed particle field as given by eq. (5.3). The qualities of the `ExcitonQuenching` corrections for the mixed particle field are comparable to the results based on the QCFs from the primaries given in table 5.1. Such an observation is in agreement with the conclusion in section 5.2.1 where the primaries were shown to constitute more than 95 % of the luminescence.

Table 5.1: Quality of the quenching corrections for the two PSDs irradiated with protons at clinically relevant energies. The models are compared through the χ^2/DoF in eq. (5.5). The quenching parameters kB and C for the Birks and Chou models along with the qualities of fits for methods (A) using the Birks model eq. (4.2a) and method (B) with the Chou model eq. (4.2b) with primaries only. Approach (C) is the Chou model with the entire proton spectrum eq. (5.4b) and (D) with `ExcitonQuenching` relying on the primaries only and (E) where `ExcitonQuenching` corrects the quenching in a mixed particle field.

	BCF-12			BCF-60		
	kB [µm keV^{-1}]	C [µm^2 keV^{-2}]	χ^2/DoF	kB [µm keV^{-1}]	C [µm^2 keV^{-2}]	χ^2/DoF
(A)	0.107 ± 0.003	—	0.66	0.103 ± 0.004	—	1.12
(B)	0.007 ± 0.002	0.056 ± 0.009	1.08	0.004 ± 0.003	0.08 ± 0.01	1.20
(C)†	—	—	1.01	—	—	1.20
(D)	—	—	0.72	—	—	1.33
(E)	—	—	0.70	—	—	1.26

The Chou model in eq. (5.4b) is not a function of LET_Φ alone and the parameters are omitted.

The quality of the Birks model quenching corrections are overall slightly better than the `ExcitonQuenching` corrections. It is worth emphasizing that the Birks and Chou models are semi-empirical with parameters fitted to each set of measurements. `ExcitonQuenching`, in contrast, predicts the QCFs based on the RDD and scintillator properties with *a priori* knowledge of the response.

5.3 Fluence thresholds

Ionization quenching models, being semi-empirical, numerical as `ExcitonQuenching`, or purely analytical, all rely on the implicit assumption that quenching in ion tracks occurs independent. Such an assumption is often justified since quenching generally occurs within the first nanoseconds upon excitation as measured by Kallmann and Brucker (1957) and calculated in section 4.3.

For comparison, the ion recombination in gas-filled ionization chamber is a much slower process and occurs throughout the charge collection time scale of some 100 µs in ionization chambers. A time scale which allows multiple overlapping ion tracks and increases the ion recombination.

`ExcitonQuenching` enables a calculation of a fluence-rate for which protons will overlap and increase the quenching further. Specifically, the total quenching in two 100 MeV proton tracks is investigated where the distance between the tracks is varied along with the time between the two proton hits. `ExcitonQuenching` computes $\mathrm{QCF}_{\mathrm{single}} = 1.056$ for a single 100 MeV proton in the BCF-12 PSD. Hence, the combined QCF for the two protons is expected to equal $\mathrm{QCF}_{\mathrm{single}}$ if the second proton hits several nanoseconds after the first proton, or if the distance between the track is much larger than the track core radius.

On the other hand, if the two protons hit the scintillator at the same time and place, the combined correction factor is $\mathrm{QCF} \simeq \mathrm{QCF}^2_{\mathrm{single}}$. An interpolated map of the common QCF for the two proton tracks is shown in figure 5.8 where a fraction of the sampled results are shown with dots. The spatial distance corresponding to twice the track core radius r_{min} is shown with a dashed vertical line. The fluence is approximated as the inverse of the track distance squared. The decay time $\tau = 3.2\,\mathrm{ns}$ of the BCF-12 scintillator is shown with a dashed horizontal line.

The map features the zero-order calculations of the quenching between the two tracks and indicates that two 100 MeV protons start to overlap around $\Phi_{\mathrm{TH}} = 10^{10}\,\mathrm{cm}^{-2}$. However, the current computation only includes two proton tracks but several penumbras may overlap during an experiment (Greilich et al. 2010) resulting in sufficient large exciton densities for quenching to occur. The QCF map furthermore indicates that the protons should interact within $10\,\mathrm{ns} \approx 3\tau$. Modern cyclotrons (e.g. the Varian ProBeam or IBA Proteus-235) operate with frequencies around 100 MHz so the different pulses may overlap and increase the quenching.

The proton fluence during the measurements at the Skandion Clinic was in paper IV estimated to $5.5 \times 10^8\,\mathrm{cm}^{-2}$, well below Φ_{TH}. Most ion beam experiments are likewise below the fluence threshold which justifies the application of the quenching models as the quenching processes occur independent of each other.

5.4 LET detector

Different scintillators exhibit different quenching responses in the same beam quality. The quenching variations are reflected in the unique quenching parameters kB and C for each scintillating material in the Birks and Chou models, and with different light yields A and decay times τ in the Blanc formalism. Rather than using the LET or the RDD at a given point to correct the quenching, the different quenching responses of two PSDs may be combined to an estimate of

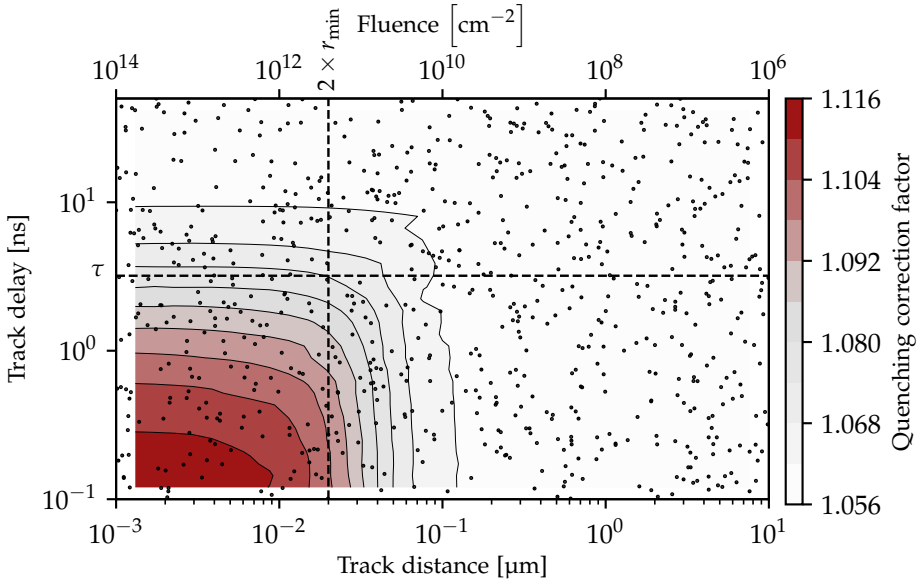

Figure 5.8: The total QCF for two 100 MeV proton tracks in the BCF-12 scintillator calculated with `ExcitonQuenching`. The map is obtained through interpolation of multiple calculations illustrated with dots. The distance between the track centres is varied along with the time between the hits. The quenching is enhanced as the two hits approach each other in time and space. Figure modified from paper IV.

the LET. The BCF-12 PSD is characterized with a large light yield whereas the light yield for the 81-0084 fluorescent fibre (Industrial Fiber Optics Inc., USA) is lower[1] and thus serve as candidates to relate the quenching differences in a point of measurement to the LET.

The quenching experiments were conducted in a 100 MeV proton beam at the Skandion Clinic as detailed in paper IV. The two different scintillators were placed side-by-side in a PMMA ring and the LET_Φ at each point of measurement calculated with `Geant4`. The ratio of the BCF-12 PSD response to the 81-0084 fibre response is shown in figure 5.9 as a function of the LET_Φ.

The vertical dotted line denotes the 80 % distal dose point where the analyses normally would be truncated. The measurements behind that point are included for reference although both the LET calculations and the responses are subject to large uncertainties as estimated from the LET and signal differ-

[1]The light yield is not tabulated but fluorescent fibres are generally characterized with a much lower excitation efficiency.

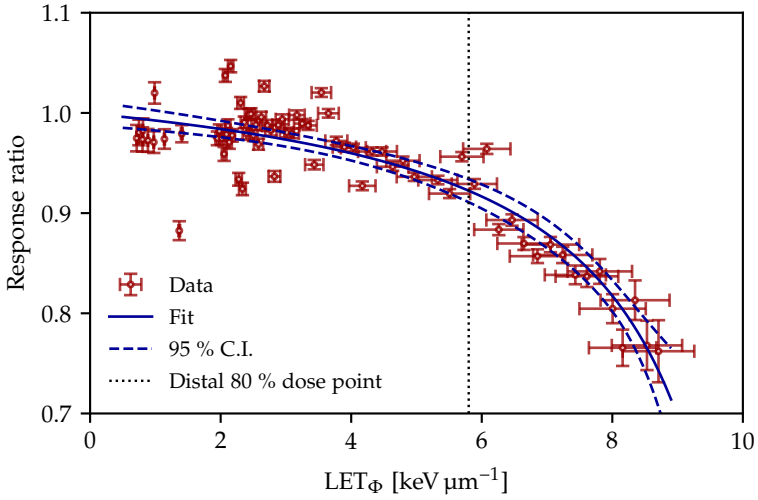

Figure 5.9: The ratio of the quenched response of BCF-12 PSD to the quenched response of the 81-0084 fibre as a function of the LET$_\Phi$. The 95 % confidence interval (C.I.) is shown with dashed lines. The 80 % dose threshold is delineated with a dotted vertical line.

ences if the detectors were misaligned by 0.5 mm.

While the response ratio shows an overall trend, the data scatter around 2 keV µm^{-1} to 4 keV µm^{-1} is large compared to the small deviation from unity, and the approach is too uncertain to be applied for LET estimations. Similar negative results were obtained by cross-comparisons between the quenching differences in the BCF-12 and BCF-60 PSDs and the 81-0084 fibre. Most of the discrepancy could be explained with systematic errors in the experimental setup, where small position errors at the distal edge give huge LET and signal uncertainties. Similarly, the LET scoring behind the 80 % distal dose point is generally extremely sensitive to the implementation and what particles are included (Cortés-Giraldo and Carabe 2015; Grzanka, Ardenfors, and Bassler 2018).

On the other hand, Alsanea, Therriault-Proulx, et al. (2018) did succeed in relating the quenching differences between the BCF-12 and BCF-60 PSDs to the LET$_\Phi$. A more robust approach to measure the LET exploiting the quenching in two PSDs would be to measure the response in the plateau region of high-LET beams.

Chapter 6

Graphite calorimetry

While protocols as the IAEA TRS-398 (Andreo, Burns, Hohlfeld, et al. 2000) or AAPM TG-51 (Almond et al. 1999) recommend ionization chambers for reference dosimetry, other reports (Vynckier, Bonnett, and Jones 1991; ICRU 1998) highlight calorimetry. An absolute ionometric dose measurement requires an absorbed dose to water calibration, an accurate estimation of the energy expended in the production of a pair of ions in the gas W, and knowledge of the exact chamber volume. The use of ionization chambers in scanning ion beams furthermore requires careful and complex corrections for ion recombination which varies with both the RDD and dose-rate along the central beam axis.

The operating principle of a calorimeter is, ideally, that all deposited energy is expressed as heat which is related to the absorbed dose through the specific heat capacity. TRS-398 recommends the use of calorimetry to correct the recombination in high-intensity scanning ion beams[1] which limits the applicability of ionization chambers for quenching corrections. Calorimeters are thus more attractive for absolute dose measurements than ionization chambers and enable more accurate quenching corrections relative to PSDs.

The design and operation of a portable in-house developed graphite calorimeter is presented and discussed in the following chapter. The main objective is to assess and correct the quenched PSD response relative to the calorimeter.

6.1 Absorbed dose

Energy deposited in a calorimeter is related to a temperature rise ΔT depending on the heat capacity. A water calorimeter may suffer from a heat defect where a large fraction of the deposited energy is spent on chemical reactions rather than being expressed as heat (Ross and Klassen 1996; Medin 2010). The present work investigates the use of a calorimeter with graphite cores with insignificant

[1] Although a novel method for such recombination corrections with gas-filled ionization chambers is proposed in paper V.

impurities and heat defects. The absorbed dose to the graphite is then given as

$$D = c_g \Delta T, \tag{6.1}$$

where c_g is the specific heat capacity of graphite.

6.1.1 Temperature conversion

The radiation induced temperature change ΔT in graphite is measured indirectly with a Wheatstone bridge: a thermistor is glued to the graphite core and connected to the bridge. Small temperature rises (order of mK) in the graphite will cause a resistance change in the thermistors and give rise to a voltage change across the Wheatstone bridge. The temperature change in the graphite can be inferred from the voltage change but such a traceable conversion is yet to be established for the system.

This chapter investigates the response of the graphite calorimeter to radiation in terms of the voltage difference across the Wheatstone bridge. It is assumed that a linear conversion from the radiation induced temperature change to the measured voltage exists.

6.2 Experimental design

The experimental design is developed for megavoltage photon beams in Santurio (2019) and sketched in figure 6.1. The aim is to measure the absorbed dose to graphite simultaneously and independently with two graphite cores. The system contains a large graphite disc (Miller and Kovacs 1985; ASTM 2003) developed at Risø and a smaller graphite core with dimensions and material properties listed in table 6.1. The smaller graphite core can be replaced with a PSD in the calorimeter at position P_2 in figure 6.1 inside a solid water (SW) slab. Repeating the measurements with a PSD in the same position as the graphite core enables a direct comparison between the quenched luminescence and graphite response under similar radiation conditions.

The large graphite disc G_2 integrates over a much wider area than G_1 and can serve to measure the dose-area-product as well as monitoring the dose delivery. The build-up between the gantry nozzle and position P_2 consists of the PMMA window and SW components with a combined mass thickness of $(8.8 \pm 0.1)\,\mathrm{g\,cm^{-2}}$, including half the length of the small graphite G_1. The mass thickness is unimportant for the quenching corrections, as the graphite and PSD are placed in the same position, but affects the `Geant4` Monte Carlo model of the calorimeter and hence the LET scoring.

6.2.1 PSD measurements

The responses of the PSDs and the two graphite cores G_1 and G_2 are investigated relative to the width L of the SW slabs in front of the container. The small

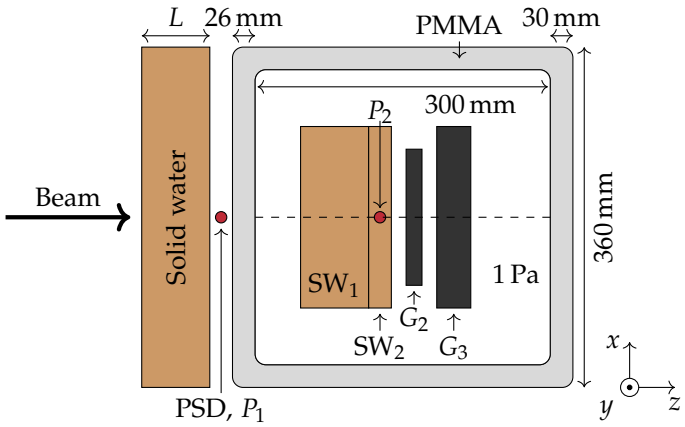

Figure 6.1: The solid water discs labelled SW_1 and SW_2 are placed on the central beam axis (dashed line) along with the graphite cores labelled G_2 and G_3. The small graphite core G_1 or a PSD can be placed at position P_2 inside SW_2. A PSD is placed at P_1 to monitor the irradiation. The graphite core G_2 is connected to thermistors and used for measurements whereas G_3 is used to balance the radiative heat loss from G_2. The air pressure in the container is $\sim$ 1 Pa to minimize heat losses.

Table 6.1: Dimensions and properties of the graphite, PSD, and solid water slabs (Solid Water HE, Sun Nuclear, USA). SW and graphite emissivities ε are extracted from Morgan et al. (2017) and Ionita, Radu, and Astefanoaei (2013), respectively. The specific heat c_p values are estimates from tables in ANSYS. $\varnothing$ denotes the diameter and ℓ the length of the cylindrical elements.

Object	Material	$\varnothing$ [mm]	ℓ [mm]	ρ [g cm^{-3}]	ε	c_p [J kg^{-1} K^{-1}]
G_1	graphite	5	7	2.25	0.82	710
G_2	graphite	138	10.5	2.25	0.82	710
G_3	graphite	170	30	2.25	0.82	710
PSD	polystyrene	0.5	2	1.06	N/A	N/A
SW_1	SW	170	50	1.032	0.94	$\sim$ 1100
SW_2	SW	170	10	1.032	0.94	$\sim$ 1100

graphite core G_1 is suspended in hole drilled in SW_2 as shown in figure 6.2(a). A dummy copy of the small graphite core G_1 is shown in figure 6.2(b) with a 1 mm hole drilled through the center in which a PSD can be placed. The PSD is guided through a channel drilled in the SW (figure 6.2(a)) into the dummy graphite in order to measure the luminescence under similar conditions as the graphite measurements.

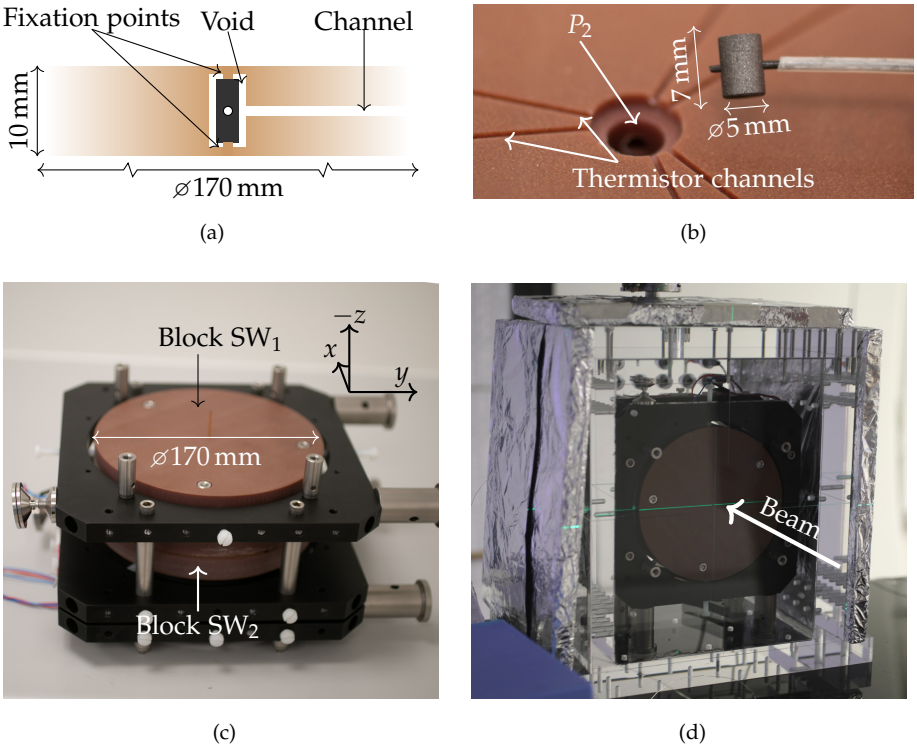

Figure 6.2: (a) Side view of SW_2 where the PSD can be guided through the channel into a hole drilled through the center of a dummy graphite piece. (b) The dummy graphite with the PSD pinned in the center. Three pairs of thermistor channels drilled in the surface of the SW_2 are visible. (c) Photo of SW_1 and SW_2 confined in a metal frame. (d) The calorimeter aligned on the couch at DCPT before irradiation where the surface of SW_1 is visible through the PMMA front window.

6.2.2 Scanning ion beams

The calorimeter was irradiated at DCPT with a scanning proton beam fixed at 170 MeV. The cyclotron enables a delivery of a dose to water at the entry channel of 3 Gy in 0.7 s ensuring a prompt temperature increase during which the heat losses are minimized.

The field consisted of 5×5 spots in 2 cm $\times$ 2 cm as illustrated in figure 6.3. The field size was chosen to be sufficiently small to be entirely collected by the large graphite disc G_2 and large enough to cover both the small graphite core G_1 and the PSD in P_2.

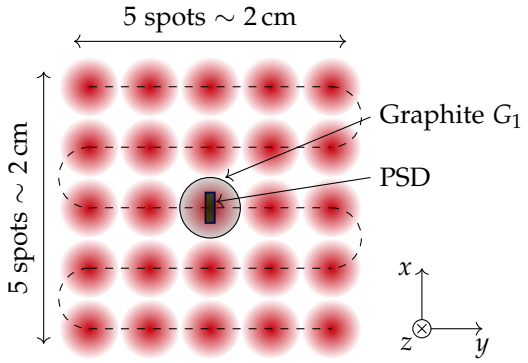

Figure 6.3: The spot scanning pattern with a 5 mm spot separation approximately drawn to scale. The PSD and graphite core G_1 at position P_2 where the PSD axis is aligned perpendicular to the beam axis. The diameter of the large graphite disc G_2 exceeds the field size.

6.2.3 Heat losses

The heat loss from the graphite to the surroundings is assessed with the finite element method (FEM) tool `ANSYS` (ANSYS inc. version R19.0., Pennsylvania, USA) in figure 6.4. `ANSYS` does not support radiation transport but enables an internal heat generation in the graphite which mimics dose absorption. The materials surrounding the graphite cores will experience similar temperature increases and to some degree balance the radiative heat transfer from each other—an effect unaccounted for in the `ANSYS` calculations and the following results thus serve as upper limits for the heat losses.

The SW_2 slab with the graphite core G_1 pinned in its hollow center, as shown in figure 6.2(a), is implemented in `ANSYS`. The heat loss correction factor upon an irradiation is estimated as

$$k_{\text{heat loss}} = \frac{\Delta T_{\text{no losses}}}{\Delta T_{\text{incl. losses}}}, \tag{6.2}$$

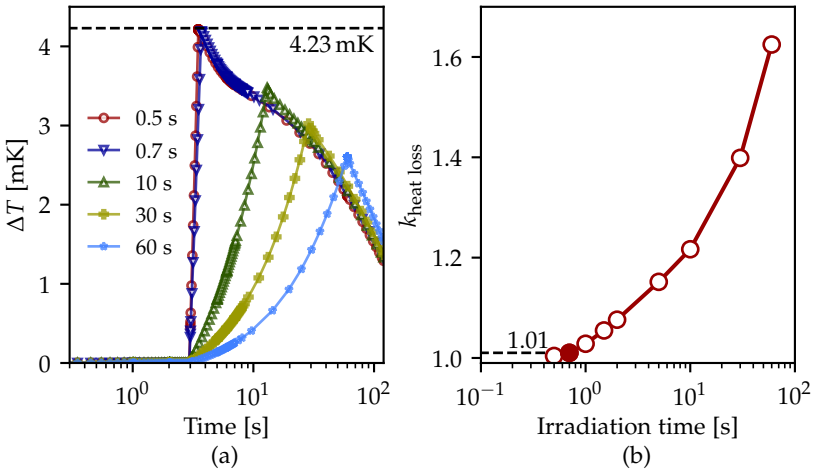

Figure 6.4: (a) ANSYS simulations of the temperature increase in the small graphite core G_1 for a 3 Gy dose deposition which starts at $t = 3$ s. The time it takes to deposit the dose is given in the figure legend. ΔT without any heat losses is shown with a horizontal dashed line. (b) shows the heat loss correction factor $k_{\text{heat loss}}$ as a function of the time it takes to deposit the 3 Gy dose. The experimental 0.7 s dose deposition time is plotted with a filled circle with a correction of 1 %. The calculations should be regarded as upper limits for the heat losses.

where $\Delta T_{\text{incl. losses}}$ is the simulated temperature increase including heat losses to radiate transfer, convection, and conduction, while $\Delta T_{\text{no losses}}$ is the simulated temperature increase for the same absorbed dose without any heat losses. Hence, $\Delta T_{\text{no losses}}$ equals ΔT in eq. (6.1) in the absence of heat defects.

The deposition of 3 Gy in the small graphite core G_1 over the course of 0.5 s to 60 s is shown in figure 6.4(a). While the rapid dose deliveries minimize the heat losses, the results emphasize the need for heat loss corrections during longer irradiation times. The heat loss correction in eq. (6.2) is plotted as a function of irradiation time for the 3 Gy dose in figure 6.4(b). The correction factor for the small graphite core during the 0.7 s irradiations is about 1 % but would be larger for graphite disc G_2. The upper estimates of the heat losses are in agreement with results in McEwen and Duane (2000).

Heat transfer minimizations

The small graphite core in P_2 is in thermal contact with the solid water at two $< 1\,\text{mm}^2$ contact surfaces indicated with arrows in figure 6.2(a). The calorimeter

is confined in a metal frame as shown in figure 6.2(c) with four nylon screws causing a small heat conduction where the frame acts as a cold temperature reservoir. The convective losses are minimized by decreasing the air pressure to 1 Pa.

The radiative heat transfer remains a challenge for quasi-adiabatic calorimeters (McEwen 2002) as it is non-linear: a hot object with temperature T_h radiates energy to a cooler surrounding with temperature T_c with a radiative heat loss q described as

$$q = \varepsilon \sigma_B A_h \left(T_h^4 - T_c^4 \right), \tag{6.3}$$

where A_h is the surface area of the hot object, the emissivity ε is given in table 6.1, and σ_B is the Stefan-Boltzmann constant. The radiative heat transfer is sometimes counterbalanced by placing materials near the graphite cores: Picard, Burns, and Roger (2009) use a mirror to reflect the radiative heat whereas Palmans et al. (2004) enclosed the active graphite with a passive graphite jacket. The surrounding materials are heated to approximately the same temperature as the calorimeter and thus approximately balance the radiative heat transfer. The present design uses a similar approach, where the large graphite disc G_2 is placed between disc G_3 and SW_2 to balance its radiative heat loss.

6.3 Measurements

An example of two irradiations measured simultaneously with the two graphite cores G_1 and G_2 is shown in figure 6.5. The responses in figures 6.5(a)–(b) were recorded without any SW ($L = 0$) in front of the calorimeter, which corresponds to measurements at the plateau region of the 170 MeV beam with a CSDA range of 19.6 g cm^{-2} given the (8.8 ± 0.1) g cm^{-2} build-up.

The 0.7 s dose deposition time allows the small graphite core in figure 6.5(a) to quickly reach a uniform temperature resulting in an almost instantaneous voltage change. The larger graphite disc in (b), with a diameter much bigger than the field size, takes several seconds to adjust to a uniform temperature causing a heat loss in the process. The responses in figures 6.5(c) and (d) were measured with $L = 10.5$ cm SW which corresponds to measurements at the Bragg peak and behind the distal edge, respectively.

The voltage change for both graphite cores is plotted in figure 6.6 as a function of the width of the SW in front of the calorimeter. The distance between the two Bragg peaks is approximately the mass thickness between the graphite centres (1.9 g cm^{-2}) but deviates slightly as the two responses have been subject to different volume averaging.

6.3.1 Volume averaging

The experimental setup as outlined in figure 6.1 is implemented in `Geant4` to calculate the LET_Φ and a volume correction factor to account for the different

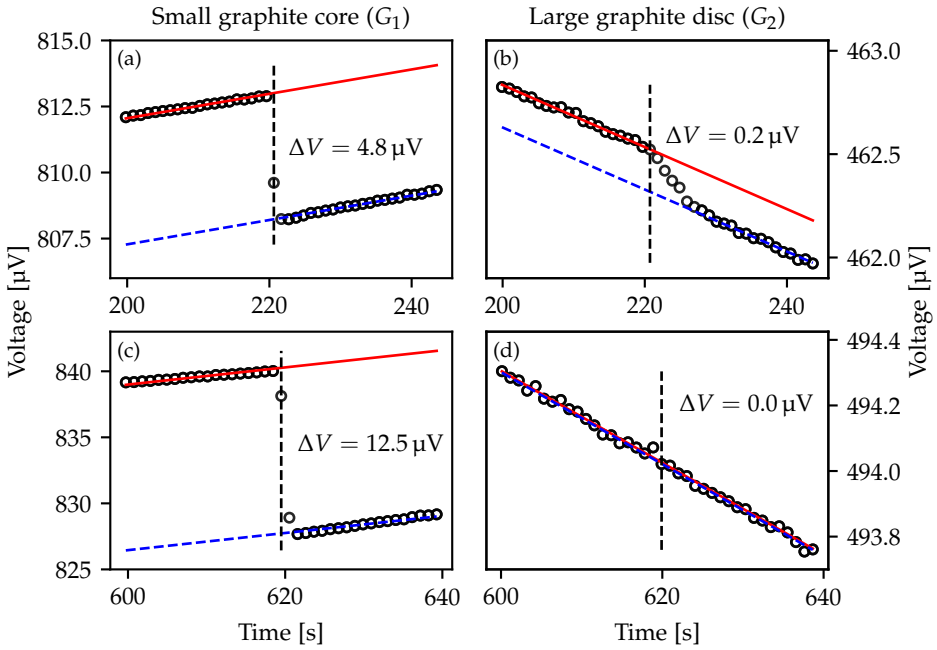

Figure 6.5: The responses of the smaller graphite core in (a) and the larger in (b) correspond to measurements at the plateau region. (c) is a measurement with the small graphite core G_1 near the Bragg peak and (d) is further downstream behind the distal edge with the graphite disc G_2. The vertical dashed lines indicate the start of the irradiation.

volumes and densities. The LET_Φ in the graphite core G_1 and the LET_Φ in the PSD is plotted for reference in figure 6.6 and used to relate the quenched PSD response to the graphite response.

The volume correction factor is computed with `Geant4` as

$$k_{\mathrm{vol}} = \frac{D_{\mathrm{PSD}}}{D_{\mathrm{graphite}}}, \tag{6.4}$$

where D_{graphite} is the dose to the graphite core G_1 and D_{PSD} is the dose to the PSD in point P_2. The `Geant4` calculation of D_{graphite} is first performed with the intact graphite core as a function of the solid water thickness L in figure 6.1. The simulation is then repeated to calculate D_{PSD} under the same conditions with the PSD inserted into the dummy graphite in P_2 as shown in figures 6.2(a)–(b).

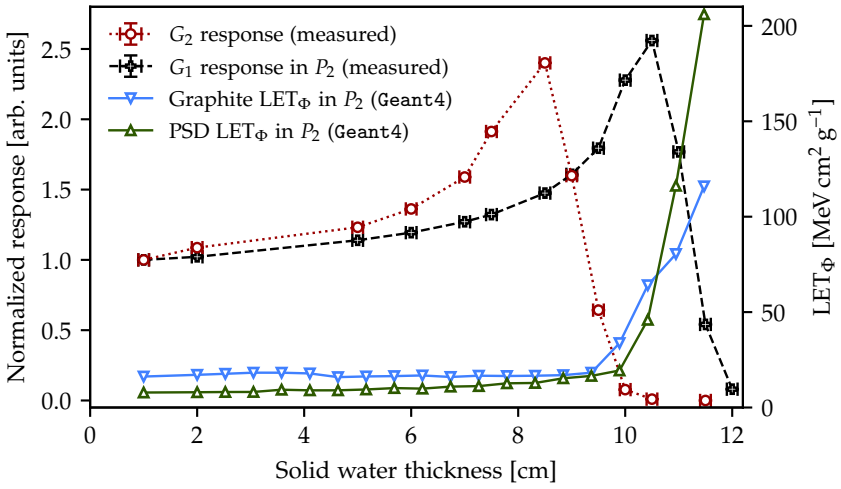

Figure 6.6: The measured response of the small and large graphite cores as a function of the solid water width L. The LET is scored in `Geant4` in both the PSD and the graphite core G_1 in P_2 in two separate simulations.

6.4 Quenching corrections

The response of the PSD is compared to the response of the graphite core G_1 in figure 6.7, where the graphite has been subject to the volume correction given by eq. (6.4). The volume corrected graphite response is used to calculate the QCF, shown in the lower figure, as the ratio of the graphite response to the quenched PSD signal.

The QCFs from figure 6.7 is plotted in figure 6.8 as a function of the LET$_\Phi$ scored in the PSD. A linear function—essentially the Birks model in eq. (4.2a)—is fitted to the data for reference: the slope $kB = (7.3 \pm 0.4)\,\mathrm{mg\,MeV^{-1}\,cm^{-2}}$, obtained with the BCF-60 PSD, is between the two values presented in Hoehr et al. (2018) but smaller than the $kB = (9.7 \pm 0.4)\,\mathrm{mg\,MeV^{-1}\,cm^{-2}}$ derived in paper IV.

6.5 Design improvements

The linearity of the QCFs versus LET$_\Phi$ in figure 6.8 demonstrates the capability of the calorimeter to correct the quenching although several elements may be improved. The discrepancy between the kB parameter for the BCF-60 PSDs obtained from experimental corrections with calorimetry and ionometry is likely to arise from a combination of:

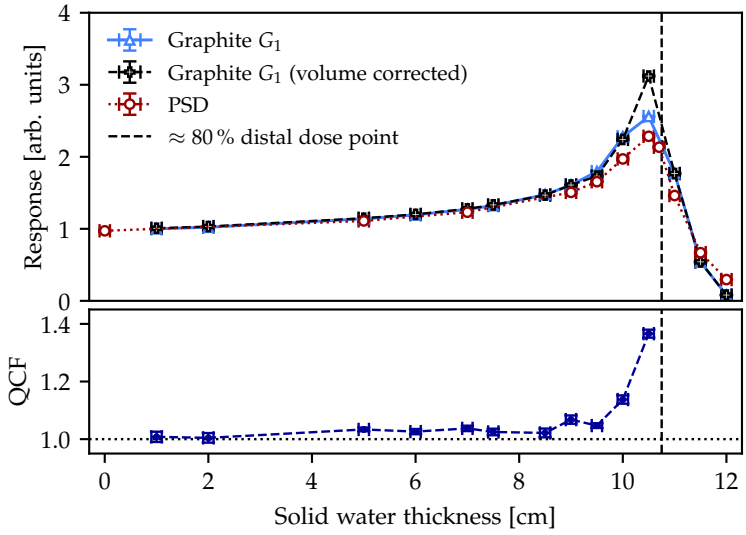

Figure 6.7: The response of the PSD and graphite in P_2 versus the SW thickness. The graphite response has been corrected for the volume averaging with eq. (6.4). The QCF (lower figure) has been calculated as the ratio of the volume corrected graphite response to the PSD response.

Volume averaging: The $1.54\,\mathrm{g\,cm^{-2}}$ mass thickness of the small graphite core along its axis (parallel to the beam) is more than an order of magnitude wider than the PSD diameter of $53 \times 10^{-3}\,\mathrm{g\,cm^{-2}}$ with its axis perpendicular to the beam axis. The volume and density differences cause an unnecessarily large volume correction factor near the steep dose gradients.

The small signal fluctuations for the measurements with the small graphite core in figures 6.5(a) and (c) indicate that the graphite core could be carved even smaller while retaining a good signal-to-noise ratio—preferable carved to the size of the PSD which would reduce the volume averaging corrections.

Monte Carlo scoring: Although the LET_Φ is redundant for an experimental quenching correction of the PSD signal with calorimetry, it does provide information necessary for a theoretical correction. The Monte Carlo model of the experimental setup is not fully validated, and accurate beam parameters were missing, which may cause a systematic bias in the LET_Φ calculations used to extract the kB value in figure 6.8, and hence the observed underestimation.

Heat losses: Despite the rapid dose deposition in the scanning proton beam, the large graphite disc is prone to heat losses during the time it takes to acquire

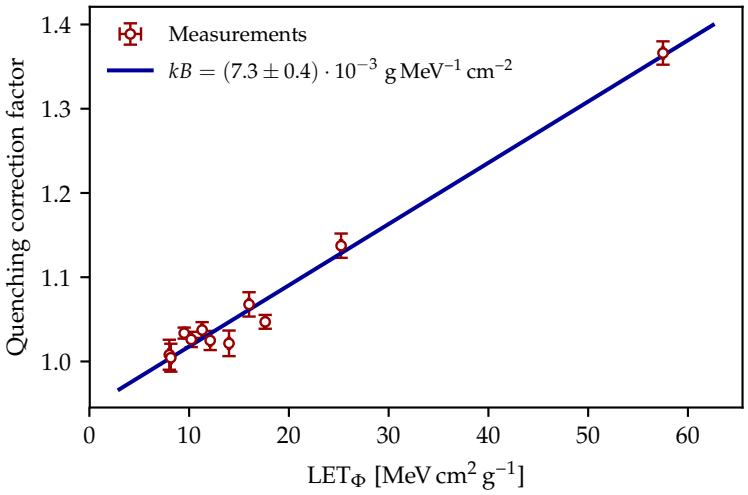

Figure 6.8: The measured QCFs from figure 6.7 as a function of the `Geant4` calculated LET$_\Phi$ from figure 6.6. A linear fit normalized to the measurement with the lowest LET$_\Phi$ is fitted to the data where the slope corresponding to the Birks quenching parameter kB is given in the legend.

a uniform temperature, which emphasises the need for heat loss correction factors. Heat loss corrections would be equally relevant for the small graphite core for measurements where the dose deposition exceeds a few seconds.

Nonetheless, the calorimeter prototype has been shown to be a feasible and novel approach to correct the quenching in PSDs. 10 consecutive measurements of the same field showed a reproducibility within 0.5 %, and the calorimeter is designed to be portable and has been assembled and prepared for irradiations in less than an hour.

6.6 Beam spot parameters

The `Geant4` simulations of the volume correction in eq. (6.4) and the LET$_\Phi$ were performed with rough estimates of the proton beam spot profiles. The measurements with the two PSDs in positions P_1 and P_2, however, enable an extraction of proton beam spot parameters during the experiments, including the spot deposition time, location, and the FWHM. The measurements with an optical fibre in the wide 10 cm $\times$ 10 cm field in section 2.3.2 demonstrated the ability to extract information along a line, whereas the two PSDs in P_1 and P_2 allow point measurements at different depths as shown in figure 6.9.

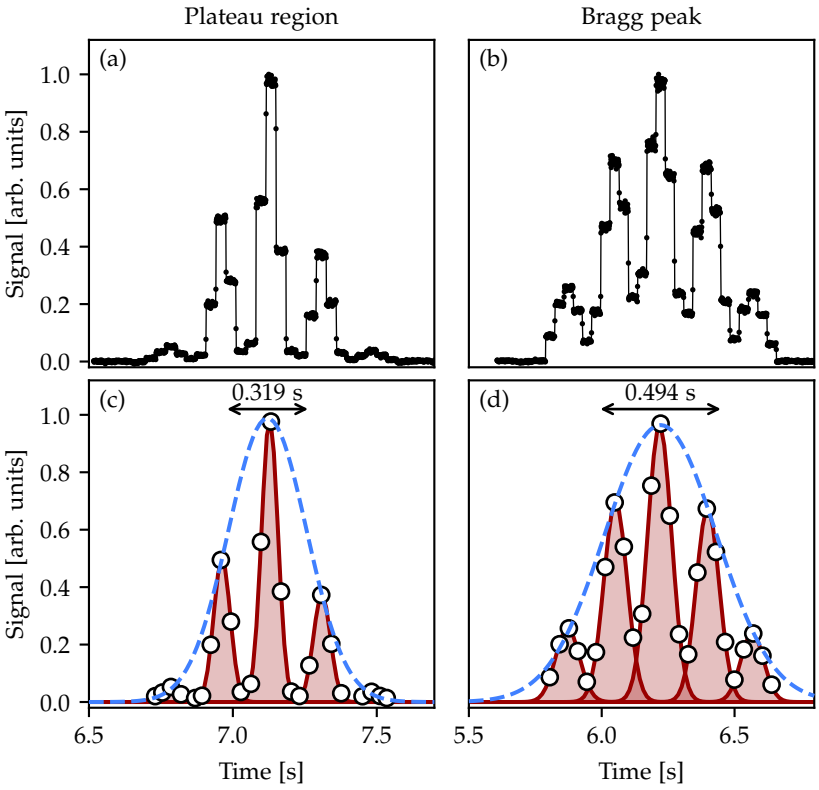

Figure 6.9: Subfigures (a) and (b) show the PMT integrated luminescence response from the scintillator measured at the entry channel and Bragg peak region, respectively. An algorithm is used to locate the different plateaus as beam spots plotted with circles in (c) and (d). Gaussians fitted (dashed blue lines) to each of the maxima of the spot lines (red Gaussians) allow an estimate of the FWHM as a time.

The luminescence signal from the PSD is integrated with a PMT using a 1 kHz sampling rate during irradiations with the 5×5 spots field illustrated in figure 6.3. The integrated signal for measurements at the entry channel and Bragg peak region is shown in figures 6.9(a) and (b), respectively. An algorithm is written to identify horizontal plateaus (i.e. the time it takes to deposit each spot) as individual spots. The plateau centres in measurement (a) are shown with circles in (c) and likewise for the spots during measurement (b) in figure (d).

The algorithm identifies the five spots deposited in the same scan line and fits a Gaussian to those points illustrated with red. A single Gaussian (dashed blue line) is fitted to the maxima of each of the Gaussians in red and resembles the FWHM of the proton beam spots in time. The FWHM *time* is converted into a distance as the beam spots—corresponding to the maxima of the red Gaussians—are 5 mm apart.

6.6.1 FWHM calculations

The proton beam spots at the entry channel in figure 6.9(a) are narrow without much lateral scattering, and the two scan lines furthest away from the centred PSD are difficult to detect. The lateral scattering increases through the PMMA container and solid water resulting in sufficiently wide spots near the Bragg peak to be measured in figure 6.9(b). The calculated FWHM from the PSDs measurements as a function of the width of the solid water is plotted in figure 6.10 along with Monte Carlo calculations from the treatment planning system (TPS) at DCPT.

The measurements of the spot FWHM along the central beam axis in figure 6.10 decreases rapidly after the Bragg peak, whereas the FWHM from the TPS (Eclipse, Varian, USA) simulations increase monotonously. The measured dip behind the Bragg Peak is also reported by Pedroni et al. (2005) and is likely to be related to the lateral spread of the protons along the central beam axis: the least scattered protons travel the longest along the central axis and, as the most scattered protons are stopped around the Bragg Peak, it effectively causes a narrowing of the beam.

The measurements of the FWHM as a function of the depth enables an optimization of the Monte Carlo particle source parameters related to the lateral scattering, i.e. directly improving the k_{vol} and LET_Φ simulations and thus the QCFs in figure 6.8.

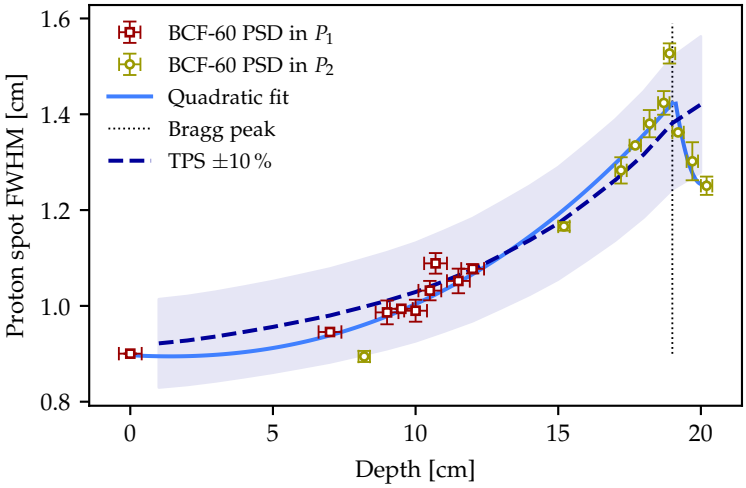

Figure 6.10: The FWHM calculated with the two BCF-60 PSDs placed in positions P_1 and P_2 in figure 6.1. Two quadratic fits have been fitted to the data at either side of the approximate location of the Bragg peak. The TPS at DCPT was used to estimate the FWHM shown with a dashed line and 10 % uncertainty.

Conclusion and outlook

The luminescence properties of optical fibres and plastic scintillation detectors (PSDs) have been investigated for irradiations with photon, electron, and light ion beams with an emphasis on protons. The luminescence signal in optical fibres during proton irradiation was examined by means of measurements and Monte Carlo simulations. The optical photons were shown to be fluorescence with a minor Čerenkov radiation component depending on the angle between the fibre and the beam.

It was demonstrated how a single PSD centred in a small spot scanning field can account for the deposition of all spots. The lateral beam scattering was measured as a function of depth and the calculated spot widths are in agreement with the treatment planning system (TPS) simulations over a wide energy range.

Quenching corrections

While the PSDs enable measurements of the deposition time and size of each proton spot, the conversion from the luminescence response to an energy deposition remains a challenge due to the non-linearity of ionization quenching. The quenched PSD signal has been corrected with several novel experimental and theoretical approaches.

Experimental quenching corrections

The quenched response of three different PSDs (BCF-12, BCF-60, and 81-008) was corrected relative to ionization chamber measurements. Monte Carlo simulations of the experiments and LET_{Φ} calculations facilitate an estimation of the Birks kB parameter for each PSD which are in agreement with literature values. The ionization chamber measurements are prone to underestimate the dose at the Bragg peak region for high-intensity scanning ion beams which motivates an investigation of the ionization quenching in PSDs with calorimetry.

An in-house developed graphite calorimeter was used to measure the energy deposition in a scanning proton beam relative to the quenched response of the BCF-60 PSD. The Birks *kB* parameter estimated from the calorimetry corrections was found to be 25 % lower than the value estimate relative to the ionization chamber corrections. A discrepancy which mainly is attributed to a possible systematic offset in the linear energy transfer (LET) calculations in the Monte Carlo model of the calorimeter with rough estimates of the beam spot parameters.

The quenching correction factors (QCFs) obtained with calorimetry are in principle more accurate than the ones derived from ionometry but more validations of the graphite calorimeter are required at this point.

Theoretical quenching corrections

The numerical algorithm `ExcitonQuenching` was proposed for correcting the quenching of PSDs irradiated with ion beams. The algorithm relies on fundamental physical properties as the scintillator decay time, density, and light yield. The local energy deposition is governed through the use of amorphous track structure models (ATSMs). Such quenching prediction capabilities differ from the semi-empirical quenching Birks and Chou models which require *a priori* knowledge about the quenched response.

`ExcitonQuenching` is open-source and available for download online and has been validated for protons, alpha particles, and lithium ions.

Novel quenching results

Mixed fields: The quenching in a mixed particle field arising from secondary ions liberated during proton irradiations was examined with `ExcitonQuenching`. The combined QCFs in a mixed field are found to be similar to those obtained from the primary protons alone. The secondary protons—and particularly the heavier fragments—are associated with an elevated LET. Even though the secondary ions constitute as much as 8 % of the total dose, the secondary ions quench the luminescence more than the primary protons and effectively constitute less than 5 % of the total luminescence.

Thus, most of the luminescence from secondary ions can be neglected which justifies the calculation of QCFs relying on the LET from the primary ions alone—An LET which can be estimated analytically without Monte Carlo approaches.

Energy spectra: The quenching was examined using the full energy spectrum rather than calculating averaged LET values. The spectrum variance is negligible at the entrance region and the arithmetic mean, the LET_{Φ}, is thus a sufficient quenching predictor. The situation differs at the Bragg peak region where the wide energy spectrum cause the $\mathrm{LET}_{\mathrm{D}}$ or LET_{Φ} averages to be questionable

quenching predictors as the quenching varies non-linearly with the LET. The uncertainties of the experimentally determined QCFs at the Bragg peak were, however, too large to conclude whether the full energy spectrum actually provides better corrections than the LET averages.

Quenching structure and applications: The temporal structure of quenching in PSDs was examined theoretically for the first time with `ExcitonQuenching`: The majority of the quenching occurs within the characteristic decay time of the scintillator in agreement with published experimental findings. A fluence threshold of $10^{10}\,\mathrm{cm}^{-2}$ for $\sim 100\,\mathrm{MeV}$ protons in PSDs was estimated, above which the proton tracks will overlap and increase the quenching. The general quenching models are inapplicable above such a limit as it contradicts the implicit assumption that quenching occurs in tracks independently of each other.

The possibility of exploiting the quenching in different PSDs to measure the LET was investigated without success for the low-LET proton beams.

Future work

The experimental and theoretical quenching corrections for PSDs in ion beams can be improved further to facilitate new applications:

Benchmarking: The `ExcitonQuenching` calculated luminescence when ions heavier than lithium are completely stopped in an organic bulk scintillator showed a discrepancy relative to measurements. The experimental results are, however, several decades old and were performed with bulk volumes which may lead to significant self-absorption. `ExcitonQuenching` could potentially be benchmarked in heavy ion beams against new measurements with PSDs.

The luminescence and quenching of inorganic scintillators is yet to be investigated with `ExcitonQuenching` although some studies report an over-response in inorganic scintillators exposed to α-particles.

Additional results: The use of two different—in terms of quenching—PSDs in high-LET ion beams can be used to estimate the LET in a point which may be used for quality assurance (QA) in combination with anthropomorphic phantoms: the estimation of the LET in points of a spread-out Bragg peak (SOBP) in the phantom can be compared to LET values from the TPS simulation, which would be beneficial for RBE modelling. Nonetheless, such LET estimations require experiments with smaller measurement uncertainties than what was presented in section 5.4, which would be feasible in the plateau region of a high-LET beam.

Calorimetry

The in-house developed graphite calorimeter with two active graphite cores is applicable to correct the quenching in PSDs with a high degree of reproducibility. A heat transfer analysis with a finite element method tool shows that the design minimizes the radiative transfer, convection, and conduction to the surroundings. The heat loss correction is less than 1 % for 3 Gy deposited in 0.7 s when the re-absorbance of the heat transfer is taken into account. The next immediate task is to establish traceability to the calorimeter in order to relate the measured voltage to an absorbed dose to graphite.

The dimensions of the smaller graphite core is currently unnecessarily large compared to a typical PSD, where a smaller graphite core would reduce the volume averaging corrections required to calculate the quenched PSD response. However, the current graphite core dimensions match exactly the size of three stacked alanine pellets. The combination of measurements with the alanine pellets and the graphite core would enable a transfer of the dose from the calorimeter via the stacked alanine pellets.

Bibliography

Agostinelli S et al. (2003). `Geant4` – A simulation toolkit. *Nuclear Instruments and Methods in Physics Research, Section A* **506**(3), 250–303.

Almhagen E, DJ Boersma, H Nyström, and A Ahnesjö (2018). A beam model for focused proton pencil beams. *Physica Medica* **52**, 27–32.

Almond PR, PJ Biggs, BM Coursey, W Hanson, MS Huq, R Nath, and D Rogers (1999). AAPM's TG-51 protocol for clinical reference dosimetry of high-energy photon and electron beams. *Medical Physics* **26**, 1847–1870.

Alsanea F and S Beddar (2017). Evaluating analytical ionization quenching correction models for 3D liquid organic scintillator detector. *Journal of Physics: Conf. Series* **847**(012022).

Alsanea F, F Therriault-Proulx, G Sawakuchi, and S Beddar (2018). A real-time method to simultaneously measure linear energy transfer and dose for proton therapy using organic scintillators. *Medical Physics* **45**(4), 1782–1789.

Andersen CE, SK Nielsen, JC Lindegaard, and K Tanderup (2009). Time-resolved *in vivo* luminescence dosimetry for online error detection in pulsed dose-rate brachytherapy. *Medical Physics* **36**(11), 5033–5043.

Andreo P, DT Burns, K Hohlfeld, MS Huq, T Kanai, F Laitano, V Smyth, and S Vynckier (2000). *Absorbed dose determination in external beam radiotherapy: an international code of practice for dosimetry based on standards of absorbed dose to water*. Vienna: International Atomic Energy Agency, Technical Report Series 398.

Andreo P, DT Burns, AE Nahum, J Seuntjens, and FH Attix (2017). *Fundamentals of ionizing radiation dosimetry*. John Wiley & Sons.

Archambault L, AS Beddar, L Gingras, R Roy, and L Beaulieu (2006). Measurement accuracy and Čerenkov removal for high performance, high spatial resolution scintillation dosimetry. *Medical Physics* **33**(1), 128–135.

ASTM (2003). *Standard practice for use of calorimetric dosimetry systems for electron beam dose measurements and routine dosimeter calibration*. Tech. rep. West Conshohocken, PA: American Society for Testing and Materials.

Attix FH (1986). *Introduction to radiological physics and radiation dosimetry*. New York: John Wiley & Sons.

Avdeichikov V, B Jakobsson, VA Nikitin, PV Nomokonov, and A Wegner (2002). Systematics in the light response of BGO, CsI(Tl) and GSO(Ce) scintillators to charged particles. *Nuclear Instruments and Methods in Physics Research, Section A* **484**(1-3), 251–258.

Beddar AS, TR Mackie, and FH Attix (1992a). Čerenkov light generated in optical fibres and other light pipes irradiated by electron beams. *Physics in Medicine and Biology* **37**(4), 925–935.

— (1992b). Water-equivalent plastic scintillation detectors for high-energy beam dosimetry: I. Physical characteristics and theoretical considerations. *Physics in Medicine and Biology* **37**(10), 1883–1900.

— (1992c). Water-equivalent plastic scintillation detectors for high-energy beam dosimetry: II. Properties and measurements. *Physics in Medicine and Biology* **37**(10), 1901–1913.

Beddar AS and L Beaulieu (2016). *Scintillation Dosimetry*. Boca Raton, FL: CRC Press.

Beddar AS, N Suchowerska, and SH Law (2004). Plastic scintillation dosimetry for radiation therapy: Minimizing capture of Cerenkov radiation noise. *Physics in Medicine and Biology* **49**(5), 783–790.

Beierholm AR, RO Ottosson, LR Lindvold, CF Behrens, and CE Andersen (2011). Characterizing a pulse-resolved dosimetry system for complex radiotherapy beams using organic scintillators. *Physics in Medicine and Biology* **56**(10), 3033–3045.

Bertolet A, A Baratto-Roldán, M Cortés-Giraldo, and A Carabe-Fernandez (2019). Segment-averaged LET concept and analytical calculation from microdosimetric quantities in proton radiation therapy. *Medical Physics*, In Press.

Bethe HA (1930). Zur theorie des durchgangs schneller korpuskularstrahlen durch materie. *Annalen der Physik* **397**(3), 325–400.

— (1932). Bremsformel für Elektronen relativistischer Geschwindigkeit. *Zeitschrift für Physik* **76**(5), 293–299.

Birks JB (1951). Scintillation from organic crystals: Specific flourescence and relative response to different radiation. *Proceedings of the Physical Society Section A* **64**(10), 874–877.

— (1964). *The theory and practice of scintillation counting: International series of monographs in electronics and instrumentation*. London: Pergamon Press Ltd.

Blanc D, F Cambou, and YGD Lafond (1962). Kinetics of the fast component of scintillation in a pure organic medium. Application to anthracene. *Comptes rendus de l'Académie des Sciences Paris* **18**, 3187–3189.

— (1964). Etude cinétique de la scintillation dans les cristaux organiques purs. *Journal de Physique* **25**, 319–325.

Blue J and D Liu (1962). Scintillation Response of Alkali Iodides to Alpha Particles and Protons. *IEEE Transactions on Nuclear Science* **9**(3), 48–51.

Bohr N (1913). On the theory of the decrease of velocity of moving electrified particles on passing through matter. *The London, Edinburgh, and Dublin Philosophical Magazine and Journal of Science* **25**(145), 10–31.

— (1915). On the decrease of velocity of swiftly moving electrified particles in passing through matter. *The London, Edinburgh, and Dublin Philosophical Magazine and Journal of Science* **30**(178), 581–612.

Boivin J, S Beddar, C Bonde, D Schmidt, W Culberson, M Guillemette, and L Beaulieu (2016). A systematic characterization of the low-energy photon response of plastic scintillation detectors. *Physics in Medicine and Biology* **61**(15), 5569–5586.

Bortfeld T (1997). An analytical approximation of the Bragg curve for therapeutic proton beams. *Medical Physics* **24**(12), 2024–33.

Bragg WH and R Kleeman (1904). On the ionization curves of radium. *The London, Edinburgh, and Dublin Philosophical Magazine and Journal of Science* **8**(48), 726–738.

— (1905). On the α particles of radium and their loss of range in passing through various atoms and molecules. *The London, Edinburgh, and Dublin Philosophical Magazine and Journal of Science* **10**(57), 318–340.

Bray F, J Ferlay, I Soerjomataram, RL Siegel, LA Torre, and A Jemal (2018). Global cancer statistics 2018: GLOBOCAN estimates of incidence and mortality worldwide for 36 cancers in 185 countries. *CA: a cancer journal for clinicians* **68**(6), 394–424.

Buenerd M, DL Hendrie, U Jahnke, J Mahoney, A Menchaca-Rocha, C Olmer, and DK Scott (1976). Response of pilot U scintillator to heavy ions. *Nuclear Instruments and Methods* **136**(1), 173–177.

Butts J and R Katz (1967). Theory of RBE for heavy ion bombardment of dry enzymes and viruses. *Radiation Research* **30**(4), 855–871.

Čerenkov PA (1934). Visible emission of clean liquids by action of γ radiation. *Doklady Akademii Nauk USSR* **2**, 451.

— (1937). Visible radiation produced by electrons moving in a medium with velocities exceeding that of light. *Physical Review* **52**(4), 378–379.

Chatterjee A and HJ Schaefer (1976). Microdosimetric structure of heavy ion tracks in tissue. *Radiation and Environmental Biophysics* **13**(3), 215–227.

Chauvie S, Z Francis, S Guatelli, S Incerti, B Mascialino, G Montarou, P Moretto, P Nieminen, and MG Pia (2006). Monte Carlo simulation of interactions of radiation with biological systems at the cellular and DNA levels: the `Geant4`-DNA project. *Radiation Research* **166**, 676–677.

Chou CN (1952). The nature of the saturation effect of fluorescent scintillators. *Physical Review Letters* **5**(87), 904–905.

Cortés-Giraldo MA and A Carabe (2015). A critical study of different Monte Carlo scoring methods of dose average linear-energy-transfer maps calculated in voxelized geometries irradiated with clinical proton beams. *Physics in Medicine and Biology* **60**(7), 2645–2669.

Cucinotta FA, H Nikjoo, and DT Goodhead (1999). Applications of amorphous track models in radiation biology. *Radiation and Environmental Biophysics* **38**(2), 81–92.

Despeignes V (1896). Observation concernant un cas de cancer de l'estomac traité par les rayons Röntgen. *Lyon Médical: Gazette Médicale et Journal de Médecine Réunis*, 428–430.

Ekstrabladet (1932). *Elektron-disputatsen*. November 29, Copenhagen.

Emfietzoglou D, R Garcia-Molina, I Kyriakou, I Abril, and H Nikjoo (2009). A dielectric response study of the electronic stopping power of liquid water for energetic protons and a new *I*-value for water. *Physics in Medicine and Biology* **54**(11), 3451–3472.

Frank I and I Tamm (1937). Coherent visible radiation from fast electrons passing through matter. *Proceedings of the USSR Academy of Sciences* **14**, 109–114.

Galanin M and Z Chizhikova (1958). The quenching of luminescence of organic substances at the alpha-excitation. *Optika i Spektroskopiya* **4**(2), 196–202.

Geiß OB, M Krämer, and G Kraft (1998). Efficiency of thermoluminescent detectors to heavy charged particles. *Nuclear Instruments and Methods in Physics Research, Section B* **142**(4), 592–598.

Grassberger C and H Paganetti (2011). Elevated LET components in clinical proton beams. *Physics in Medicine and Biology* **56**(20), 6677–6691.

Greilich S, L Grzanka, N Bassler, CE Andersen, and O Jäkel (2010). Amorphous track models: A numerical comparison study. *Radiation Measurements* **45**(10), 1406–1409.

Grubbé EH (1949). *X-ray Treatment: Its Origin, Birth and Early History*. Bruce Publishing Company.

Grün R, T Friedrich, E Traneus, and M Scholz (2018). Is the dose-averaged LET a reliable predictor for the relative biological effectiveness? *Medical Physics* **46**(2), 1064–1074.

Grzanka L, O Ardenfors, and N Bassler (2018). Monte carlo simulations of spatial let distributions in clinical proton beams. *Radiation Protection Dosimetry* **180**(1-4), 296–299.

Hansen JW and KJ Olsen (1984). Experimental and calculated response of a radiochromic dye film dosimeter to high-LET radiations. *Radiation Research* **97**(1), 1–15.

Helo Y, A Kacperek, I Rosenberg, G Royle, and AP Gibson (2014). The physics of Čerenkov light production during proton therapy. *Physics in Medicine and Biology* **59**(23), 7107–7123.

Hoehr C, C Lindsay, J Beaudry, C Penner, V Strgar, R Lee, and C Duzenli (2018). Characterization of the exradin W1 plastic scintillation detector for small field applications in proton therapy. *Physics in Medicine and Biology* **63**(9).

ICRU (1970). *Linear Energy Transfer (Report 16)*. Washington, DC: International Commission on Radiation Units and Measurements.

— (1993). *Stopping Powers and Ranges for Protons and Alpha Particles (Report 49)*. Bethesda, MD: International Commission on Radiation Units and Measurements.

— (1998). *Clinical proton dosimetry part I: beam production, beam delivery and measurement of absorbed dose (Report 59)*. Bethesda, MD: International Commission on Radiation Units and Measurements.

— (2005). *Stopping of Ions Heavier Than Helium (Report 73)*. Bethesda, MD: International Commission on Radiation Units and Measurements.

Ionita CE, D Radu, and I Astefanoaei (2013). 3D-modelling of temperature gradients induced by electrical power dissipation in a 3-body Domen-type calorimeter for absorbed dose measurements. *Materials Science and Engineering B: Solid-State Materials for Advanced Technology* **178**(19), 1275–1284.

Jaffé G (1913). Zur Theorie der Ionisation in Kolonnen. *Annalen der Physik* **347**(12), 303–344.

Jain A, C Blum, and V Subramaniam (2009). *Fluorescence Lifetime Spectroscopy and Imaging of Visible Fluorescent Proteins*. Elsevier, 147–176.

Jang KW, WJ Yoo, JK Seo, JY Heo, J Moon, JY Park, EJ Hwang, D Shin, and P J (2012). Fiber-optic Čerenkov radiation sensor for proton therapy dosimetry. *Optics Express* **20**(13), 13907–13914.

Jelley JV (1958). *Čerenkov radiation and its applications*. London: Pergamon.

Johansen JG, S Rylander, S Buus, L Bentzen, SB Hokland, CS Søndergaard, AKM With, G Kertzscher, and K Tanderup (2018). Time-resolved in vivo dosimetry for source tracking in brachytherapy. *Brachytherapy* **17**(1), 122–132.

Kallmann H and GJ Brucker (1957). Decay times of fluorescent substances excited by high-energy radiation. *Physical Review* **108**(5), 1122–1130.

Katz R and MN Varma (1991). *Radial distribution of dose*. Boston: Springer, 163–180.

Kertzscher G, A Rosenfeld, S Beddar, K Tanderup, and JE Cygler (2014). In vivo dosimetry: Trends and prospects for brachytherapy. *British Journal of Radiology* **87**(1041), 1–16.

Kiefer J and H Straaten (1986). A model of ion track structure based on classical collision dynamics. *Physics in Medicine and Biology* **31**(11), 1201–1209.

Knoll GF (2010). *Radiation detection and measurement*. Hoboken, NJ: John Wiley & Sons.

Kragh H (1992). Relativistic Collisions. The Work of Christian Møller in the Early 1930s. *Archive of the History of Exact Sciences* **43**, 299–328.

Lindvold LR, AR Beierholm, and CE Andersen (2010). An organic dye in a polymer matrix – A search for a scintillator with long luminescent lifetime. *Radiation Measurements* **45**(3-6), 615–617.

McEwen MR (2002). "Development of a Portable Graphite Calorimeter for Measuring Absorbed dose in the radiotherapy clinic". PhD Thesis. University of Surrey.

McEwen MR and S Duane (2000). A portable calorimeter for measuring absorbed dose in the radiotherapy clinic. *Physics in Medicine and Biology* **45**(12), 3675–3691.

Medin J (2010). Implementation of water calorimetry in a 180 MeV scanned pulsed proton beam including an experimental determination of k_Q for a Farmer chamber. *Physics in Medicine and Biology* **55**(12), 3287–3298.

Michaelian K and A Menchaca-Rocha (1994). Ion-Induced Luminescence Based on Energy Deposition. *Physical Review B* **49**(22), 550–562.

Michaelian K, A Menchaca-Rocha, and E Belmont-Moreno (1995). Scintillation response of nuclear particle detectors. *Nuclear Instruments and Methods in Physics Research, Section A* **356**, 297–303.

Miller A and A Kovacs (1985). Calorimetry at industrial electron accelerators. *Nuclear Instruments and Methods in Physics Research, Section B* **10-11**, 994–997.

Møller C (1932). Zur Theorie des Durchgangs schneller Elektronen durch Materie. *Annalen der Physik* **406**(5), 531–585.

Morgan RV, RS Reid, AM Baker, B Lucero, and JD Bernardin (2017). *Emissivity measurements of additively manufactured materials*. Tech. rep. Los Alamos National Lab, Los Alamos, NM, USA.

Murray RB and A Meyer (1961). Scintillation response of activated inorganic crystals to various charged particles. *Physical Review* **122**(3), 815–826.

Ogawa T, T Yamaki, and T Sato (2018). Analysis of scintillation light intensity by microscopic radiation transport calculation and Förster quenching model. *PLoS ONE* **13**(8), 1–19.

Otuka N, E Dupont, V Semkova, B Pritychenko, A Blokhin, M Aikawa, S Babykina, M Bossant, G Chen, and S Dunaeva (2014). Towards a more complete and accurate experimental nuclear reaction data library (EXFOR): International collaboration between nuclear reaction data centres. *Nuclear Data Sheets* **120**, 272–276.

Paganetti H, A Niemierko, M Ancukiewicz, LE Gerweck, M Goitein, JS Loeffler, and HD Suit (2002). Relative Biological Effectiveness (RBE) values for proton beam therapy. *Int. J. Radiation Oncology Biol. Phys* **53**(2), 407–421.

Palmans H, R Thomas, M Simon, S Duane, A Kacperek, A DuSautoy, and F Verhaegen (2004). A small-body portable graphite calorimeter for dosimetry in low-energy clinical proton beams. *Physics in Medicine and Biology* **49**(16), 3737–3749.

Paul H (2010). Recent results in stopping power for positive ions, and some critical comments. *Nuclear Instruments and Methods in Physics Research, Section B* **268**(22), 3421–3425.

Paul H and A Schinner (2001). An empirical approach to the stopping power of solids and gases for ions from Li to Ar. *Nuclear Instruments and Methods in Physics Research, Section B* **179**(3), 299–315.

— (2002). An empirical approach to the stopping power of solids and gases for ions from Li to Ar – Part II. *Nuclear Instruments and Methods in Physics Research, Section B* **195**(1-2), 166–174.

Pedroni E, S Scheib, T Böhringer, A Coray, M Grossmann, S Lin, and A Lomax (2005). Experimental characterization and physical modelling of the dose distribution of scanned proton pencil beams. *Physics in Medicine and Biology* **50**(3), 541–561.

Picard S, DT Burns, and P Roger (2009). *Construction of an absorbed-dose graphite calorimeter*. Tech. rep. Sèvres Cedex: BIPM.

PTCOG (2019). *Particle therapy facilities in clinical operation*. URL: `https://www.ptcog.ch/` (visited on 14/07/2019).

Röntgen WC (1895). Über eine neue Art von Strahlen. Vorläufige Mitteilung. *Aus den Sitzungsberichten der Würzburger Physik.-medic. Gesellschaft Würzburg*, 137–147.

Rosling H (2018). *Ten Reasons We're Wrong About the World—And Why Things Are Better Than You Think*. London: Sceptre.

Ross CK and NV Klassen (1996). Water calorimetry for radiation dosimetry. *Physics in Medicine and Biology* **41**(1), 1–29.

Rutherford E (1911). The scattering of α and β particles by matter and the structure of the atom. *The London, Edinburgh, and Dublin Philosophical Magazine and Journal of Science* **21**(125), 669–688.

Santurio GV (2019). "Dosimetry for new radiotherapy modalities: Towards improved traceability for scintillator dosimetry in small MV photon beams". PhD thesis. Technical University of Denmark.

Scholz M and G Kraft (1996). Track structure and the calculation of biological effects of heavy charged particles. *Advances in space research: the official journal of the Committee on Space Research* **18**(1-2), 5–14.

Sibczyński P et al. (2018). Non-proportionality of GAGG:Ce scintillators down to 50 eV electron equivalent by application of alpha particle excitation. *Nuclear Instruments and Methods in Physics Research, Section A* **898**, 24–29.

Sibolt P, CE Andersen, W Ottosson, and CF Behrens (2017). Time-resolved plastic scintillator dosimetry in a dynamic thorax phantom. *Radiation Measurements* **106**, 373–377.

Sigmund P (2000). Stopping power: Wrong terminology. *ICRU News* **16**(1), 1–3.

— (2006). *Particle Penetration and Radiation Effects: General Aspects and Stopping of Swift Point Charges*. Vol. 151. Berlin.

— (2014). *Particle Penetration and Radiation Effect: Penetration of Atomic and Molecular Ions*. Vol. 179. Berlin.

Sørensen BS, J Overgaard, and N Bassler (2011). In vitro RBE-LET dependence for multiple particle types. *Acta Oncologica* **50**(6), 757–762.

Tanderup K, S Beddar, CE Andersen, G Kertzscher, and JE Cygler (2013). In vivo dosimetry in brachytherapy. *Medical Physics* **40**(7), 1–15.

Therriault-Proulx F, L Beaulieu, L Archambault, and S Beddar (2013). On the nature of the light produced within PMMA optical light guides in scintillation fiber-optic dosimetry. *Physics in Medicine and Biology* **58**(7), 2073–2084.

Thomson J (1899). On the theory of the conduction of electricity through gases by charged ions. *The London, Edinburgh, and Dublin Philosophical Magazine and Journal of Science* **47**(286), 253–268.

Thomson J (1912). Ionization by moving electrified particles. *The London, Edinburgh, and Dublin Philosophical Magazine and Journal of Science* **23**(136), 449–457.

Toftegaard J, A Lühr, N Sobolevsky, and N Bassler (2014). Improvements in the stopping power library `libdEdx` and release of the web GUI `dedx.au.dk`. *Journal of Physics: Conference Series* **489**(1), 012003.

Torrisi L (2000). Plastic scintillator investigations for relative dosimetry in proton-therapy. *Nuclear Instruments and Methods in Physics Research, Section B* **170**(3), 523–530.

Voltz R, JL da Silva, G Laustriat, and A Coche (1966). Influence of the nature of ionizing particles on the specific luminescence of organic scintillators. *The Journal of Chemical Physics* **45**(9), 3306–3311.

Vynckier S, DE Bonnett, and DT Jones (1991). Code of practice for clinical proton dosimetry. *Radiotherapy and Oncology* **20**(1), 53–63.

Wagener DT (2009). *The history of oncology*. Bohn Stafleu van Loghum.

Wang H and ON Vassiliev (2017). Radial dose distributions from protons of therapeutic energies calculated with `Geant4`-DNA. *Physics in Medicine and Biology* **62**(10), 219–227.

Wang LL, LA Perles, L Archambault, N Sahoo, D Mirkovic, and S Beddar (2012). Determination of the quenching correction factors for plastic scintillation detectors in therapeutic high-energy proton beams. *Physics in Medicine and Biology* **57**(23), 7767–7781.

WHO (2019). *Global Health Observatory data*. URL: `https://www.who.int/gho/database/en/` (visited on 03/08/2019).

Wilson RR (1946). Radiological use of fast protons. *Radiology* **47**(5), 487–491.

Wootton L, R Kudchadker, A Lee, and S Beddar (2014). Real-time in vivo rectal wall dosimetry using plastic scintillation detectors for patients with prostate cancer. *Physics in Medicine and Biology* **59**(3), 647–660.

Ziegler JF, MD Ziegler, and JP Biersack (2010). SRIM – The stopping and range of ions in matter. *Nuclear Instruments and Methods in Physics Research, Section B* **268**(11-12), 1818–1823.

Part II

Publications

Paper I

Title:

Quenching-free fluorescence signal from plastic-fibres in proton dosimetry: understanding the influence of Čerenkov radiation.

Authors:

Christensen JB, Almhagen E, Nyström H and Andersen CE

Submitted to:

Physics in Medicine and Biology,
September 2017.

Status:

Published March 2018.

Digital Object Identifier:

10.1088/1361-6560/aaafad

IOP Publishing Phys. Med. Biol. 63 (2018) 065001 (10pp) https://doi.org/10.1088/1361-6560/aaafad

Physics in Medicine & Biology

IPEM Institute of Physics and Engineering in Medicine

RECEIVED
29 September 2017

REVISED
8 February 2018

ACCEPTED FOR PUBLICATION
15 February 2018

PUBLISHED
9 March 2018

PAPER

Quenching-free fluorescence signal from plastic-fibres in proton dosimetry: understanding the influence of Čerenkov radiation

Jeppe Brage Christensen[1,4], **Erik Almhagen**[2,3], **Håkan Nyström**[3] **and Claus E Andersen**[1]

[1] Center for Nuclear Technologies, Technical University of Denmark, Roskilde, Denmark
[2] Medical Radiation Sciences, Department of Immunology, Genetics and Pathology, Uppsala University, Uppsala, Sweden
[3] The Skandion Clinic, Uppsala, Sweden
[4] Author to whom any correspondence should be addressed.

E-mail: jepb@dtu.dk

Keywords: ionization quenching, dosimetry, fluorescence, Čerenkov radiation, proton therapy, quenching-free

Abstract

The origin of photons emitted in optical fibres under proton irradiation has been attributed to either entirely Čerenkov radiation or light consisting of fluorescence with a substantial amount of Čerenkov radiation. The source of the light emission is assessed in order to understand why the signal from optical fibres irradiated with protons is reportedly quenching-free.

The present study uses the directional emittance of Čerenkov photons in 12 MeV and 20 MeV electron beams to validate a Monte Carlo model for simulating the emittance and transmission of Čerenkov radiation in optical fibres.

We show that fewer than 0.01 Čerenkov photons are emitted and guided per 225 MeV proton penetrating the optical fibre, and that the Čerenkov signal in the optical fibre is completely negligible at the Bragg peak. Furthermore, on taking the emittance and guidance of both fluorescence and Čerenkov photons into account, it becomes evident that the reported quenching-free signal in PMMA-based optical fibres during proton irradiation is due to fluorescence.

1. Introduction

Dosimetry with fibre-coupled organic scintillators is known to benefit from near water-equivalence, high spatial resolution, and good energy independence (Beddar *et al* 1992b, 1992c, De Boer *et al* 1993, Beddar and Beaulieu 2016). The temperature dependent light output (Buranurak *et al* 2013, Wootton and Beddar 2013) and stem effect (Archambault *et al* 2006, Marckmann *et al* 2006, Therriault-Proulx *et al* 2011, 2013) can be accounted for in different ways. Nonetheless, the non-linear response exhibited by organic scintillators exposed to particles with a high linear energy transfer (LET) remains challenging, and the underlying mechanisms are poorly understood. This signal reduction, termed ionization quenching, is often corrected by applying the semi-empirical formula developed by Birks (1951), but a recent study (Boivin *et al* 2016) questions the applicability of this correction method in low-energy photon beams, which motivates different approaches.

An attempt to circumvent the quenching issue was made by irradiation of a bare optical fibre in a 180 MeV proton beam (Jang *et al* 2012). The resulting signal resembled the reference depth-dose measured with an ionization chamber perfectly, without any LET-dependent signal reduction—i.e. quenching-free. However, the signal in the optical fibre was at first entirely attributed to Čerenkov radiation, rather than fluorescence.

Čerenkov radiation—the emission of optical photons by a charged particle travelling through a dielectric medium with an energy above a material-dependent threshold—differs from fluorescence by having a characteristic emission angle depending on the kinetic energy and material (Jelley 1958, Beddar *et al* 1992a). Consequently, the measurement of Čerenkov photons within an optical fibre is angle-dependent, in contrast to the isotropic emission of fluorescence.

The interpretation of the optical signal to be entirely Čerenkov radiation was partly corrected by Darafsheh *et al* (2016), who concluded that the signal mainly consists of fluorescence but is also heavily *Čerenkov contaminated*.

A deeper understanding of the fluorescence and Čerenkov radiation is of interest, since it finds several applications in radiation therapy dosimetry; Glaser *et al* (2013) used Čerenkov emission in water to obtain accurate dose profiles in megavoltage x-ray photon beams, while Helo *et al* (2014b) developed a quality assurance method using Čerenkov radiation in a water tank exposed to therapeutic electron beams. Helo *et al* (2014a) suggest imaging the Čerenkov Bragg peak following proton therapy. Demers *et al* (2013), Jarvis *et al* (2014), and Lin *et al* (2016) investigated the possibilities of tomography and sensing tumours during radiotherapy using Čerenkov excited fluorescence. However, the main emphasis in this work is to understand and utilize the quenching-free signal reported in Jang *et al* (2012) as optical fibres are irradiated with protons.

Protons at clinically relevant energies are below the Čerenkov energy threshold in water and plastic-like materials, but give rise to Čerenkov radiation as secondary particles are liberated via Coulomb interactions, by production of positron and electron emitting isotopes, and via interactions in which the proton transfers energy to charged or uncharged particles Helo *et al* (2014a) . The Čerenkov radiation following the said processes in a proton beam exhibits a broad angular distribution due to the particle scattering and Čerenkov radiation following isotropic decays. The angular distribution makes it challenging to measure the emitted optical Čerenkov photons using e.g. an optical fibre, since the majority of the emitted optical photons will be absorbed in the optical fibre rather than guided to a photomultipler tube (PMT).

The number of Čerenkov photons per primary in an electron beam generally exceeds that of a proton beam by more than an order of magnitude (Glaser *et al* 2014) for water and plastic-materials. Additionally, the emittance of Čerenkov photons in electron beams has a narrower angular distribution than in proton beams, which makes the Čerenkov photons in electron beams easier to measure using an optical fibre with a limited acceptance angle.

The present study utilizes the relative directional emittance of Čerenkov photons in 12 MeV and 20 MeV electron beams to validate a Monte Carlo model for the emittance and transmission of Čerenkov photons in optical fibres. The model is validated against experimental results obtained in therapeutic electron beams. The Monte Carlo implementation is subsequently used to investigate Čerenkov radiation and fluorescence in water and optical fibres exposed to proton beams, with emphasis on the number of fluorescence and Čerenkov photons emitted within the acceptance cone of the fibre per primary particle. The Monte Carlo simulations of fluorescence and Čerenkov radiation in a proton beam is eventually compared to the experimental results.

2. Materials and methods

2.1. Theory

Čerenkov radiation was first observed by Čerenkov (1937), explained theoretically by Frank and Tamm (1937), and is characterized by optical photons emitted by charged particles exceeding the phase velocity of light in a dielectric medium. The refractive index-dependent energy threshold is given as

$$E_{\mathrm{TH}} = m_0 c^2 \left(\frac{1}{\sqrt{1 - n^{-2}}} - 1 \right) \tag{1}$$

for a particle of rest-mass m_0, where n is the average refractive index of the dielectric material, and c the speed of light in vacuum (Jelley 1958). Consequently, the energy threshold for electrons in poly(methyl methacrylate) (PMMA) ($n = 1.49$) and water ($n = 1.33$) is 178 keV and 264 keV respectively. As protons are ~1836 times heavier than electrons, the Čerenkov energy thresholds for protons in PMMA and water are above clinically relevant energies. However, protons above 80 MeV in PMMA and 115 MeV in water (Glaser *et al* 2014) may liberate electrons above the Čerenkov energy threshold, and at lower energies via nuclear interactions.

The number $\mathrm{d}N$ of optical photons emitted by an electron with energy E within the spectral region defined by wavelengths $\lambda_1 < \lambda_2$, traversing a distance $\mathrm{d}x$, is given by the Frank–Tamm formula (Jelley 1958) as

$$\frac{\mathrm{d}N}{\mathrm{d}x} = 2\pi\alpha \left(\frac{1}{\lambda_1} - \frac{1}{\lambda_2} \right) \sin^2 \theta, \tag{2}$$

where $\alpha = 1/137$ is the fine structure constant, and

$$\theta = \arccos\left(\frac{1}{\beta n} \right), \qquad \text{for} \quad \beta = \sqrt{1 - \left(\frac{m_0 c^2}{E + m_0 c^2} \right)^2} \tag{3}$$

is the angle at which the optical Čerenkov photons are emitted relative to the direction of the electron. The angular dependency is crucial for the present case, where the light must be guided through optical fibres—requiring the emitted optical photons to be within the acceptance cone of the fibre in question. The spectral intensity distribution in equation (2) and the angular dependency in equation (3) make it feasible to confirm the presence of Čerenkov radiation experimentally.

2.2. Experimental set-up

The study uses a 15 m optical fibre with 480 μm diameter PMMA core and fluorinated polymer ($n = 1.40$) as cladding with a 500 μm outer diameter (GH-4001-P, Mitsubishi Rayon Co., Ltd., Japan). A black polyethylene fibre-jacket protected the cladding and core, with an outer diameter of 1000 μm, from external light.

The optical fibre was irradiated with 12 MeV and 20 MeV electrons at a medical linac (TrueBeam, Varian Medical Systems, USA) where the attached SMA-connector was connected to an ME-40 device with two PMTs (Beierholm *et al* 2014). An in-house built x-ray source (Andersen *et al* 2003) was used to irradiate the bare optical fibre with 50 kVp photons.

Optical spectra of the light transmitted through the fibre under irradiation with protons and electrons were obtained with a monochromator (Model 77250, Oriel Instruments, USA) placed outside the treatment room. The acquisition time for all spectra was set to 15 min to compensate for the low optical signal as the fibre was irradiated with 50 kVp x-ray, and kept for consistency during electron irradiation. The monochromator was connected to a photomultiplier tube (MP-982, PerkinElmer, USA) coupled to a laptop with data acquisition software. Measurements of the optical spectra and the optical signal as a function of gantry angle were conducted with the fibres suspended in air whereas the depth curves were simulated and measured in water.

A 180 MeV spot-scanning proton beam (Proteus 235, IBA, Belgium) at the Skandion Clinic, Uppsala, was used to irradiate the optical fibre placed in a water phantom (Blue Phantom, IBA Dosimetry, Germany) with a 41×41 spots in a $10\ \text{cm} \times 10\ \text{cm}$ field. A 180 MeV spot had a full width at half maximum (FWHM) of 9.4 mm, and each spot was delivered in approximately 22 ms. An ionization chamber (Bragg Peak Ionization Chamber No. 34070, PTW Freiburg, Germany) was used to measure the reference depth-dose curve.

The 180 MeV energy is chosen for the experimental irradiations for comparisons with Jang *et al* (2012) and Darafsheh *et al* (2016) whereas 225 MeV, with the most Čerenkov radiation per primary, is chosen for the simulations to investigate the so-called Čerenkov contamination referred to by Darafsheh *et al* (2016).

2.2.1. *Monte Carlo parameters*

The number of emitted fluorescence photons per unit energy in the optical fibre is required as an input in GEANT4. This number was estimated by comparing the outputs of a fibre-coupled scintillator irradiated with equal doses at (i) a point in the scintillator and (ii) a point in the optical fibre 1 cm from the scintillator, giving a negligible difference in the fibre transmission lengths. The irradiations took place in a ^{60}Co source (Terabalt T100, UJP Praha, Czech Republic), where the fiber-coupled scintillator was placed at angle relative to the ^{60}Co beam direction, to favour the absorption of Čerenkov photons in the optical fibre rather than guidance. The scintillator (BCF-60, Saint-Gobain, France) yields 7100 photons MeV^{-1} according to the manufacturer, which allowed an estimation of the number of fluorescence photons per unit deposited energy. The estimate was subsequently used as a lower threshold of the amount of fluorescence photons being guided in the optical fibre in section 3.5.

A fibre-subtraction method, as described in Jang *et al* (2012), was used to validate the Monte Carlo code against experimentally obtained results. The set-up is sketched in figure 1, where the Čerenkov radiation in 5 cm of the irradiation field is estimated by subtracting the signal in one fibre from that in another. The two bare optical fibres are each connected to a PMT in the ME-40 set-up with same gain.

2.3. Monte Carlo simulations

The dose deposition, spatial distribution, and guidance of Čerenkov photons in water and the optical fibres were investigated with the Monte Carlo software GEANT4 10.2 (Agostinelli *et al* 2003). The optical Čerenkov photons were generated in the waveband 380 nm–700 nm where the refractive indices for water, PMMA and fluorinated polyethylene (cladding material) were set to be spectrally constant as 1.33, 1.49 and 1.40 respectively. Fluorescence photons were generated in the same waveband as Čerenkov radiation, with a spectral distribution in the optical fibre as in De Boer *et al* (1993). The number of emitted fluorescence photons per energy was for this particular optical fibre estimated to be 340 photons MeV^{-1}—see the procedure in section 2.2.

The standard electromagnetic package with `option4` was used along with the `QGSP_BIC` hadron physics package. The GEANT4 implementation of the simulated emission and scoring of Čerenkov photons was compared to and validated against results in Glaser *et al* (2014) for photons, electrons and protons in water. 10^8 primary particles were used in the case of electron beams, whereas an order of 10^9 protons was required due low number of emitted Čerenkov photons per proton in the optical fibre. Čerenkov and fluorescence emission profiles were simulated in a $1\ \text{m} \times 1\ \text{m} \times 1\ \text{m}$ water tank where the primary particles were sampled uniformly from a monoenergetic circular source with radius 2 cm placed in the middle of the tank.

The emittance and guidance of Čerenkov photons in the Monte Carlo model of the optical fibre is validated against experimental data in section 3.4.

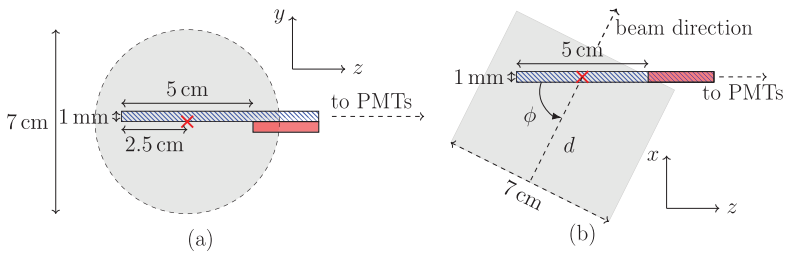

Figure 1. Fibre-subtraction method used to validate the Monte Carlo implementation where the 7 cm diameter radiation field is (a) perpendicular to the two fibres and (b) rotated an angle ϕ. Fibre 1 (hatched rectangle) and fibre 2 (filled rectangle) are separated by a 5 cm distance and each connected to a photomultiplier tube. The top-view in (b) shows the source-to-fibre distance d where the beam is rotated an angle ϕ relative to the fibres.

3. Results

3.1. Angular dependency

The Čerenkov emission angle in the optical fibre is investigated experimentally by irradiating optical fibres at different angles with 20 MeV electrons. The PMT signal as a function of gantry angle, with the angle defined as in figure 1(b), is shown in figure 2(a). The angular Čerenkov radiation peak matches the theoretical emission angle in the fibre-core (PMMA), which confirms that fluorescence is negligible relative to the Čerenkov radiation for electron beams, if the irradiation angle is chosen properly to favour the Čerenkov radiation.

3.2. Spectral distributions

Spectral distributions of the photons generated in the optical fibres exposed to electron beams are acquired at two irradiation angles, as defined in figure 2(b): one optimized for guidance of the Čerenkov radiation, and one in which the guidance is minimal—see equation (3). The Čerenkov emission angle for electrons at infinite energies ($\theta \simeq \arccos n^{-1}$) is 47.8° in PMMA, i.e. in the fibre core.

Thus, the angle between the beam and optical fibre, ϕ as chosen as in figure 1(b), is set to $\phi = 45°$ to obtain a Čerenkov spectrum, and $\phi = 135°$ for a fluorescence spectrum. The two irradiation angles are chosen to ensure that the same length of fibre is irradiated in both electron measurements, which gives rise to the same fluorescence signal. For comparison, another fluorescence spectrum was obtained by irradiating the optical fibre in a 50 kVp x-ray source, i.e. well below the Čerenkov threshold.

3.3. Čerenkov radiation in electron beams

3.3.1. Čerenkov radiation distribution

Studies (Glaser *et al* (2014), Helo *et al* (2014a)) report a small depth-shift between the dose and emission of optical Čerenkov photons as a function of the depth in electron beams, as shown in figure 3(a).

The kinetic energy of a 20 MeV electron beam in water is scored along the central axis in figure 3(b) with GEANT4 for reference, where the Čerenkov emission angle in equation (3) is plotted as a function of the energy—i.e. the emission angle relative to the beam direction if no interaction were to occur. Figure 3(c) shows the actual angles at which Čerenkov photons are emitted relative to the beam direction scored with a 500 × 500 grid in water for 20 MeV electrons. The majority of the Čerenkov photons are emitted an angle around 41.2° as predicted by equation (3).

3.4. Measured depth-profile of Čerenkov radiation

The emission of Čerenkov photons as a function of the water depth is investigated with the fibre-subtraction method sketched in figures 1(a) and (b) with an irradiation angle of $\phi = 45°$. The Čerenkov radiation in the 5 cm difference region was estimated by subtracting the smaller PMT signal from the larger. An identical set-up was implemented in GEANT4, in which only the Čerenkov radiation was scored. Depth-curves of the normalized signal difference were now experimentally obtained by mechanically moving the fibres through the water phantom, and equivalently in the Monte Carlo code with a photon counter at the fibre end. The experimental results and Monte Carlo simulations are shown in figure 4 for 12 MeV and 20 MeV electrons in water.

3.5. Čerenkov radiation and fluorescence in clinical proton beams

The emittance of optical Čerenkov photons in a proton beam is more complex to relate to the dose-profile than for electron beams. The depth profile of both dose and Čerenkov radiation is shown in figure 5(a). The Čerenkov radiation is scored in a cylinder with 1.5 cm radius along the axis of a pencil beam.

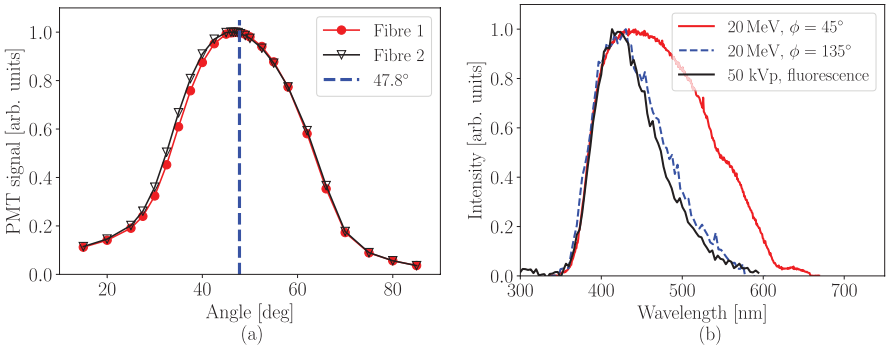

Figure 2. (a) PMT signal as a function of gantry angle as optical fibres are irradiated with 20 MeV electrons along with the theoretical emission angle in the fibre core (dashed line). (b) The fluorescence spectrum of the optical fibre obtained with a 50 kVp x-ray source, along with spectra from irradiations using 20 MeV electrons at $\phi = 45°$ (Čerenkov dominated spectrum) and $\phi = 135°$ (fluorescence spectrum) with angles chosen as in figure 1(b).

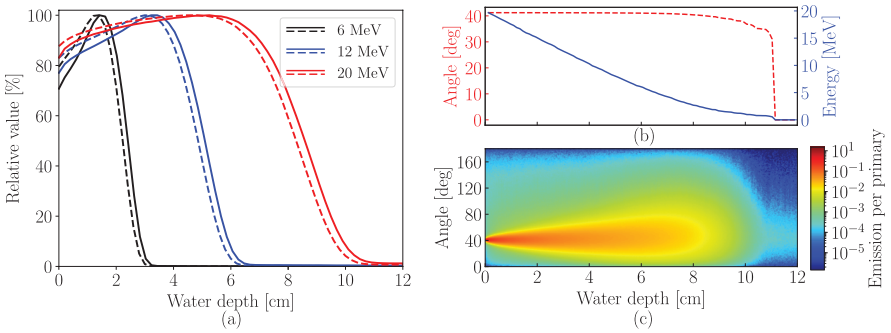

Figure 3. GEANT4 simulations of electrons in water. (a) Distribution of dose (solid lines) and emission of Čerenkov photons (dashed lines) for three energies in water. (b) Kinetic energy (solid line) scored along the central axis of a 20 MeV electron beam. The Čerenkov emission angle (dashed line) is plotted as a function of the energy for comparison. (c) Emission angle scored relative to the beam direction.

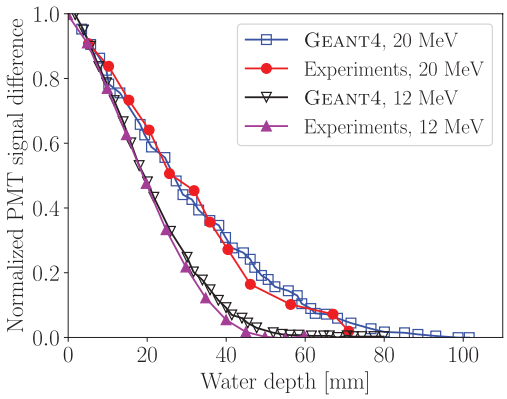

Figure 4. Fibre-subtraction method applied to experiments and Monte Carlo simulations for 12 MeV and 20 MeV electrons. The fibres were irradiated at an angle $\phi = 45°$ in a water phantom.

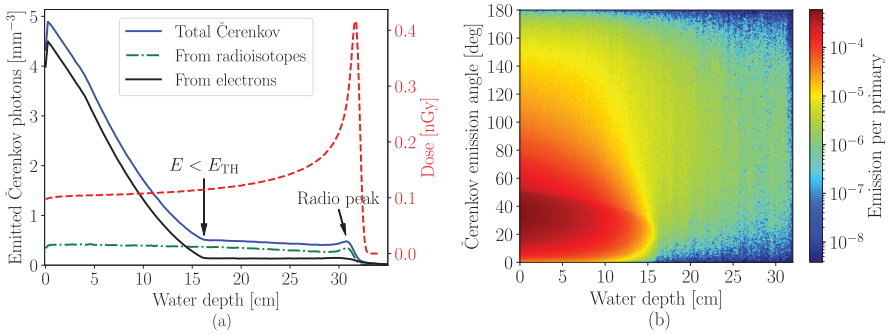

Figure 5. GEANT4 simulations of 225 MeV protons in water. (a) The majority of the Čerenkov radiation arises from liberated electrons with a spatial distribution different from the dose, although a minor radiopeak is observable at the Bragg peak. (b) Angular distribution of the emitted Čerenkov photons scored in a 500 × 500 grid relative to the beam direction reveals a broader emission distribution than in electron beams.

The first half of the range is dominated by Čerenkov photons emitted by electrons liberated by protons (Glaser *et al* (2014), Helo *et al* (2014a)) until a point where the protons no longer have energy to liberate electrons above the Čerenkov energy threshold in equation (1). The angular distribution of emitted Čerenkov photons in water, including the contributions from electron scattering and Čerenkov emission from induced radioisotopes, is shown in figure 5(b).

GEANT4 simulations of Čerenkov radiation and fluorescence as an optical fibre is placed perpendicular to a 225 MeV proton beam are shown in figures 6(a) and (b) respectively. The results have been normalized to the number of Čerenkov and fluorescence photons emitted and guided through the optical fibre per proton.

3.6. Experimental irradiation of optical fibres with protons

The optical fibres were placed in a water phantom perpendicular to the beam direction (i.e. $\phi = \pi/2$ in figure 1(b)) and irradiated with 180 MeV protons in a 10 cm × 10 cm field consisting of 41 × 41 spots. The set-up is sketched in figure 7(a), where an optical fibre is placed in the centre of the field but does not extend to the edge. A signal is detected for each of the 41 horizontal scan lines, which results in the 41 peaks in figure 7(b). The four decreasing peaks to the right correspond to the case, in which the beam does not scan directly over the fibre, as illustrated in the upper part of figure 7(a).

The PMT, with a resolution on the micro-second scale, was able to resolve the delivery of each spot in the vicinity of the fibre as seen in the close-up in figure 7(b). The optical signal as a function of depth is calculated from the scan lines that passed directly over the fibre, i.e. the 37 peaks from left to right in figure 7(b). The response of the optical fibre irradiated with protons at a given depth is calculated in two ways: firstly, by averaging over an integration of each of the 37 peaks; and, secondly, by averaging over the signal amplitude of each of the 37 peaks. The results are compared in figure 8 to a reference curve obtained with a Bragg Peak ionization chamber normalized to the entrance value.

4. Discussion

4.1. Optical photons in electron beams

The PMT signal as a function of gantry angle in figure 2(a) indicates that Čerenkov radiation in the optical fibre might completely dominate fluorescence in electron beams if the irradiation angle is chosen properly. The coinciding spectra obtained in the 50 kVp x-ray source and with 20 MeV electrons ($\phi = 135°$) in figure 2(b) confirm that the Čerenkov radiation is indeed emitted outside the acceptance cone at such an angle. The fluorescence spectrum is in agreement with results published in De Boer *et al* (1993). Hence, the spectrum obtained in the 20 MeV electron linac at $\phi = 45°$ is the result of a Čerenkov spectrum convolved with the transmission profile of the optical fibre where no photons below 350 nm are transmitted in PMMA.

For simplicity, the spectra are scaled to their respective maximum value but the electron spectra were acquired with the same dose-rates and the same length of irradiated fibre; the actual intensity of the Čerenkov spectrum ($\phi = 45°$) is of the order of 15 times more intense than the fluorescence spectrum obtained at $\phi = 135°$, and thus indeed confirms the presence of Čerenkov radiation.

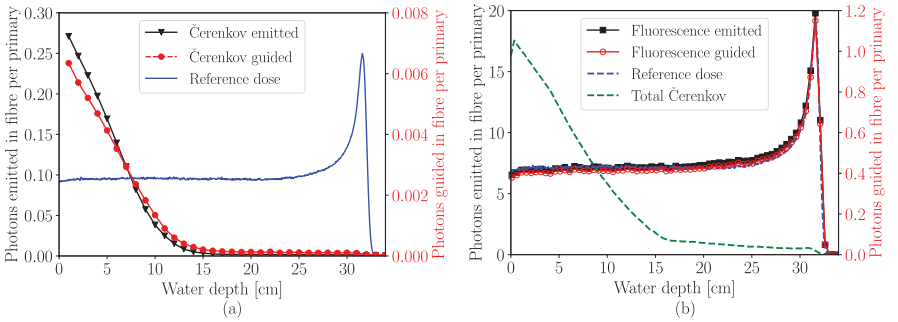

Figure 6. GEANT4 simulations of 225 MeV protons in water. (a) Number of Čerenkov photons emitted and guided in the optical fibre per proton. (b) Number of (isotropically) emitted fluorescence emissions per proton emitted and guided in the optical fibre.

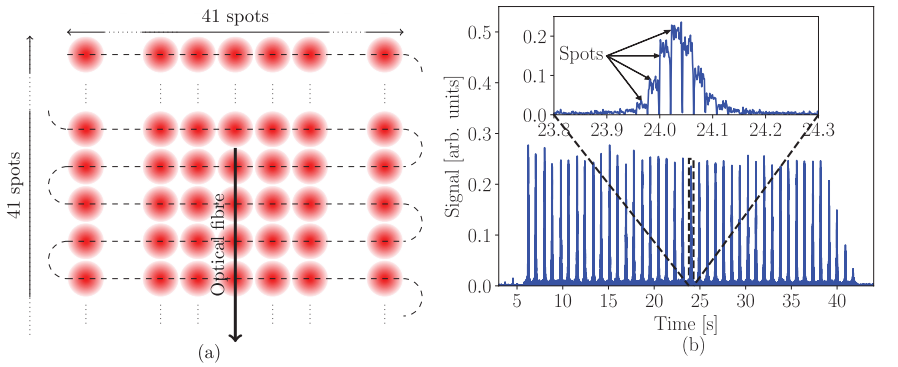

Figure 7. Optical fibre placed orthogonal to the 180 MeV proton beam direction in a water phantom. (a) The scanning pattern with the optical fibre placed in the middle of the field. (b) The signal as the beam scans by the optical fibre in (a) 41 times at 6 cm depth. The close-up shows the deposition of single spots. The signal increases, as the beam approaches the fibre, and subsequently decreases as the beam passed by.

4.1.1. Monte Carlo validation

The effective signal estimated from the fibre-subtraction method for $\phi = 45°$ is dominated by Čerenkov radiation as shown in figures 2(a) and (b). However, according to figure 3(c), the Čerenkov emittance per electron is diminished with almost two orders of magnitude at half the range relative to the entrance for such an angle between fibre and beam. Hence, if the Čerenkov radiation from 20 MeV electrons were to be measured as a function of water depth with an optical fibre placed an angle $\phi \sim 45°$, the Čerenkov signal would be expected to be negligible after ~ 8 cm.

The results in figure 4 show good agreement for both 12 MeV and 20 MeV electrons between calculations with the GEANT4 model of the fibres in the water phantom and experimentally measured in the medical linac. The agreements in this critical test validate the Monte Carlo implementation of the fibres and the simulation of emission and transmission of Čerenkov radiation. The Monte Carlo implementation of the optical fibres is henceforth used to investigate Čerenkov radiation in a proton beam in detail which otherwise would not have been feasible.

4.2. Protons

4.2.1. Čerenkov radiation

The GEANT4 simulations of Čerenkov radiation emission in a 225 MeV proton beam in water are shown in figures 5(a) and (b). The overall emission of Čerenkov photons becomes more isotropic as the protons slow down and Čerenkov emission following isotropic decays starts to be significant, which in turn makes it challenging to measure the Čerenkov photons with e.g. an optical fibre. Although the secondary electrons above the Čerenkov radiation energy threshold are liberated in a primarily forward direction, the combination of an energy-dependent Čerenkov radiation emission direction and particle scattering yield a broad angular Čerenkov distribution. The angular distribution of emitted Čerenkov photons nonetheless indicates that it may

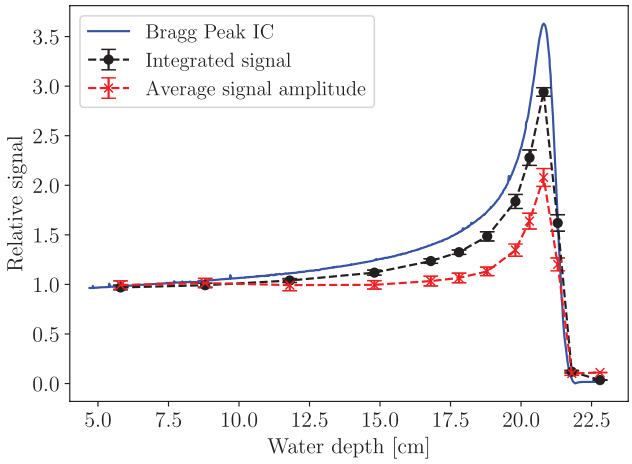

Figure 8. The integrated signal over all depth measurements resembles the reference depth-dose curve obtained with an ionization chamber.

be advantageous to place the optical fibre at an $\approx 30°$ angle relative to the beam direction, to guide as much Čerenkov radiation as possible through the fibre.

4.2.2. Transition radiation

It should be noted that transition radiation (Ginzburg and Frank 1946) also gives rise to optical photons in the fibre due to differing optical properties (Jelley 1958). However, as the intensity of transition radiation is proportional to $\gamma = 1/\sqrt{1-\beta^2}$, the transition radiation in an optical fibre is negligible relative to fluorescence for proton beams at clinical energies, and generally not emitted within the acceptance angle of the fibre (when placed perpendicular to the beam), as the radiation peaks at an angle γ^{-1} relative to the particle's path (Dolgoshein 1993).

4.2.3. Fluorescence and Čerenkov radiation in optical fibres

The simulations in figure 6(a), using the Monte Carlo implementation of the emission and transmission of Čerenkov radiation validated in an electron linac, indicate the problems related to measurements of Čerenkov radiation in proton beams. Although just fewer than one Čerenkov photon per proton is emitted in a fibre placed at the entrance, only a fraction of these photons are emitted within the acceptance angle of the optical fibre. The simulation does not take the attenuation of the optical fibre into account, and consequently serves as an ideal case.

The number of fluorescence photons emitted in the fibre along with the number of fluorescence photons within the acceptance angle of the fibre per proton is shown in figure 6(b). The fluorescence distribution exhibits, due to its isotropic nature, the same depth dependence as deposited energy; the ionization quenching is not included in the simulations, as the abovementioned results in Jang *et al* (2012) indicate that quenching is negligible in the PMMA-based fibre. A comparison between the figures 6(a) and (b) gives, that the number of fluorescence photons within the acceptance angle of the optical fibre per proton is more than an order of magnitude larger than that of Čerenkov radiation. In the case of a 225 MeV proton beam, Čerenkov radiation is completely negligible after ~ 14 cm. Hence, the optical photon signal measured with a fibre placed perpendicular to a proton beam is largely dominated by fluorescence photons.

These results, based on Monte Carlo implementation of the fibres validated in known Čerenkov radiation regimes, do not support either of the hypotheses that (i) the optical signal under proton irradiation is solely Čerenkov radiation, as in Jang *et al* (2012), or (ii) Čerenkov radiation is able to *contaminate* the fluorescence signal substantially after 14 cm water depth (see figure 6(a)) in a 225 MeV proton beam as described in Darafsheh *et al* (2016).

4.2.4. Experimental results for protons

Generally, it was possible to distinguish between the 8 and 9 spots closest to the fibre in each scan line, as seen in figure 7(b). As one may infer from the close-up in figure 7(b), the FWHM of the signal in a scan line is about four spots, which corresponds to FWHM $\simeq 1$ cm at 6 cm water depth with the given number of spots and field

size. The actual FWHM = 9.4 mm for the beam at the entrance region for the same energy indicates that optical fibres may be used to monitor both the spot size and delivery time—which, however, is out of the scope of this work.

The measured Bragg peak in figure 8 is the result of fluorescence, as measured with the monochromator during irradiation with photons below the Čerenkov energy threshold in figure 2, and simulated in figure 6(b). The signal reduction at the Bragg peak was anticipated due to spread of the beam spots with increasing water depth and the 1 mm diameter of the fibre. The interpretation of fluorescence is in agreement with other sources (Peeples *et al* 2012, Yamamoto *et al* 2018) reporting a strong correlation between luminescence and dose profile as water is irradiated with photons or protons below the Čerenkov threshold.

4.3. Ionization quenching

The apparently quenching-free curve resulting from a PMMA-based optical fibre irradiated with protons (Jang *et al* 2012) may give information about the nature of ionization quenching. In order to understand the quenching-free results, we present two hypotheses, based on differences between the optical fibre and traditional organic scintillators.

The emission of light from PMMA-based materials is different from that from polystyrene-based scintillators. Acetone, a ketone which is spectroscopically similar to the ester in PMMA, has a singlet–singlet transition about three orders of magnitude stronger than its triplet–singlet transition (Becker *et al* 1983). Thus, we suggest a possible explanation of the lack of quenching could be the dominating singlet–singlet transition in the optical fibre, although the presence of e.g. O_2 in the fibre core inevitably leads to triplet–singlet transitions.

Another approach to understanding of the quenching-free results is to consider the number of excited molecules involved in the quenching process. Blanc *et al* (1962) developed a general equation to describe the kinetics of the excitation densities, where Birks' formula is a solution to a simplified version of their equation (Birks 1964). The quenching in this formulation consists of terms in which the density of excited molecules is of power 2 or higher, and thus extremely density-dependent. The low local concentration of excited molecules in PMMA, compared to excitation concentrations in typical scintillator-based materials, consequently results in a much lower (if not negligible) ionization quenching in the optical fibre, compared to organic scintillators.

5. Conclusions

The Čerenkov radiation and fluorescence emitted in optical fibres exposed to electron beams was used to establish a foundation, where a Monte Carlo implementation of the emission and transmission of optical photons was validated against experimental data. The simulations of emittance and guidance of optical photons in fibres irradiated with protons indicate that fluorescence—and not Čerenkov radiation—is responsible for the optical Bragg peak measured in a 180 MeV proton beam, where the signal reduction relative to the reference dose curve in this work is due to the small spot size relative to the fibre diameter.

The validated model does not support either of the hypotheses that the optical signal in a fibre under proton irradiations is (i) entirely Čerenkov radiation (Jang *et al* 2012) or (ii) severely Čerenkov contaminated (Darafsheh *et al* 2016)—since neither follows the depth distribution nor spatial extension of Čerenkov distribution, and the amount of fluorescence, furthermore, greatly exceeds that of Čerenkov radiation.

The mechanism behind the quenching-free fluorescence signal in optical fibres during proton irradiation still requires further scrutiny.

Acknowledgments

The work was supported by the Danish Cancer Society. The authors thank Lars René Lindvold, Technical University of Denmark, for stimulating discussions pertaining to luminescence properties and Čerenkov radiation effects in optical fibres.

ORCID iDs

Jeppe Brage Christensen https://orcid.org/0000-0002-6894-381X

References

Agostinelli S *et al* 2003 GEANT4—a simulation toolkit *Nucl. Instrum. Methods* A **506** 250–303

Andersen C E, Bøtter-Jensen L and Murray A S 2003 A mini x-ray generator as an alternative to a $^{90}Sr/^{90}Y$ beta source in luminescence dating *Radiat. Meas.* **37** 557–61

Archambault L, Beddar A S, Gingras L, Roy R and Beaulieu L 2006 Measurement accuracy and Cerenkov removal for high performance, high spatial resolution scintillation dosimetry *Med. Phys.* **33** 128–35
Becker H G O, Böttcher H, Dietz F, Rehorek D, Roewer G, Schiller K and Timpe H J 1983 *Einführung in die Photochemie* (New York: Georg Thieme Verlag Stuttgart)
Beddar A S, Mackie T R and Attix F H 1992a Cerenkov light generated in optical fibres and other light pipes irradiated by electron beams *Phys. Med. Biol.* **37** 925–35
Beddar A S, Mackie T R and Attix F H 1992b Water-equivalent plastic scintillation detectors for high-energy beam dosimetry: I. Physical characteristics and theoretical considerations *Phys. Med. Biol.* **37** 1883–900
Beddar A S, Mackie T R and Attix F H 1992c Water-equivalent plastic scintillation detectors for high-energy beam dosimetry: II. Properties and measurements *Phys. Med. Biol.* **37** 1901–13
Beddar S and Beaulieu L 2016 *Scintillation Dosimetry* (Boca Raton, FL: CRC Press)
Beierholm A R, Behrens C F and Andersen C E 2014 Dosimetric characterization of the Exradin W1 plastic scintillator detector through comparison with an in-house developed scintillator system *Radiat. Meas.* **69** 50–6
Birks J B 1951 Scintillations from organic crystals: specific fluorescence and relative response to different radiations *Proc. Phys. Soc.* A **64** 874–77
Birks J B 1964 *The Theory and Practice of Scintillation Counting: International Series of Monographs in Electronics and Instrumentation* vol 27 (Amsterdam: Elsevier)
Blanc D, Cambou F and de Lafond Y G 1962 Kinetics of the fast component of scintillation in a pure organic medium. Application to anthracene *C. R. Acad. Sci.* **18** 3187–89
Boivin J, Beddar S, Bonde C, Schmidt D, Culberson W, Guillemette M and Beaulieu L 2016 A systematic characterization of the low-energy photon response of plastic scintillation detectors *Phys. Med. Biol.* **61** 5569–86
Buranurak S, Andersen C E, Beierholm A R and Lindvold L R 2013 Temperature variations as a source of uncertainty in medical fiber-coupled organic plastic scintillator dosimetry *Radiat. Meas.* **56** 307–11
Čerenkov P A 1937 Visible radiation produced by electrons moving in a medium with velocities exceeding that of light *Phys. Rev.* **52** 378–79
Darafsheh A, Taleei R, Kassaee A and Finlay J C 2016 The visible signal responsible for proton therapy dosimetry using bare optical fibers is not Čerenkov radiation *Med. Phys.* **43** 5973–80
De Boer S F, Beddar A S and Rawlinson J A 1993 Optical filtering and spectral measurements of radiation-induced light in plastic scintillation dosimetry *Phys. Med. Biol.* **38** 945–58
Demers J L, Davis S C, Zhang R, Gladstone D J and Pogue B W 2013 Čerenkov excited fluorescence tomography using external beam radiation *Opt. Lett.* **38** 1364–6
Dolgoshein B 1993 Transition radiation detectors *Nucl. Instrum. Methods* A **326** 434–69
Frank I and Tamm I 1937 Coherent visible radiation from fast electrons passing through matter *Acad. Sci. USSR* **14** 109–14
Ginzburg V and Frank I 1946 To the theory of transition radiation *Sov. Phys.* **16** 15
Glaser A K, Davis S C, Voigt W H, Zhang R, Pogue B W and Gladstone D J 2013 Projection imaging of photon beams using Čerenkov-excited fluorescence *Phys. Med. Biol.* **58** 601–19
Glaser A K, Zhang R, Gladstone D J and Pogue B W 2014 Optical dosimetry of radiotherapy beams using Čerenkov radiation: the relationship between light emission and dose *Phys. Med. Biol.* **59** 3789–811
Helo Y, Kacperek A, Rosenberg I, Royle G and Gibson A P 2014a The physics of Čerenkov light production during proton therapy *Phys. Med. Biol.* **59** 7107–23
Helo Y, Rosenberg I, DSouza D, MacDonald L, Speller R, Royle G and Gibson A P 2014b Imaging Čerenkov emission as a quality assurance tool in electron radiotherapy *Phys. Med. Biol.* **59** 1963–78
Jang K W, Yoo W J, Shin S H, Shin D and Lee B 2012 Fiber-optic Čerenkov radiation sensor for proton therapy dosimetry *Opt. Express* **20** 13907–14
Jarvis L A, Zhang R, Gladstone D J, Jiang S, Hitchcock W, Friedman O D, Glaser A K, Jermyn M and Pogue B W 2014 Cerenkov video imaging allows for the first visualization of radiation therapy in real time *Int. J. Radiat. Oncol. Biol. Phys.* **89** 61522
Jelley J V 1958 *Čerenkov Radiation and its Applications* (Oxford: Pergamon)
Lin H, Zhang R, Gunn J R, Esipova T V, Vinogradov S, Gladstone D J, Jarvis L A and Pogue B W 2016 Comparison of Cherenkov excited fluorescence and phosphorescence molecular sensing from tissue with external beam irradiation *Phys. Med. Biol.* **61** 3955–68
Marckmann C J, Aznar M C, Andersen C E and Bøtter-Jensen L 2006 Influence of the stem effect on radioluminescence signals from optical fibre Al2O3: C dosemeters *Radiat. Prot. Dosim.* **119** 363–67
Peeples J L, Stokely M H, Poorman M C, Magerl M and Wieland B W 2012 Visual observation of boiling in high power liquid target *AIP Conf. Proc.* **1509** 76–80
Therriault-Proulx F, Beaulieu L, Archambault L and Beddar S 2013 On the nature of the light produced within PMMA optical light guides in scintillation fiber-optic dosimetry *Phys. Med. Biol.* **58** 2073–84
Therriault-Proulx F, Beddar S, Briere T M, Archambault L and Beaulieu L 2011 Removing the stem effect when performing Ir-192 HDR brachytherapy *in vivo* dosimetry using plastic scintillation detectors: a relevant and necessary step *Med. Phys.* **38** 2176–79
Wootton L and Beddar S 2013 Temperature dependence of BCF plastic scintillation detectors *Phys. Med. Biol.* **58** 2955–67
Yamamoto S, Koyama S, Yabe T, Komori M, Tada J, Ito S, Toshito T, Hirata Y and Watanabe K 2018 Stability and linearity of luminescence imaging of water during irradiation of proton-beams and x-ray photons lower energy than the Cerenkov light threshold *Nucl. Instrum. Methods* A **803** 48–56

Paper II

Title:

Relating ionization quenching in organic plastic scintillators to basic material properties by modelling excitation density transport and amorphous track structure during proton irradiation

Authors:

Christensen JB and Andersen CE

Submitted to:

Physics in Medicine and Biology,
April 2018.

Status:

Published September 2018.

Digital Object Identifier:

10.1088/1361-6560/aadf2d

IOP Publishing Phys. Med. Biol. 63 (2018) 195010 (11pp) https://doi.org/10.1088/1361-6560/aadf2d

Physics in Medicine & Biology

IPEM Institute of Physics and Engineering in Medicine

PAPER

RECEIVED
25 April 2018

REVISED
3 August 2018

ACCEPTED FOR PUBLICATION
5 September 2018

PUBLISHED
28 September 2018

Relating ionization quenching in organic plastic scintillators to basic material properties by modelling excitation density transport and amorphous track structure during proton irradiation

Jeppe Brage Christensen and Claus E Andersen

Center for Nuclear Technologies, Technical University of Denmark, Frederiksborgvej 399, 4000 Roskilde, Denmark

E-mail: jepb@dtu.dk

Keywords: ionization quenching, organic scintillators, proton therapy, quenching kinetics, dosimetry

Abstract

Ionization quenching in organic scintillators is usually corrected with methods that require careful assessment of the response relative to that of an ionization chamber. Here, we present a framework to compute ionization quenching correction factors (QCFs) from first principles for organic plastic scintillators exposed to ions. The tool solves the kinetic Blanc equation, of which the Birks model is a simplified solution, based on amorphous track structures models. As a consequence, ionization quenching correction factors can be calculated relying only on standard, tabulated scintillator material properties such as the density, light yield, and decay time.

The tool is validated against experimentally obtained QCFs for two different organic plastic scintillators irradiated with protons with linear energy transfers (LETs) between 5–70 MeV cm^{-1}. The QCFs computed from amorphous track structure models and the BC-400 scintillator properties deviate less than 3% from the Birks model for LETs below 45 MeV cm^{-1} and less than 5% for higher LETs. The agreement between experiments and the software for the BCF-12 scintillator is within 2% for LETs below 45 MeV cm^{-1} and within 10% for LETs above, comparable to the experimental uncertainties. The framework is compiled into the open source software `ExcitonQuenching` available for download. `ExcitonQuenching` enables computations of QCFs in organic plastic scintillators exposed to ions independently of experimentally based quenching parameters in contrast to the Birks model. `ExcitonQuenching` can improve the accuracy of correction factors and understanding of ionization quenching in scintillator dosimetry.

1. Introduction

Organic plastic scintillators are attractive for particle dosimetry due to the prompt response, small size, and good water-equivalence (Beddar *et al* 1992a, 1992b). Fibre-coupled scintillators are known to exhibit a stem-effect, where light is emitted outside the primary scintillating mechanism (Archambault *et al* 2005, Therriault-Proulx *et al* 2011), as well as a temperature dependence (Buranurak *et al* 2013, Wootton and Beddar 2013). These mechanisms are however well-understood and the effects can be corrected for. The situation for organic scintillators exposed to radiation with high linear energy transfer (LET) is more complex, and the reduced scintillator response, due to high local ionization densities, is termed ionization quenching. The quenching is traditionally explained as a reduction of the primary scintillation efficiency, where zones with a high ionization density fail to transfer all energy to the excited states (Birks 1951). Kallmann and Brucker (1957) showed that most quenching occurs faster than the characteristic decay time of the scintillator, which may be explained in terms migration of excited states, heat conduction, and ionic recombination (Birks 1964, Beddar and Beaulieu 2016). The quenching is often corrected by comparing the response of the quenched signal in an organic scintillator to the unquenched signal measured with an ionization chamber. On the other hand, Alsanea *et al* (2018) exploited the quenching differences in four organic scintillators to simultaneously measure the LET and dose in therapeutic proton beams. Monte Carlo simulations of the LET distribution enable quenching corrections by applying the

semi-empirical formula developed by Birks (1951), henceforth referred to as the Birks model. Nonetheless, such quenching corrections often give rise to deviations up to 10% at the Bragg peak due to the sharp LET-gradient (Beddar and Beaulieu 2016).

Recently, Boivin *et al* (2016) showed how the Birks model breaks down for high-LET photon beams, whereas a shortcoming for ions has been known for decades; two ions with same LET but different atomic number will in the Birks model give rise to the same ionization quenching. Such a prediction however contradicts experiments (Newman and Steigert 1960, Birks 1964) as the radial energy deposition by secondary electrons (EDSE) differs in the two cases. In any case, it motivates new approaches and the application of track structure models to account for the energy deposition by secondary electrons.

Blanc *et al* (1962, 1964) developed a kinetic model where the energy of excited molecules is migrating radially and lost by fluorescence and quenching. The Blanc model depends on—like the Birks model and most EDSE models—the number of molecules involved in the quenching process. In this work, we focus on computing the ionization quenching for organic plastic scintillators based on the Blanc model. The Birks model itself takes on the form of a simplified version of the Blanc model (Birks (1964), p 198). As such, the Blanc formalism enables a more exact computation of the quenching correction factors than the Birks model and, furthermore, is independent of experimentally determined quenching parameters as the Birks *kB* factor.

Here, we use amorphous track structure theory to model the radial energy deposition after an ion has penetrated an organic plastic scintillator. Amorphous track structure theory often distinguishes between the core and the penumbra. The core is an extremely narrow zone with an enormous density of energy deposited by the incident ion whereas the penumbral region, exhibiting a r^{-2} density decrease, is mainly due to energy deposition by secondary electrons. The kinetic Blanc model is subsequently applied to evolve the initial radial energy deposition in the temporal and spatial domains while keeping track of the fluorescence and quenching. The Blanc model as a consequence is able to distinguish the quenching between two particles, with the same LET but different atomic numbers, in contrast to the Birks model.

The first part of the present work outlines the concepts of quenching corrections factors and track structure models. Solutions to the Blanc model are subsequently investigated with its inherent free parameters. The Blanc model consists of a set of general parameters, which in this work are estimated by fitting the Blanc model to experimentally obtained quenching correction factors. These parameters are then examined by computing the ionization quenching in a different scintillator and subsequently comparing the theory to experimental results.

The numerical framework to apply track structure theory and solve the Blanc equation is compiled into the open source code `ExcitonQuenching` available for download[1]. `ExcitonQuenching` computes the quenching correction factors from first principles using merely the density, decay time, and light yield of an organic plastic scintillator and the energy of the primary particle.

2. Background

2.1. Ionization quenching

The scintillation light yield per unit length $\mathrm{d}S/\mathrm{d}x$ for an organic scintillator is traditionally written in the form

$$\frac{\mathrm{d}S}{\mathrm{d}x} = \frac{A \cdot \mathrm{LET}}{\mathrm{QCF}}, \qquad \mathrm{QCF} = 1 + kB \cdot \mathrm{LET} + C \cdot \mathrm{LET}^2 + \cdots, \tag{1}$$

where A is the scintillation efficiency, and the quenching correction factor (QCF) depends on the quenching parameters kB and C. The Birks model truncates the series at the first-order LET-term, which has been shown to be successfully applicable for quenching corrections (Beddar and Beaulieu 2016). The second-order LET term was suggested by Chou (1952) and is often neglected but has been shown to give a better correction for high-LET (Torrisi 2000).

2.2. Kinetics of excitation densities

Blanc *et al* (1962, 1964) proposed a kinetic model which considers a number of molecules excited to the first singlet state which are allowed to migrate, fluoresce, and quench. The excited states are henceforth referred to as excitons to comply with the terminology in Birks (1964). The Blanc model governs the kinetics of the excitation density $n(r, t)$, where r is the distance from the centre of the ion track and t is the time after the ionization. The model takes on the form of

$$\frac{\partial n}{\partial t} = D\nabla^2 n - (p + k)n - \alpha n^2 - \beta n^3, \tag{2}$$

where D is the exciton diffusion constant, and p, k, αn, and βn^2 are defined as the rates of fluorescence emission, and uni-, bi-, and trimolecular quenching, respectively. Unimolecular quenching is isolated to a single molecule,

[1] https://github.com/jbrage/ExcitonQuenching

whereas the importance of the bi- and tri-molecular quenching terms increases with the local exciton density, i.e. with increasing LET.

Consider two scintillators with the same density and decay time but different scintillation efficiencies being penetrated by two identical particles. The scintillator with the higher scintillation efficiency will thus have a larger local excitation density. As a consequence, the second- and third-order quenching terms will lead to more quenching than in the scintillator with a lower scintillation efficiency. Similarly, two scintillators with the same scintillation efficiency and density—but different decay times—will require different quenching correction factors: Although the local exciton densities immediately after the particle passed are equal, the scintillator with the faster decay time is more efficient in emitting photons before they are quenched than the other. The diffusion term, on the other hand, causes the excitons to migrate away from the center of the particle track and hence decreases the quenching but not the rate of fluorescence emission. The Blanc model is an interesting ionization quenching model for several reasons:

1. The Blanc model corresponds to the Birks model if only fluorescence and unimolecular quenching are included (Birks 1964, p 198; Blanc *et al* 1962), i.e. truncating equation (1) at the first-order LET term. If fluorescence, uni-, and bimolecular quenching terms are included in the Blanc model, it is equivalent to the model proposed by Chou (1952), i.e. with both kB and C as quenching parameters in equation (1) (Birks (1964), p 198).
2. The Blanc model enables an inclusion of amorphous track structure theory, and—in contrast to the semi-empirical Birks and Chou models—two ions with same LET and different charges will hence give rise to different quenching correction factors as experimentally observed.
3. The solution of equation (2) makes it feasible to examine the temporal structure of the ionization quenching.

The version of the Blanc equation in equation (2) only models the exciton interactions between the first singlet state and the ground state. An extension to the equation, including the interactions with the first triplet state, could be added with a second coupled partial differential equation as suggested by Blanc *et al* (1962). The extended model can be validated against experimentally obtained QCFs for an appropriate scintillator (e.g. BCF-60, Saint-Gobain, France, as measured by Hoehr *et al* (2018)). Nonetheless, such a study is beyond the scope of this work.

2.3. Amorphous track structure models

The radial excitation density distribution in an ion track should vary according to the material and the energy of the primary particle and this can be achieved through amorphous track structure models. Amorphous track structures consider the radial energy distribution as the average of many secondaries and tracks, i.e. a continuous function, in contrast to the microdosimetric approach, where the stochastic nature of energy deposition by single electrons is taken into account. The initial number of excitations per unit length N_0 depends on the scintillation efficiency A, the number of photons emitted per deposited energy, as

$$N_0 = A \cdot \mathrm{LET}. \tag{3}$$

The ionization quenching is investigated using three different radial energy deposition distributions, namely the Gaussian (Blanc *et al* (1964)), Chatterjee and Schaefer (1976), and Scholz and Kraft (1996) track structure models. The three track structure models are defined in appendix A and shown in figure 1 for two different energies.

The track structure models have been chosen to reflect the cases of (i) an extremely dense core (Chatterjee–Schaefer), (ii) the continuous transition from core to penumbra (Scholz–Kraft), and (iii) the Gaussian which is independent of the range of secondary electrons but has been applied historically due to its simplicity. Other track structure models, such as those by Hansen and Olsen (1984), Kiefer and Straaten (1986) and Katz and Varma (1991), could have been included as well with similar arguments.

The distribution of exciton densities using amorphous track structure models, and exciton interaction probabilities in terms of the Blanc model, makes it feasible to investigate ionization quenching at the macroscopic scale.

3. Methods

3.1. Experimentally determined quenching correction factors

Often the LET-varying QCF is estimated by comparing the quenched scintillator measurement to an unquenched measurement with an ionization chamber. Two such examples are shown in figure 2 where Wang *et al* (2012) irradiated an organic fibre-coupled scintillator (BCF-12, Saint-Gobain, France) and Torrisi (2000) irradiated a thin organic scintillator (BC-400, Bicron, USA) with protons at different energies.

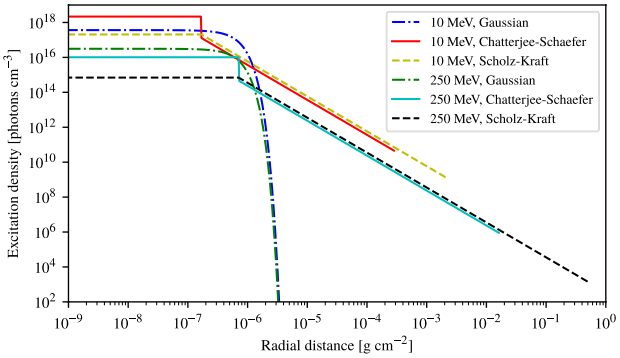

Figure 1. The three track structure models in equations (A.1)–(A.4) for protons at 10 MeV and 250 MeV in water. The range of the secondary electrons depends on the kinetic energy of the primary particle, which is included in the Scholz–Kraft and Chatterjee–Schaefer track structures, but unaccounted for in the Gaussian model.

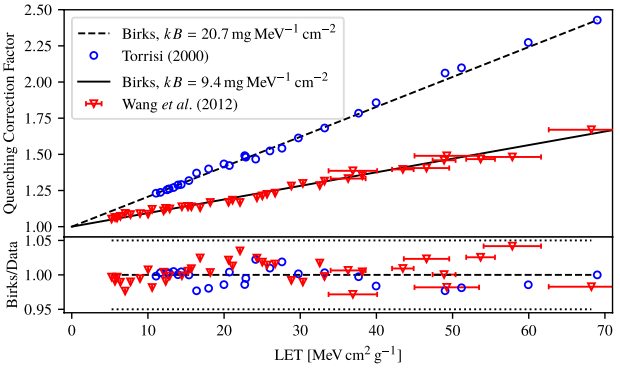

Figure 2. The quenching correction factor as a function of LET for two different organic scintillators irradiated with protons where the Birks model is fitted to the data in both cases. The ratios of the QCF obtained from the Birks model to the experimentally obtained values in the figure below indicate a good agreement for both measurements.

Wang *et al* (2012) and Torrisi (2000) fitted the Birks model to the QCF as a function of LET which in both cases show an agreement within 5%. Since the QCFs in both data sets are given for a wide LET range and differ by more than a factor of 2, they serve as a reference and are applicable to validate the QCFs calculated with the Blanc model. The parameters relevant for the Blanc model are listed in table 1 for the BC-400 and BCF-12 plastic scintillators.

3.2. Numerical scheme

3.2.1. The itinerary to quenching correction factors

The Blanc model is used to compute the QCF for a particle with energy E as outlined in figure 3. The scintillator efficiency A defines, along with the LET, the total number of excitons N_0 involved in the quenching process as given by equation (3). The N_0 excitons are distributed radially according to an amorphous track structure model, where the penumbra and core radii are computed from the particle energy E and the density ρ of the scintillating material as given in appendix A. The chosen track structure model governs in any case the radial exciton distribution at time $t = 0$.

The excitons are subsequently evolved in the temporal and spatial domain as governed by the Blanc model in equation (2). The total emission of fluorescence photons, the signal, is computed by integrating over the fluorescence term pn in equation (2) from time $t = 0$ to $t = \infty$. The numerical scheme used to solve the partial differential equation (2) is included in appendix B.

The QCF is computed by solving equation (2) twice as outlined in figure 3 part (b); with and without the ionization quenching parameters. Setting the parameters $\alpha = \beta = 0$ in equation (2) leads to a solution of the form $n(t) \propto \exp(-t/\tau)$, i.e. the fluorescence signal follows an exponential decay with time constant τ

Table 1. The scintillator parameters required to model the exciton densities and fluorescence emission are tabulated for most scintillators. The relevant parameters for the two scintillators in the present work are given below. Data from the manufacturer (Saint-Gobain, Paris, France).

Scintillator	Scintillation efficiency, A [photons MeV^{-1}]	Decay time τ [ns]	Density ρ [g cm^{-3}]
BCF-12	8000	3.2	1.05
BC-400	11 300	2.4	1.03

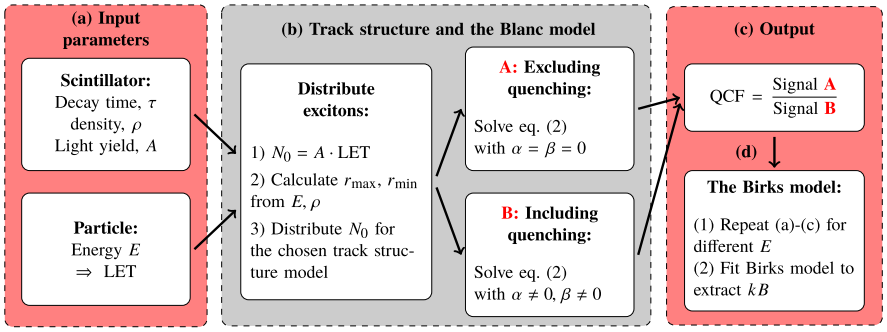

Figure 3. The workflow to a quenching correction factor. (a) The input parameters are responsible for the number of excitons involved in the quenching process. (b) The initial exciton distribution is modelled by the selected track structure model. The Blanc model in equation (2) is subsequently used to calculate the emission of fluorescence in two cases: With and without ionization quenching. (c) The QCF is as a result computed as the ratio of the unquenched to the quenched signal. (d) The Birks model parameter kB can be calculated from a fit to a series of the QCFs as a function of LET.

without ionization quenching. The solution to equation (2) with $\alpha \neq 0, \beta \neq 0$, and thus including ionization quenching, reduces in any case the total signal. The QCF is accordingly computed as the ratio of the two signals. The steps (a)–(c) may be repeated for several particle energies to plot the QCF as a function of LET. The Birks quenching parameter kB can consequently be extracted theoretically by fitting the Birks model to these computed data.

3.3. Quenching parameters in the Blanc model

The data by Wang *et al* (2012) in figure 2 comprises the QCFs for protons penetrating the BCF-12 scintillator over a wide range of LETs, which can be used to determine the general (D, α, β) parameters in the Blanc model, equation (2). The QCF for a particular plastic scintillator and particle in the Blanc formulation merely depends on the input parameters listed in figure 3(a). The scintillator decay time $\tau = (p + k)^{-1}$ is tabulated for most plastic scintillators, where the probability rates for the fluorescence emission p and unimolecular quenching k are weighted equally. Any weight cancels out as the QCF, figure 3(c), is computed as the ratio between the signals.

Let a proton with a given LET penetrate a thin BCF-12 layer where the excited states are radially distributed as in the, say, Scholz–Kraft model. The modified Blanc model in equation (2) will then for one set of (D, α, β) parameters give rise to some QCF using the workflow outlined in figure 3. This calculation is repeated for all LET values present in the data set by Wang *et al* (2012). The quality of the particular set of (D, α, β) parameters is evaluated through the sum of squares

$$\chi^2 = \sum_i \frac{\left(\mathrm{QCF}_{\mathrm{Blanc},i} - \mathrm{QCF}_{\mathrm{exp},i}\right)^2}{\mathrm{QCF}_{\mathrm{exp},i}}, \qquad \forall i \in [\text{LET values in figure 2}] \tag{4}$$

where $\mathrm{QCF}_{\mathrm{Blanc},i}$ is the QCF computed with the Blanc model for the ith LET-value in the Wang *et al* (2012) data, and $\mathrm{QCF}_{\mathrm{exp},i}$ is the corresponding QCF obtained experimentally. The best set of (D, α, β) parameters is found by minimizing χ^2.

The exciton diffusivity has been experimentally estimated to be of the order of $D \simeq 5 \times 10^{-4}$ cm^2 s^{-1}. The bimolecular quenching parameter is computed to be $\alpha \simeq 3.2 \times 10^{-9}$ cm^3 s^{-1} (Birks (1964), p 199), whereas the order of the trimolecular quenching parameter is to be determined. The uncertainties on the experimentally obtained values of D and α are unknown and they merely serve as means to compare to the computed χ^2 minima.

After the unique (D, α, β) parameters in the Blanc model have been established, the same parameters are used to compute the QCFs for protons interaction with the BC-400 scintillator and assessed against the corresponding experimental data by Torrisi (2000).

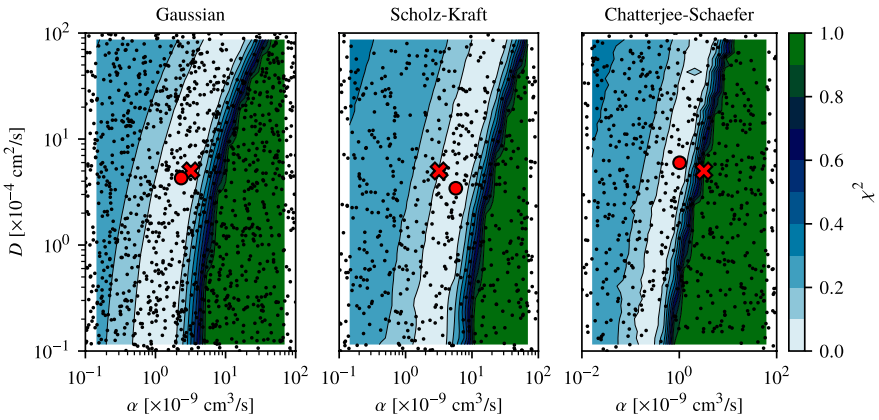

Figure 4. Maps over χ^2 from equation (4) for various values of (α, D) for the three track structure models. Each dot represents a pair of (α, D) drawn from a uniform distribution. Only a fraction of the samples are shown. The literature value is marked with a cross in each case, whereas the (α, D) sets providing the best match to the experimental QCFs are marked with a closed circle and listed in table 2.

4. Results

4.1. Quenching parameters

4.1.1. The second-order Blanc equation

The roles of the diffusion constant D and the bimolecular quenching parameter α in the Blanc model are investigated by truncating equation (2) after the second-order term, i.e. setting $\beta = 0$. χ^2 is in figure 4 mapped for various (α, D) pairs for the three track structure models in question. The (α, D) pairs are sampled uniformly and the χ^2 minimum is found by cubic interpolation. The experimentally determined D and calculated α values, listed in table 2, are marked with a cross in each χ^2 map for comparison.

4.1.2. The third-order Blanc equation

The inclusion of the third-order β term in equation (2) provides information about the local excitation density as trimolecular quenching requires a high-LET to occur. Adding higher-order terms in the Blanc model corresponds to extending the equation (1) with additional terms, i.e. corresponding to the Birks model to the Chou model and so on. The diffusion constant D is now fixed at the value obtained from minimizing χ^2 in figure 4, see table 2, to compare the magnitudes of the bi- and trimolecular quenching terms to each other for protons. The χ^2 maps for the Gaussian, Scholz–Kraft, and Chatterjee–Schaefer track structures are given in figure 5. The pairs of (α, β) providing the best fit to the experimental data is given in table 2 and marked with a filled circle in figure 5. Henceforth, the three parameters D, α, and β as given in table 2 are used to compute the QCF for a given plastic scintillator.

4.2. Quenching correction factors

The measurements by Wang *et al* (2012) of the quenched signal from the BCF-12 scintillator during proton irradiations are shown in figure 6, where the Birks model has been fitted to the data. The quenched response for the BCF-12 calculated with the Blanc model and the parameters in table 2 are shown alongside for each track structure model.

The quenched signal from the BC-400 scintillator irradiated with protons at different energies is for comparison plotted in the same figure. The Birks model is again fitted to the experimental data, whereas the quenched signal is computed independently of the data using the Blanc model and its parameters in table 2 and the BC-400 properties in table 1.

5. Discussion

5.1. Quenching in the Blanc model

5.1.1. Second-order Blanc equation, $\beta = 0$

The χ^2 maps for the three track structure models in figure 4 indicate a distinct correlation between α and D, which also is evident from Birks (1964, p 199), where α after several approximations is shown to be proportional

Table 2. The general parameters in the Blanc model providing the best fit to the experimental data: (i) when equation (2) was truncated at the second-order term ($\beta = 0$) and (ii) including the third-order term ($\beta \neq 0$). The D value obtained from the χ^2 mapping in the second-order case (figure 4) was used in the third-order case (figure 5) as well.

	2nd order		3rd order	
Method	D [cm^2 s^{-1}]	α [cm^3 s^{-1}]	α [cm^3 s^{-1}]	β [cm^6 s^{-1}]
Literature	5×10^{-4}[a]	3.2×10^{-9}[b]	—	—
Gaussian	4.3×10^{-4}	2.3×10^{-9}	1.3×10^{-9}	9.1×10^{-27}
Scholz–Kraft	4.2×10^{-4}	5.7×10^{-9}	4.5×10^{-9}	2.7×10^{-27}
Chatterjee–Schaefer	5.9×10^{-4}	1.0×10^{-9}	6.1×10^{-10}	4.2×10^{-28}

[a] From Kallmann and Brucker (1957).

[b] Calculated from Birks (1964), *Kinetics of Quenching*, p 199.

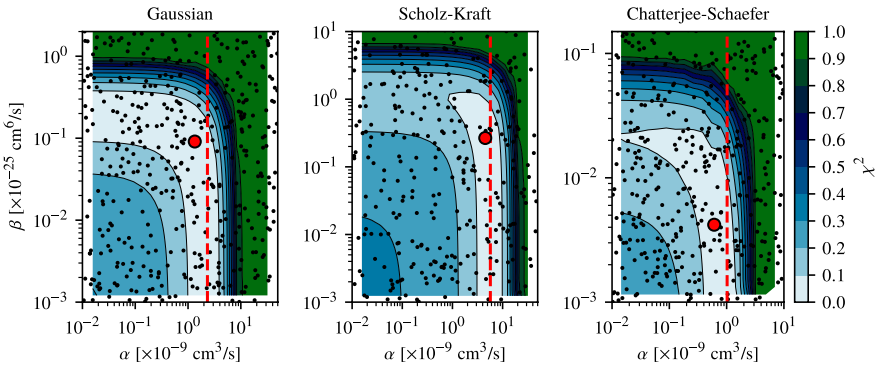

Figure 5. χ^2 maps when the parameter D is kept at the value given in table 2 and the quenching parameters α and β vary. Only a fraction of the samples are shown for simplicity. The dashed line corresponds to the α value obtained from figure 4, i.e. for $\beta \to 0$. The (α, β) values at the χ^2 minima are marked with a filled circle and listed in table 2.

to D. The mutual dependency indicates the primary role of the exciton diffusion constant: Due to the cylindrical symmetry of track structure models, the diffusion term $D\nabla^2 n$ effectively gives rise to exciton migration away from the center of the track. This in turns diminishes the bimolecular quenching rapidly as it is proportional to the square of the exciton density. Consequently, the quenching parameter α needs to increase if D increases to give rise to the same amount of quenching.

5.1.2. *Third-order Blanc equation, $\beta = 0$*

The χ^2 maps in figure 5 show the density dependence of the bi- and trimolecular quenching parameters α and β. As $\beta \to 0$, the α value providing the best match to the data converges towards the α value from figure 4 marked with a dashed line. The β value equivalently converges for $\alpha \to 0$, as anticipated, although such a value is not of interest.

Nonetheless, all three χ^2 maps contain a ridge, where both the α and β terms contribute to the ionization quenching, which indicates that an extra term—as in the Chou model relative to the Birks model—may be relevant for high-LET situations. The pair of (α, β) providing the best fit to the experimentally determined QCFs, the minimum χ^2 value, is for the Gaussian and Scholz–Kraft track structure found around the χ^2 ridge. The χ^2 minima are overall in the proximity to $\beta \to 0$ indicating that the β term is close to be negligible for proton relevant LETs.

The β term is only relevant for high-LET cases and these are often associated with large uncertainties for protons, as in the present case, which makes an unambiguous conclusion on its importance for protons difficult. As such, the small effect of an extra quenching parameter is in line with the literature: Birks (1964, p 194) investigated the extra parameter in the Chou model relative to the Birks model and concluded it redundant for the case of anthracene exposed to protons and α-particles. Torrisi (2000), on the other hand, concluded that the Chou model provides a better fit to the data for the BC-400 scintillator during proton irradiations than the Birks model does. The β term, or even additional terms of higher order, may be subject to a later investigation for particles with substantially higher LET than protons.

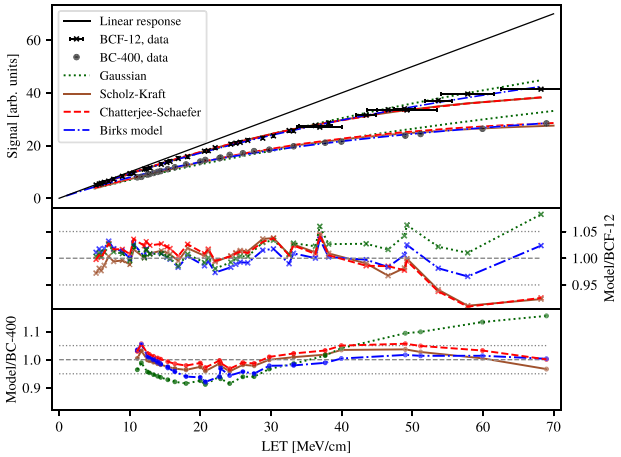

Figure 6. The quenched signals of the BCF-12 (Wang *et al* 2012) and BC-400 (Torrisi 2000) scintillators are plotted with crosses and circles, respectively. The Birks model has been fitted to each data set for comparison. The `ExcitonQuenching` computed responses for both scintillators using the three track structure models are shown with lines. The ratio of the response from each model to the experimental values are shown below for both scintillators.

5.2. Ionization quenching correction factors

The QCF measurements by Wang *et al* (2012) comprise several points between 5 MeV cm^{-1} and 70 MeV cm^{-1}. However, more than half the measurements are below 25 MeV cm^{-1} and most measurements above 40 MeV cm^{-1} are associated with large uncertainties. In that light, it is not surprising that the three computed fluorescence signals in figure 6, including ionization quenching, are within few percent of the measurements for LET values up to 50 MeV cm^{-1} but deviate up to $\pm 10\%$ for higher LET values.

The BC-400 has a light yield around 40% larger than the BCF-12 scintillator, as is shown in table 1, and is thus in the Blanc model expected to give rise to a larger degree of quenching due to its larger initial exciton density. However, the $\sim$35% lower scintillator decay time for the BC-400 in turn causes a faster fluorescence emission which reduces the quenching. Hence, the fluorescence emission in the BC-400 scintillator differs greatly from that of the BCF-12 scintillator and therefore serves as a means of testing the Blanc model.

The Blanc model with its fitted parameters is assessed against the BC-400 data by Torrisi (2000) in figure 6. The Scholz–Kraft and Chatterjee–Schaefer track structure models both predict the quenching signal within $\pm 5\%$ of the measurements. The model-predicted signal divided by the measured signal in the lower part of the figure seems to contain the same structure in all four cases. On the other hand, the lack of a particle energy-dependent penumbral radius causes the Gaussian model to overestimate the ionization quenching for low-LET and vice versa for high-LET. The fact that the modified Blanc model follows the same structure as the Birks model in figure 6 was anticipated, as the Birks model is contained within and a simplified solution to the Blanc model as stated above. The agreement between `ExcitonQuenching` and the experimental data at high-LET in figure 6 is better for the BC-400 scintillator than for the BCF-12 scintillator. This might be explained by the fact, that Torrisi (2000) used thin scintillator pieces which gave an excellent LET-resolution whereas the high-LET measurements by Wang *et al* (2012) contain large uncertainties. Similarly for `ExcitonQuenching`, the uncertainties associated with the input parameters give rise to an uncertainty of the QCF. A $\pm 2\%$ variation in the scintillator light yield for the BCF-12 scintillator changes the computed QCF about $\pm 2\%$ for a proton with 50 MeV cm^{-1}. The similar variation of the light yield in the BC-400 scintillator exposed to the same proton energy however gives a variation about 4% of the QCF due to its larger light yield.

Nonetheless, the excellent agreement within few percent between the Birks and Blanc models for especially the Chatterjee–Schaefer track structure validates the application of the Blanc model, as the results are calculated completely independently: the Birks model by fitting to the experimental data, whereas the Blanc model response is computed numerically by solving the partial differential equation with initial conditions given by the specific particle and plastic scintillator.

The Blanc model furthermore explains why the fluorescence emission in a PMMA-based optical fibre during proton irradiations is reported to be quenching-free (Jang *et al* 2012, Christensen *et al* 2018); the low light yield A in PMMA, relative to a traditional scintillator, gives rise to such a low initial linear exciton density ($n \propto A$) that $\alpha n^2 \approx \beta n^3 \approx 0$ in equation (2) even for high-LET. Consequently, QCF $\simeq 1$ in the workflow in figure 3(c) corresponding to negligible quenching.

6. Conclusion

The open source software `ExcitonQuenching` combines amorphous track structure theory and the Blanc model to compute theoretical quenching correction factors for organic scintillators exposed to ions. Hence, it provides a new method—and more general than that due to Birks—to correct the ionization quenching from first principles which otherwise is a cumbersome experimental procedure.

The local exciton densities for proton relevant LETs are sufficient for bimolecular quenching to occur whereas the trimolecular quenching is almost vanishing for protons in the investigated water-equivalent materials. As a consequence, trimolecular quenching is not included in the online version of `ExcitonQuenching` but may be relevant for particles with higher LET.

The theoretically computed QCFs are compared to experimentally obtained QCFs for two plastic scintillators which differ greatly in their emission properties and thus quenching. The theoretical QCFs for the Scholz–Kraft and Chatterjee–Schaefer track structure models are within 3% of the Birks model for low-LET and 5% for high-LET for the BC-400 scintillator. The agreement between `ExcitonQuenching` and experimental data for the BCF-12 scintillator is within 2% for LET-values below 45 MeV cm^{-1}, where the experimental uncertainties were small. The discrepancy however increases up to 10% for the largest LET-values where the experimental measurements contain relative uncertainties of 8%.

`ExcitonQuenching` depends on the density, decay time, and light yield of the scintillator, and thus constitutes a new method to compute QCFs for organic plastic scintillator exposed to ions without prior knowledge of the quenched scintillator response from experimental data.

Acknowledgments

The work was supported by the Danish Cancer Society and the Danish Council for Independent Research (grant FTP, DFF—4184-00151). We thank Professor Lorenzo Torrisi for providing the original data of the luminescence response of the BC-400 scintillator during proton irradiations.

Appendix A. Amorphous track structure models

Any track structure must satisfy $2\pi \int_0^\infty n(r)\, r\mathrm{d}r = N_0$. The three track structure models are compared for protons in water in figure 1 for two energies.

A.1. Gaussian

The Gaussian distribution is of the form

$$n_{\mathrm{Gaussian}}(r,0) = \frac{N_0}{\pi b^2} \exp\left(-\frac{r^2}{b^2}\right), \tag{A.1}$$

where $b = 2r_0/\sqrt{\pi}$ (Blanc *et al* 1962). Birks (1964) sets $r_0 = 0.5 \times 10^{-6}$ cm, as obtained by Kallmann and Brucker (1957) for heavily ionizing particles. The main drawback of the Gaussian track structure is, that the energy-dependent range of the secondary electrons is unaccounted for. Blanc *et al* (1964) applied a Gaussian distribution to solve equation (2) with $\beta = 0$ analytically using several approximations.

A.2. Scholz–Kraft

The Scholz–Kraft track structure models the energy deposition as a dense core of radius $r_{\mathrm{min}} = 0.01\,\mu$m which falls off proportionally to r^{-2} until the maximum range of the secondary electrons

$$r_{\mathrm{max}} = 0.05\,\mu\mathrm{m}\,\mathrm{MeV}^{-1.7} \times E^{1.7}$$

has been reached:

$$n_{\mathrm{SK}}(r) = \begin{cases} \frac{N_0}{r_{\mathrm{min}}^2}\left(\pi\left[1 + 2\,\ln\frac{r_{\mathrm{max}}}{r_{\mathrm{min}}}\right]\right)^{-1} & \text{for} \quad r < r_{\mathrm{min}} \\ \frac{N_0}{r^2}\left(\pi\left[1 + 2\,\ln\frac{r_{\mathrm{max}}}{r_{\mathrm{min}}}\right]\right)^{-1} & \text{for} \quad r_{\mathrm{min}} \leqslant r \leqslant r_{\mathrm{max}} \\ 0 & \text{for} \quad r > r_{\mathrm{max}}. \end{cases} \tag{A.2}$$

A.3. Chatterjee–Schaefer

The Chatterjee–Schaefer model has a denser core than the Scholz–Kraft model with radius

$$r_{\min} = r_{\text{core}}\,\beta_{\text{ion}}, \tag{A.3}$$

where $r_{\text{core}} = 11.6\,\text{nm}$ and $\beta_{\text{ion}} = v/c$ is the ratio of the speed v to the speed of light c. The outer border of the penumbra has a radius of

$$r_{\max} = 0.768\ \mu\text{m}\ \text{MeV}^{-1} \times E - 1.925\ \mu\text{m}\,\text{MeV}^{-0.5} \times \sqrt{E} + 1.257\ \ \mu\text{m}$$

and will consequently give rise to a relatively large amount of ionization quenching in the core:

$$n_{\text{CS}}(r) = \begin{cases} \frac{N_0}{2\pi r_{\min}^2} + \frac{N_0}{4\pi r_{\min}^2}\left(\ln\left(\sqrt{e}\frac{r_{\max}}{r_{\min}}\right)\right)^{-1} & \text{for} \quad r < r_{\min} \\ \frac{N_0}{4\pi r^2}\left(\ln\left(\sqrt{e}\frac{r_{\max}}{r_{\min}}\right)\right)^{-1} & \text{for} \quad r_{\min} \leqslant r \leqslant r_{\max} \\ 0 & \text{for} \quad r > r_{\max} \end{cases} \tag{A.4}$$

with more than half the excitations inside the core. The Scholz–Kraft and Chatterjee–Schaefer models are developed for water and thus the core and penumbra radii are scaled with the density of the water-equivalent plastic scintillator in question.

Appendix B. Numerical scheme

The cylindrical symmetry of the track structure models reduces the problem to be one dimensional; the LET of the ion along its path is approximately constant on the microscopical scale, which in turn causes the second derivative of the excitation density in equation (2) to vanish along the trajectory, and only the radial diffusion is left.

The one dimensional mesh of length $L = 2r_{\max}$, where the ion trajectory is centred, defines the solution domain. The distance between two neighbouring voxels Δx is limited by $\Delta x < r_{\min}/l$, where $l > 1$ is chosen to satisfy the natural requirement that a numerical integration over the excitation densities in the mesh grid must equal the analytical integration. For the Scholz–Kraft and Chatterjee–Schaefer track structures, $l > 20$ turned out fulfil the said requirement, whereas $\Delta x < r_0/5$ was sufficient for the Gaussian case.

The explicit Lax–Wendroff scheme (Lax and Wendroff 1960) is applied to solve the partial differential equation. The derivatives of the exciton density n_i^m for voxel $i \in [1, 2, \ldots, L/\Delta x - 1]$ at time step m are

$$\left.\frac{\partial n}{\partial t}\right|_i^m \simeq \frac{n_i^{m+1} - n_i^m}{\Delta t} \quad \text{and} \quad \left.\frac{\partial^2 n}{\partial x^2}\right|_i^m \simeq \frac{n_{i+1}^m - 2n_i^m + n_{i-1}^m}{(\Delta x)^2}.$$

The time step Δt is subject to the von Neumann stability conditions (Press *et al* 1988, Dehghan 2004). The open-source code library `libamtrack` (Toftegaard *et al* 2014) is used to calculate the LET and β_{ion} in equation (A.3) depending on the particle energy.

ORCID iDs

Jeppe Brage Christensen https://orcid.org/0000-0002-6894-381X
Claus E Andersen https://orcid.org/0000-0002-7356-9607

References

Alsanea F, Therriault-Proulx F, Sawakuchi G and Beddar S 2018 A real-time method to simultaneously measure linear energy transfer and dose for proton therapy using organic scintillators *Med. Phys.* **45** 1782–9

Archambault L, Beddar A S, Gingras L, Roy R and Beaulieu L 2005 Measurement accuracy and Cerenkov removal for high performance, high spatial resolution scintillation dosimetry *Med. Phys.* **33** 128–35

Beddar A S, Mackie T R and Attix F H 1992a Water-equivalent plastic scintillation detectors for high-energy beam dosimetry: I. Physical characteristics and theoretical considerations *Phys. Med. Biol.* **37** 1883–900

Beddar A S, Mackie T R and Attix F H 1992b Water-equivalent plastic scintillation detectors for high-energy beam dosimetry: II. Properties and measurements *Phys. Med. Biol.* **37** 1901–13

Beddar S and Beaulieu L 2016 *Scintillation Dosimetry* (Boca Raton, FL: CRC Press)

Birks J B 1951 Scintillation from organic crystals: Specific fluorescence and relative response to different radiation *Proc. Phys. Soc.* A **64** 874–7

Birks J B 1964 *The Theory and Practice of Scintillation Counting: International Series of Monographs in Electronics and Instrumentation* vol 27 (Amsterdam: Elsevier)

Blanc D, Cambou F and Lafond Y G D 1962 Kinetics of the fast component of scintillation in a pure organic medium. Application to anthracene *C. R. l'Acad. Sci., Paris* **18** 3187–9

Blanc D, Cambou F and Lafond Y G D 1964 Etude cinétique de la scintillation dans les cristaux organiques purs *J. Physique* **25** 319–25
Boivin J, Beddar S, Bonde C, Schmidt D, Culberson W, Guillemette M and Beaulieu L 2016 A systematic characterization of the low-energy photon response of plastic scintillation detectors *Phys. Med. Biol.* **61** 5569–86
Buranurak S, Andersen C E, Beierholm A R and Lindvold L R 2013 Temperature variations as a source of uncertainty in medical fiber-coupled organic plastic scintillator dosimetry *Rad. Meas.* **56** 307–11
Chatterjee A and Schaefer H J 1976 Microdosimetric structure of heavy ion tracks in tissue *Rad. Environ. Biophys.* **13** 215–27
Chou C N 1952 The nature of the saturation effect of fluorescent scintillators *Phys. Rev.* **5** 904–5
Christensen J B, Almhagen E, Nyström H and Andersen C E 2018 Quenching-free fluorescence signal from plastic-fibres in proton dosimetry: understanding the influence of Čerenkov radiation *Phys. Med. Biol.* **63** 065001
Dehghan M 2004 Numerical solution of the three-dimensional advection—diffusion equation *Appl. Math. Comput.* **150** 5–19
Hansen J W and Olsen K J 1984 Experimental and calculated response of a radiochromic dye film dosimeter to high-LET radiations *Radiat. Res.* **97** 1–15
Hoer C, Lindsay C, Beaudry J, Penner C, Strgar V, Lee R and Duzenli C 2018 Characterization of the exradin W1 plastic scintillation detector for small field applications in proton therapy *Phys. Med. Biol.* **63** 095016
Jang K W, Yoo W J, Shin S H, Shin D and Lee B 2012 Fiber-optic Čerenkov radiation sensor for proton therapy dosimetry *Opt. Express* **20** 13907–14
Kallmann H and Brucker G J 1957 Decay times of fluorescent substances excited by high-energy radiation *Phys. Rev.* **108** 1122–30
Katz R and Varma M N 1991 *Radial Distribution of Dose* (Boston: Springer) pp 163–80
Kiefer J and Straaten H 1986 A model of ion track structure based on classical collision dynamics *Phys. Med. Biol.* **31** 1201–9
Lax P and Wendroff B 1960 Systems of conservation laws *Commun. Pure Appl. Math.* **13** 217–37
Newman E and Steigert F E 1960 Response of NaI(Tl) to energetic heavy ions *Phys. Rev.* **118** 1575–8
Press W H, Teukolsky S A, Vetterling W T and Flannery B P 1988 *Numerical Recipes in C The Art of Scientific Computing* (Cambridge: Cambridge University Press)
Scholz M and Kraft G 1996 Track structure and the calculation of biological effects of heavy charged particles *Adv. Space Res.* **18** 5–14
Therriault-Proulx F, Beddar S, Briere T M, Archambault L and Beaulieu L 2011 Technical note: removing the stem effect when performing Ir-192 HDR brachytherapy *in vivo* dosimetry using plastic scintillation detectors: a relevant and necessary step *Med. Phys.* **38** 2176–9
Toftegaard J, Lühr A, Sobolevsky N and Bassler N 2014 Improvements in the stopping power library `libdEdx` and release of the web GUI `dedx.au.dk` *J. Phys.: Conf. Ser.* **489** 012003
Torrisi L 2000 Plastic scintillator investigations for relative dosimetry in proton-therapy *Nucl. Instrum. Methods Phys. Res.* **170** 523–30
Wang L L, Perles L A, Archambault L, Sahoo N, Mirkovi D and Beddar S 2012 Determination of the quenching correction factors for plastic scintillation detectors in therapeutic high-energy proton beams *Phys. Med. Biol.* **57** 7767–81
Wootton L and Beddar S 2013 Temperature dependence of BCF plastic scintillation detectors *Phys. Med. Biol.* **58** 2955–67

Paper III

Title:

Applications of amorphous track structure models for correction of ionization quenching in organic scintillators exposed to ion beams

Authors:

Christensen JB and Andersen CE

Submitted to:

Radiation Measurements,
September 2018.

Status:

Published January 2019.

Digital Object Identifier:

10.1016/j.radmeas.2019.01.003

Radiation Measurements 124 (2019) 158–162

Contents lists available at ScienceDirect

Radiation Measurements

journal homepage: www.elsevier.com/locate/radmeas

Applications of amorphous track structure models for correction of ionization quenching in organic scintillators exposed to ion beams

Jeppe Brage Christensen*, Claus E. Andersen

Center for Nuclear Technologies, Technical University of Denmark, 4000, Roskilde, Denmark

ARTICLE INFO

Keywords:
Ionization quenching
Organic plastic scintillators
Ion beam dosimetry
Amorphous track structure theory
Particle therapy

ABSTRACT

The scintillation response of organic plastic scintillators irradiated with heavy ions is investigated with the open-source code ExcitonQuenching. The software relies on amorphous track structure theory to account for the radial energy deposition by secondary electrons (EDSE) in ion tracks. The kinematic Blanc model is applied to evaluate the ionization quenching for a given ion by taking the decay time, light yield, and density of the scintillator into account. ExcitonQuenching predicts the scintillation response without a priori knowledge of any measured response curves in contrast to other EDSE models, such as the correction method due to Birks, which rely on free fitting parameters for each ion. ExcitonQuenching is validated against published measurements of the Pilot-U scintillator exposed to several ions. The agreement with experimental data is between 5% and 9% for ions with atomic number $z \leq 6$ but deviates more for heavier ions.

1. Introduction

Water equivalent organic plastic scintillator detectors coupled to optical fibers for remote read out (Beddar et al., 1992a, b) enable measurements of absorbed dose with minimal perturbation and a high degree of resolution in time (<1 ms) and space (sub-mm). While both the temperature variations (Buranurak et al., 2013) of the scintillator and the radiation induced stem-effect in the fibre (Archambault et al., 2005) are well-understood and may be corrected for, the scintillators suffer in line with other solid state detectors from a response that is nonproportional to the local energy deposition. The reduced scintillator response occurring at high ionization densities, termed ionization quenching or nonproportionality, remains a challenge. Several kinematic models have been proposed to correct ionization quenching in inorganic scintillators (Michaelian and Menchaca-Rocha, 1994; Vasil'ev, 2008; Williams et al., 2010) but few have been suggested for organic materials.

Birks (1951) suggested a semi-empirical model to correct the scintillator signal for ionization quenching which later was extended by Chou (1952) for particles with a high linear energy transfer (LET) with an additional free parameter. Nonetheless, neither of the models account for the local ionization density in ion tracks. The radial energy deposition by secondary electrons (EDSE) in the tracks of two ions with the same LET, but different atomic numbers, differ due to the ranges of the liberated secondaries. The differing ionization densities in the ion tracks thus cause the scintillation responses to differ as experimentally observed by Buenerd et al. (1976). Consequently, the Birks and Chou models require experimentally determined correction factors for each particle and each scintillator in question.

Michaelian and Menchaca-Rocha (1994) approached the ionization quenching issue with a model based on the EDSE and were as such capable of distinguishing between the quenching from different particles with the same LET. However, their model requires determination of several free quenching parameters by fitting the model to experimentally obtained data. The present work investigates the numerical framework ExcitonQuenching (Christensen and Andersen, 2018) for the case of plastic scintillators exposed to ions heavier than protons.

The software combines amorphous track structure theory and the decay time, light yield, and density of the scintillator to estimate the local ionization densities, upon which the scintillator response is evaluated through a kinematic model. ExcitonQuenching is in contrast to other EDSE models able to predict the quenched scintillator response without fitting parameters to specific response curves and can furthermore quantify the temporal structure of ionization quenching. The open-source software ExcitonQuenching is accessible for download[1] to correct the ionization quenching in organic plastic scintillators exposed to ions.

* Corresponding author.
E-mail address: jepb@dtu.dk (J.B. Christensen).
[1] https://github.com/jbrage/ExcitonQuenching

https://doi.org/10.1016/j.radmeas.2019.01.003
Received 3 October 2018; Received in revised form 30 November 2018; Accepted 10 January 2019
Available online 14 January 2019
1350-4487/

2. Methods

2.1. Ionization quenching

The luminescence dL per unit length dx as a function of a particle's linear energy transfer is often written as

$$\frac{\mathrm{d}L}{\mathrm{d}x} = \frac{A\cdot \mathrm{d}E/\mathrm{d}x}{\mathrm{QCF}}, \quad \mathrm{QCF} = 1 + kB\cdot \mathrm{d}E/\mathrm{d}x, \tag{1}$$

where A denotes the light yield of the scintillator in units of photons emitted per deposited energy, and the quenching correction factor (QCF) is expressed as a linear function with slope kB in the Birks model. The scintillator response L for a particle with kinetic energy E may consequently be computed from eq. (1) as

$$\frac{\mathrm{d}L}{\mathrm{d}E} = A\cdot \mathrm{QCF}^{-1} \Rightarrow L = \int_0^E A\cdot \mathrm{QCF}^{-1}\,\mathrm{d}E \tag{2}$$

for a thick scintillator. The QCF for a given ion and scintillator is a function of the kinetic energy and the EDSE which can be achieved through a track structure.

2.2. Amorphous track structures

Amorphous track structure theory models the EDSE as a continuous radial function and the local ionization density based on the kinetic energy of the primary particle and the material composition of the medium. The present work focuses on the Chatterjee-Schaefer track structure model (Chatterjee and Schaefer, 1976), which consists of a dense core region of enormous ionization density and a penumbral region with the characteristic r^{-2} radial decrease. The Chatterjee-Schaefer track structure model is defined in eq. (A.1) and illustrated in Fig. 1 for different ions with the same LET. As the ion core regions may exhibit huge excitation densities for slow, heavy ions, the Chatterjee-Schaefer quenching results are compared to the quenching results for the Scholz-Kraft track structure model (Scholz and Kraft, 1996) to evaluate the influence of the applied track structure model. The Scholz-Kraft track structure model is outlined in eq. (A.2).

2.3. Kinematics of excited states

An ion depositing an energy dE per unit length dx in a scintillator gives rise to a linear density of $N = \mathrm{d}E/\mathrm{d}x\cdot A$ of excited states (excitons). The exciton distribution immediately after an ion traversed the material slab of unit length dx is radially distributed according to the Chatterjee-Schaefer track structure.

The excitons of density n in the ion track are in a kinematic model suggested by Blanc et al. (1962, 1964) allowed to diffuse, fluoresce, and quench according to

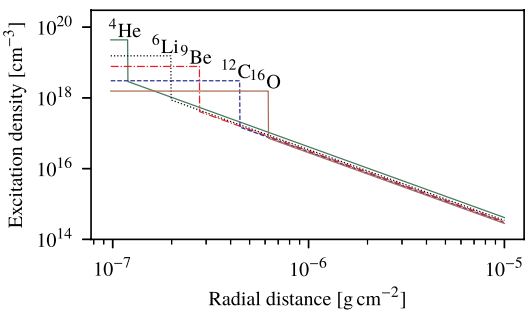

Fig. 1. Close-up of the track structures of five ions with $\mathrm{d}E/\mathrm{d}x = 30$ keVμm^{-1} in the Pilot-U scintillator modelled as suggested by Chatterjee and Schaefer (1976).

Table 1
The generic model parameters are calculated in Christensen and Andersen (2018) whereas the decay time τ, light yield A (relative to anthracene), and density ρ for the Pilot-U plastic scintillator are given by the manufacturer (Eljen Technology, USA).

Generic parameters		Scintillator parameters		
D	α	τ	A	ρ
[cm^2 s^{-1}]	[cm^3 s^{-1}]	[ns]	[%]	[gcm^{-3}]
5.9×10^{-4}	1.0×10^{-9}	1.4	67	1.023

$$\frac{\partial n}{\partial t} = D\nabla^2 n - (p + k)n - \alpha n^2, \tag{3}$$

where the diffusion constant D and bimolecular quenching parameter α are estimated from fits in Christensen and Andersen (2018) and listed in Table 1. The unimolecular quenching parameter k and the rate of fluorescence emission p are related to the decay time τ of the scintillator via $\tau^{-1} = p + k$ (Birks, 1964) and weighted equally. Eq. (3) models the fluorescence emission from the first excited singlet state to the ground state (Blanc et al., 1962).

2.4. Quenching correction factors

The kinematic eq. (3) governs the exciton interactions where the initial exciton distribution is given by the track structure model and scintillator light yield and material composition. The emitted light is calculated by solving eq. (3) numerically (see Christensen and Andersen (2018) for details) while integrating over the fluorescence term pn. Solving eq. (3) with $\alpha = 0$ gives the light emission in the absence of ionization quenching while solving the same equation with $\alpha \neq 0$ gives the quenched scintillator response. The corresponding QCF can consequently be obtained as the ratio of the unquenched signal to the quenched signal.

The following section applies ExcitonQuenching to investigate the ionization quenching in an organic plastic scintillator (Pilot-U, Eljen Technology, USA) which was subject to irradiation with several ions heavier than protons by Buenerd et al. (1976). The results are obtained as predictions without fitting free parameters to the experimentally determined scintillator responses for the Pilot-U scintillator in contrast to the Birks model and most EDSE models.

3. Results

3.1. Ionization quenching

The QCF is calculated with ExcitonQuenching for ^{4}He, ^{6}Li, ^{9}Be, ^{12}C, and ^{16}O ions for a wide range of kinetic energies in the Pilot-U scintillator, where the LET as a function of energy for a given ion and material composition is calculated as suggested by Bird and Williams (1990). The QCFs as a function of LET is shown in Fig. 2 where the Birks model in eq. (1) has been fitted to each set of calculated QCFs.

The scintillation efficiency dL/dE for the five ions are calculated according to eq. (2) as a function of the QCF which in turn depends on the kinetic energy of the particle. The results are shown in Fig. 3 as a function of kinetic energy.

3.1.1. Light emission for isotopes

The scintillation efficiency for three isotopes of hydrogen, helium, and lithium are in Fig. 4 calculated as a function of velocity $\beta = v/c$ and velocity per atomic number β/z, respectively. The scintillation efficiency converges in all cases towards a quenching-free level for $\beta \to 1$, corresponding to QCF → 1 in eq. (2).

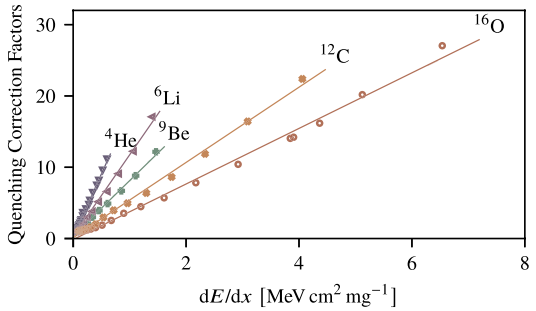

Fig. 2. The quenching correction factor as a function of LET for five ions is calculated with ExcitonQuenching plotted with symbols. The Birks model is fitted to each set of data shown with solid lines.

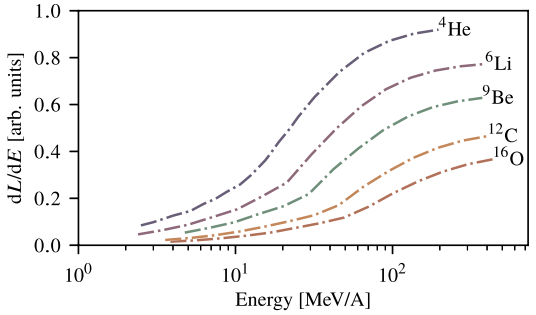

Fig. 3. Theoretical light emission per energy as a function of kinetic energy in eq. (2) for the Pilot-U scintillator irradiated with different ions.

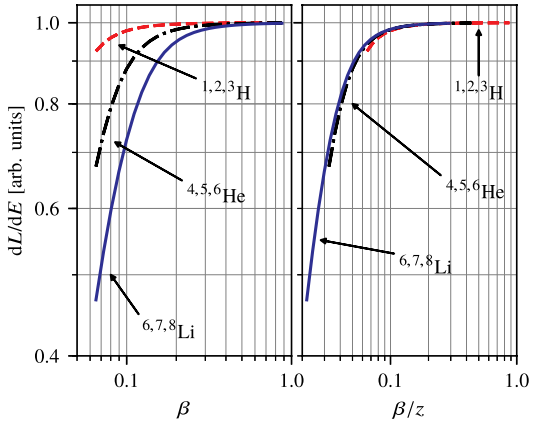

Fig. 4. The scintillation efficiency dL/dE for 3 isotopes of hydrogen, helium, and lithium as a function of (*left*) velocity and (*right*) velocity per atomic number z. All efficiencies coincide in the latter case.

3.2. Light output

The luminescence response from the plastic scintillator induced by a stopped ion of kinetic energy E is calculated by integrating dL/dE over the kinetic energy as given by eq. (2), where the QCF as a function of kinetic energy is interpolated for a continuous integration. The theoretical results are compared to the experimental results obtained by

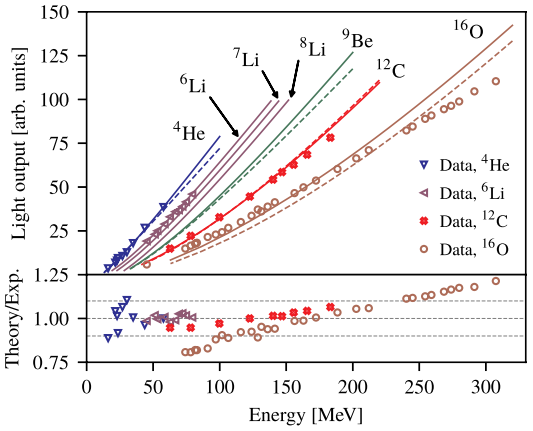

Fig. 5. The light emission as a function of kinetic energy for ions stopping in the plastic scintillator. The calculated ExcitonQuenching results are shown with solid lines (Chatterjee-Schaefer track structure) and dashed lines (Scholz-Kraft track structure), whereas the experimental data points from Buenerd et al. (1976) with symbols as given by the legend. The luminescence is shown for three isotopes of lithium for comparison. The ratios between the ExcitonQuenching calculated responses (solid lines) to the experimentally measured scintillation responses are shown below where the dashed horizontal lines show ± 10% discrepancies.

Buenerd et al. (1976) in Fig. 5, where the results are collectively scaled to the experimental data with a single value. The light output is calculated for all ions using the Chatterjee-Schaefer and Scholz-Kraft track structures where the isotopes ^{7,8}Li and ^{9}Be are shown for reference.

4. Discussion

4.1. Track structure theory

The ion core densities for the five different ions in Fig. 1 with the same dE/dx = 30 keVμm^{-1} span almost two orders of magnitude and illustrate the importance of the track structure models; the oxygen ion ($E \approx 190$ MeV/A) liberates secondaries with significantly larger kinetic energies than the α particle ($E \approx 5.5$ MeV/A). The core and penumbra radii in the oxygen ion track are consequently broader which in turn reduce the ionization density and quenching. The variation of the QCFs as a function of dE/dx in Fig. 2 illustrates how the ionization quenching varies with the atomic number and dE/dx as experimentally confirmed by Newman and Steigert (1960).

4.2. Scintillation efficiency

The scintillation efficiency in Fig. 3 as a function of energy shows how lighter ions more efficiently convert energy into luminescence for a given energy. The scintillation efficiency for each ion slowly converges as the kinetic energy increases in turn reducing the ionization density of core region and quenching, which also was observed experimentally (Murray and Meyer, 1961).

The luminescence responses for the isotopes of a given element coincide as a function of velocity in Fig. 4, which also was experimentally confirmed by Avdeichikov et al. (2002) for the case of BGO exposed to light ions. The scintillation efficiency as a function of velocity per atomic number is approximately the same for all ions as explained and measured by Sibczynski et al. (2018) for GAGG:Ce excited by alpha particles.

4.3. Light emission

The scintillation response curves in Fig. 5, as ions are stopped in the plastic scintillator, illustrate the variation of luminescence efficiency with atomic number. The emitted light as a function of kinetic energy differs between isotopes of the same element, as illustrated in the figure with the 3 isotopes of lithium, which is in line with the experimentally measured responses reported by Avdeichikov et al. (2002) and Fig. 4.

The agreement between the ExcitonQuenching calculated and experimentally measured scintillation response curves for helium, lithium, and carbon ions confirms the application of track structure theory and the kinematic Blanc model to compute the ionization quenching for $z \leq 6$ ion beams. However, the deviation between the predicted and measured response for oxygen ions (as much as $\pm$ 25%) in Fig. 5 exhibits a structure where the response is underestimated for low energies and overestimated for high energies. The magnitude and structure of the discrepancy between the two track structure models and the data are similar, implying that the deviation between theory and experimental data is related to the model itself and not the particular amorphous track structure model in question.

The kinematic Blanc model in eq. (3) governs the fluorescence emission from de-excitation of the first singlet state but does not account for triplet state interactions. Two triplet states may interact and give rise to one molecule in the ground state and one molecule in the singlet state and as such leading to fluorescence emission at a slower time scale than normally observed (Michaelian and Menchaca-Rocha, 1994; Jain et al., 2009). Thus, the probability for a bimolecular interaction between two triplet states and subsequent fluorescence emission increases with the local ionization density and occurs more frequently in carbon and oxygen ion tracks than in lighter ion tracks as helium and lithium. The possibility of extending the kinematic Blanc model to include triplet state interactions was suggested by Blanc et al. (1964) but is out of the scope of the present work.

Another explanation of the deviation may be found in the current equation itself, where higher-order density terms may be required to balance the high-LET ions. Such a conclusion is in line with Torrisi (2000) where the Birks model with an additional free parameter, i.e. the Chou model, was concluded to provide a better fit to the data for high-LET.

The good agreement between data and ExcitonQuenching for $z \leq 6$ ions matches the results in Christensen and Andersen (2018), where the software accurately predicted the scintillation response for another plastic scintillator (BCF-60, Saint-Gobain, France) irradiated with protons.

5. Conclusion

The open-source software ExcitonQuenching predicts the quenched scintillation response in plastic scintillators exposed to ion beams based on amorphous track structure theory and a kinematic exciton model. The agreement between the software and experimental data for helium, lithium and carbon ions is, except for one outlier, better than 9%, and as such in line with traditionally reported experimental uncertainties. The large discrepancy between the model and data for oxygen ions indicates that an additional model parameter, along with the inclusion of triplet state interactions, are required for high-LET ions.

Nonetheless, ExcitonQuenching accurately predicts the ionization quenching in the organic plastic scintillator exposed to ions with $z \leq 6$ based on the decay time, light yield, and density of the scintillator without any fit to the data. Such a predictive capability is in sharp contrast to most available EDSE models which contain free parameters requiring fits to each set of experimental data.

Acknowledgement

The work was supported by the Danish Cancer Society and the Danish Council for Independent Research (grant FTP, DFF 4184-00151). The authors wish to thank Dr. Fahed M. Alsanea, MD Anderson Cancer Center, for discussions pertaining to ionization quenching and EDSE models.

Appendix A. Amorphous track structure models

Chatterjee-Schaefer. The track structure model due to Chatterjee and Schaefer (1976) consists of a dense core with radius defined as

$r_{\min} = \beta_{\text{ion}} \times 11.6$ nm,

where $\beta_{\text{ion}} = v/c$ is the ratio of the speed v to the speed of light c. The outer border of the penumbra has a radius of

$r_{\max} = 0.768E - 1.925\sqrt{E} + 1.257 \quad [\mu\text{m}]$

with the kinetic energy E in units of MeV/nucleon. The radial exciton density is given as

$$n(r) = \begin{cases} \frac{N}{4\pi}\left(\frac{2+C_1}{r_{\min}^2}\right) & \text{for} \quad r < r_{\min} \\ \frac{N}{4\pi}\frac{C_1}{r^2} & \text{for} \quad r_{\min} \leq r \leq r_{\max} \\ 0 & \text{for} \quad r > r_{\max} \end{cases} \tag{A.1}$$

where

$$C_1 = \left(\ln\left(\sqrt{e}\,\frac{r_{\max}}{r_{\min}}\right)\right)^{-1}$$

and $N = \mathrm{d}E/\mathrm{d}x \cdot A$.

Scholz-Kraft. With core and penumbral radii defined as

$r_{\max} = 0.05\, E^{1.7}\ \mu\text{m}, \qquad r_{\min} = 0.01\ \mu\text{m},$

where E [MeV/nucleon] is the kinetic energy of the projectile, the Scholz-Kraft track structure model governs a radial exciton density of

$$n(r) = \begin{cases} \frac{C_2}{r_{\min}^2} & \text{for} \quad r < r_{\min} \\ \frac{C_2}{r^2} & \text{for} \quad r_{\min} \leq r \leq r_{\max} \\ 0 & \text{for} \quad r > r_{\max} \end{cases} \tag{A.2}$$

for

$$C_2 = N\left(\pi\left[1 + 2\ln\frac{r_{\max}}{r_{\min}}\right]\right)^{-1}.$$

References

Archambault, L., Beddar, A.S., Gingras, L., Roy, R., Beaulieu, L., 2005. Measurement accuracy and Cerenkov removal for high performance, high spatial resolution scintillation dosimetry. Med. Phys. 33 (1), 128–135.

Avdeichikov, V., Jakobsson, B., Nikitin, V., Nomokonov, P., Wegner, A., 2002. Systematics in the light response of BGO, CsI (Tl) and GSO (Ce) scintillators to charged particles. Nucl. Instrum. Methods Phys. Res. Sect. A Accel. Spectrom. Detect. Assoc. Equip. 484 (1–3), 251–258.

Beddar, A.S., Mackie, T.R., Attix, F.H., 1992a. Water-equivalent plastic scintillation detectors for high-energy beam dosimetry: I. Physical characteristics and theoretical considerations. Phys. Med. Biol. 37 (10), 1883–1900.

Beddar, A.S., Mackie, T.R., Attix, F.H., 1992b. Water-equivalent plastic scintillation detectors for high-energy beam dosimetry: II. Properties and measurements. Phys. Med. Biol. 37 (10), 1901–1913.

Bird, R.C., Williams, J.S., 1990. Ion Beams for Materials Analysis. Elsevier.

Birks, J.B., 1951. Scintillation from organic crystals: specific fluorescence and relative response to different radiation. Proc. Phys. Soc. 64 (10), 874–877.

Birks, J.B., 1964. The Theory and Practice of Scintillation Counting: International Series of Monographs in Electronics and Instrumentation, vol. 27 Elsevier.

Blanc, D., Cambou, F., de Lafond, Y.G., de Lafond, Y.G., 1962. Kinetics of the fast component of scintillation in a pure organic medium. Application to anthracene. Comptes rendus de l'Académie des Sciences Paris 18, 3187–3189.

Blanc, D., Cambou, F., Lafond, Y.G.D., 1964. Etude cinétique de la scintillation dans les cristaux organiques purs. J. Phys. 25, 319.

Buenerd, M., Hendrie, D., Jahnke, U., Mahoney, J., Menchaca-Rocha, A., Olmer, C., Scott, D., 1976. Response of pilot u scintillator to heavy ions. Nucl. Instrum. Methods 136 (1), 173–177.

Buranurak, S., Andersen, C.E., Beierholm, A.R., Lindvold, L.R., 2013. Temperature variations as a source of uncertainty in medical fiber-coupled organic plastic scintillator dosimetry. Radiat. Meas. 56, 307–311.

Chatterjee, A., Schaefer, H.J., 1976. Microdosimetric structure of heavy ion tracks in tissue. Radiat. Environ. Biophys. 13 (3), 215–227.

Chou, C.N., 1952. The nature of the saturation effect of fluorescent scintillators. Phys. Rev. Lett. 5 (87), 904–905.

Christensen, J.B., Andersen, C.E., 2018. Relating ionization quenching in organic plastic scintillators to basic material properties by modelling excitation density transport and amorphous track structure during proton irradiation. Phys. Med. Biol. 63, 195010.

Jain, A., Blum, C., Subramaniam, V., 2009. Chapter 4 - fluorescence lifetime spectroscopy and imaging of visible fluorescent proteins. In: Verdonck, P. (Ed.), Advances in Biomedical Engineering. Elsevier, Amsterdam, pp. 147–176.

Michaelian, A., Menchaca-Rocha, A., 1994. Ion-induced luminescence based on energy deposition. Phys. Rev. B 49 (22), 550–562.

Murray, R., Meyer, A., 1961. Scintillation response of activated inorganic crystals to various charged particles. Phys. Rev. 122 (3), 815.

Newman, E., Steigert, F.E., 1960. Response of NaI(Tl) to energetic heavy ions. Phys. Rev. 118 (6), 1575–1578.

Scholz, M., Kraft, G., 1996. Track structure and the calculation of biological effects of heavy charged particles. Adv. Space Res.: the official journal of the Committee on Space Research 18 (1–2), 5–14.

Sibczynski, P., Czarnacki, W., Mianowska, Z., Mianowski, S., Moszynski, M., Sworobowicz, T., Swiderski, L., Bezbakh, A.A., Fomichev, A.S., Krupko, S.A., Sabelnikov, A.V., Kamada, K., Shoji, Y., Yoshikawa, A., 2018. Non-proportionality of GAGG:Ce scintillators down to 50 eV electron equivalent by application of alpha particle excitation. Nucl. Instrum. Methods Phys. Res. Sect. A Accel. Spectrom. Detect. Assoc. Equip. 898, 24–29.

Torrisi, L., 2000. Plastic scintillator investigations for relative dosimetry in proton-therapy. Nucl. Instrum. Methods Phys. Res. Sect. B Beam Interact. Mater. Atoms 170 (3), 523–530.

Vasil'ev, A.N., 2008. From luminescence non-linearity to scintillation non-proportionality. IEEE Trans. Nucl. Sci. 55 (3), 1054–1061.

Williams, R., Li, Q., Grim, J.Q., Ucer, K., Bizarri, G., Moses, W., 2010. Role of carrier diffusion and picosecond exciton kinetics in nonproportionality of scintillator light yield. In: Hard X-Ray, Gamma-Ray, and Neutron Detector Physics XII, vol. 7805. International Society for Optics and Photonics, pp. 78050K.

Paper IV

Title:

Ionization quenching in scintillators used for dosimetry of mixed particle fields

Authors:

Christensen JB, Almhagen E, Stolarczyk L, Vestergaard A, Bassler N and Andersen CE

Submitted to:

Physics in Medicine and Biology,
February 2019.

Status:

Published March 2019.

Digital Object Identifier:

10.1088/1361-6560/ab12f2

IOP Publishing Phys. Med. Biol. 64 (2019) 095018 (13pp) https://doi.org/10.1088/1361-6560/ab12f2

Physics in Medicine & Biology

IPEM Institute of Physics and Engineering in Medicine

PAPER

RECEIVED
11 February 2019

REVISED
18 March 2019

ACCEPTED FOR PUBLICATION
25 March 2019

PUBLISHED
29 April 2019

Ionization quenching in scintillators used for dosimetry of mixed particle fields

Jeppe Brage Christensen[1], Erik Almhagen[2,3], Liliana Stolarczyk[2,4], Anne Vestergaard[5], Niels Bassler[6,7,8] and Claus E Andersen[1]

[1] Center for Nuclear Technologies, Technical University of Denmark, Roskilde, Denmark
[2] Skandionkliniken, Uppsala, Sweden
[3] Medical Radiation Sciences, Department of Immunology, Genetics and Pathology, Uppsala University, Uppsala, Sweden
[4] Institute of Nuclear Physics Polish Academy of Sciences in Krakow, The Bronowice Cyclotron Centre, Krakow, Poland
[5] Danish Centre for Particle Therapy, Aarhus University Hospital, Aarhus, Denmark
[6] Medical Radiation Physics, Department of Physics, Stockholm University, Stockholm, Sweden
[7] Department of Oncology and Pathology, Medical Radiation Physics, Karolinska Institutet, Stockholm, Sweden
[8] Department of Experimental Clinical Oncology, Aarhus University Hospital, Aarhus, Denmark

E-mail: jepb@dtu.dk

Keywords: plastic scintillator, particle dosimetry, quenching, proton therapy

Abstract

Ionization quenching in ion beam dosimetry is often related to the fluence- or dose-averaged linear energy transfer (LET). Both quantities are however averaged over a wide LET range and a mixed field of primary and secondary ions. We propose a novel method to correct the quenched luminescence in scintillators exposed to ion beams. The method uses the energy spectrum of the primaries and accounts for the varying quenched luminescence in heavy, secondary ion tracks through amorphous track structure theory. The new method is assessed against more traditional approaches by correcting the quenched luminescence response from the BCF-12, BCF-60, and 81-0084 plastic scintillators exposed to a 100 MeV pristine proton beam in order to compare the effects of the averaged LET quantities and the secondary ions. Calculations and measurements show that primary protons constitute more than 92% of the energy deposition but account for more than 95% of the luminescence signal in the scintillators. The quenching corrected luminescence signal is in better agreement with the dose measurement when the secondary particles are taken into account. The Birks model provided the overall best quenching corrections, when the quenching corrected signal is adjusted for the number of free model parameters. The quenching parameter kB for the BCF-12 and BCF-60 scintillators is in agreement with literature values and was found to be $kB = (10.6 \pm 0.1) \times 10^{-2}$ μm keV^{-1} for the 81-0084 scintillator. Finally, a fluence threshold for the 100 MeV proton beam was calculated to be of the order of 10^{10} cm^{-2}, corresponding to 110 Gy, above which the quenching increases non-linearly and the Birks model no longer is applicable.

1. Introduction

Organic plastic scintillators are attractive for particle dosimetry due to a prompt signal, good water equivalence, and a small volume (Beddar *et al* 1992a, 1992b). Nonetheless, the luminescence signal deviates from the dose deposition along the beam axis, an under response termed ionization quenching, as the linear energy transfer (LET) increases. Several methods have been suggested to correct the ionization quenching in solid state detectors: a semi-empirical formula due to Birks (1951) has historically been successfully applied to correct the ionization quenching in scintillators, although the model requires *a priori* knowledge about the quenched response and is incapable of predicting the quenching. Murray and Meyer (1961) demonstrated a shortcoming for the model for ions, while (Boivin *et al* 2016) recently showed how the model breaks down for low-energy photons. The Birks model was extended by Chou (1952) with an additional quenching parameter with mixed success; Birks (1964) examined the Chou model and found the best fit when the additional parameter vanished, thereby reducing it to the Birks model. That is in contrast to Torrisi (2000) who obtained a better agreement between the model and data

when the additional parameter is included. However, neither the Chou nor Birks model accounts for the radial energy deposition by secondary electrons (EDSE), which requires the model parameters to be experimentally determined for each primary ion and scintillator while the luminescence from heavier, secondary ions is omitted. Furthermore, the models cannot account for the temporal structure of quenching.

Blanc *et al* (1962, 1964) proposed a kinematic quenching model relying on the light yield and decay time of the scintillator, which can be simplified to the Birks model (Birks 1964) without the temporal component. The model allows excited states (excitons) to diffuse, fluorescence, and quench which enables a calculation of the quenching as well as quantifying the temporal structure of the quenched luminescence signal. The Blanc model has been implemented in the open-source software `ExcitonQuenching` (Christensen and Andersen 2018) which applies amorphous track structure theory to distribute the initial exciton density in an ion track. Amorphous track structure theory models, in contrast to a stochastic track structure theory, the radial energy deposition with a continuous penumbral region and a dense core region depending on the kinetic energy and LET of the given ion. `ExcitonQuenching` is consequently able to calculate the temporal structure of quenching as well as distinguishing between the quenching in ions with different atomic number through track structure theory, unlike the Birks and Chou models.

Secondary protons and heavier ions in a clinical proton beam constitute as much as 8% of the total dose (Paganetti 2002). The LET contribution from secondary protons gives rise to an elevated LET which can have an impact on the the relative biological effectiveness (RBE) (Grassberger and Paganetti 2011). The situation is reversed in scintillator dosimetry, where the high-LET secondary particles quench the luminescence more than the primary protons. Grzanka *et al* (2018) recently investigated the LET distribution in a spread out Bragg peak in a proton beam with a distinction between the LET from primary protons and all primaries calculated in terms of the fluence-averaged LET (LET_Φ) and dose-averaged LET (LET_D). The distinction between the primaries and all particles gave as much as ≈300% LET differences and highlights the importance of LET calculations for quenching corrections. The LET_D was recently shown to be a questionable predictor for the RBE (Grün *et al* 2018), as the LET_D poorly resembles a broad LET distribution, which similarly would give rise to a biased quenching correction in scintillator dosimetry. This motivates an investigation of how the averaging of the mixed particle field and the LET spectrum affects the quenching corrections in ion beams.

The present work applies the `ExcitonQuenching`, Birks, and Chou models to correct the ionization quenching in three organic plastic scintillators exposed to a pristine proton beam where the primary particles and nuclear fragments are taken into account. We assess how the LET-averaging affects the quenching corrections relative to the use of the entire LET spectrum and secondary ions. Furthermore, the traditional quenching correction methods rely on the implicit assumption that ionization quenching in ion tracks are independent events; such a presumption is assessed with `ExcitonQuenching`, where the temporal and spatial components enable an estimation of a fluence threshold, above which the excitons in ion tracks will interact on average and increase the ionization quenching.

2. Materials and methods

2.1. Experimental setup

Three organic, plastic scintillators (BCF-12 and BCF-60, Saint-Gobain, France; 81-0084, Industrial Fiber Optics, Inc, USA) with a diameter of 1 mm and 2 mm length were coupled to optical fibers connected to the ME-40 data acquisition system (Andersen 2011). The scintillators were irradiated in a water phantom with 100 MeV protons in a spot-scanned beam at the Skandion Clinic, Uppsala, Sweden. The primary proton fluence was estimated to be $\Phi = D/s = 5.5 \times 10^8\ \mathrm{cm}^{-2}$ from a dose measurement $D = 0.635$ Gy at 2 mm water depth with an electronic mass stopping power $s = 7.25\ \mathrm{MeV\ cm^2\ g^{-1}}$ at 100 MeV.

A reference depth-dose curve of the 100 MeV protons in the water phantom was measured with an ionization chamber (Roos, PTW Freiburg GmbH, Germany) which is used to validate the Monte Carlo model of the experimental setup. Two scintillators are introduced at a time in a hollow acrylic (PMMA) cylinder, see figure 1, carved to match the outer diameter of the ionization chamber in order to fit the same holder in the water phantom. The response curve of each scintillator in the water phantom was measured twice. The detector response from the water surface to 6.9 cm water depth was measured with 3 mm and 1 cm steps for the ionization chamber and scintillators, respectively. Both step sizes were 0.3 mm onwards.

2.1.1. Monte Carlo scoring of the dose and LET

A model of the experimental setup is implemented in `Geant4` (Agostinelli *et al* 2003) version 10.4.p02 using the `QGSP_INCLXX_EMZ` physics list. A beam model detailed in Almhagen *et al* (2018) was used, which was validated against measured dose distributions and thus has a demonstrated ability to recreate the nuclear halo. The `Geant4` model enables a scoring of the energy deposition and LET spectra for both primary and secondary particles at any point in the scintillator and ionization chamber during the experiments.

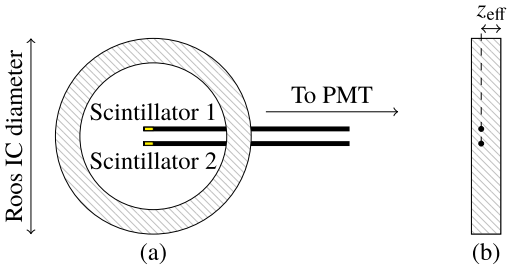

Figure 1. (a) The PMMA ring with an outer diameter matching the Roos chamber holder with the fiber-coupled scintillators connected to a photomultiplier tube (PMT). (b) Side view of the ring where the two holes are drilled at a distance z_{eff} corresponding to the effective point of measurement of the ionization chamber.

The LET is scored in `Geant4` as both LET_Φ and LET_D following the recommended definition in Cortés-Giraldo and Carabe (2015), where the LET in the latter case is extracted from the `Geant4` electronic stopping power tables. The dose and LET quantities are scored in voxels of side length 1 mm. The LET values in the tables and figures below are given as the LET in water. The stopping power ratios between water and the scintillating material in question are used to estimate the LET in the scintillator for quenching calculations.

The active volume in a scintillator causes an averaging of the sharp dose gradients at the pristine Bragg peak. The volume averaging is assessed through a Monte Carlo approach by scoring the dose and LET in cylinders placed along the beam axis with the cylinder axis perpendicular to the beam direction for different radii.

2.2. Quenching corrections

2.2.1. Semi-empirical quenching corrections

The luminescence $\mathrm{d}L$ per unit length $\mathrm{d}x$ of an ion incident on a scintillator with light yield per energy A will in the absence of ionization quenching equal the number of photons emitted per deposited energy, i.e. $N \equiv A \cdot \text{LET}$. However, the luminescence is reduced with the quenching correction factor (QCF) as

$$\frac{\mathrm{d}L}{\mathrm{d}x} = A\,\frac{\text{LET}}{\text{QCF}}, \qquad \text{for} \quad 1 \leqslant \text{QCF} = 1 + kB \cdot \text{LET} + C \cdot \text{LET}^2 + \cdots, \tag{2.1}$$

where kB and C are model parameters to be determined experimentally. The case $C = 0$ reduces equation (2.1) to the Birks model (Birks 1951) and $C \neq 0$ corresponds to the second-order model due to Chou (1952), which both typically rely on the LET_Φ.

2.2.2. Theoretical quenching corrections

Amorphous track structure models have historically been successfully applied to model the radial energy distribution. This work relies on the track structure model due to Scholz and Kraft (1996), as outlined in appendix A.1, to model the radial exciton density in ion tracks.

The exciton density $n(r, t)$ in an ion track is at $t = 0$ governed by the amorphous track structure model and changes in time and space according to the kinematic Blanc model (Blanc *et al* 1962, 1964)

$$\frac{\partial n}{\partial t} = D\nabla^2 n - \tau^{-1} n - \alpha n^2, \tag{2.2}$$

where D is the exciton diffusion constant, $\tau^{-1} = p + k$ is the decay time of the scintillator, and p, k, and α are the rate of fluorescence emission, uni-, and bimolecular quenching parameters, respectively. The solution to equation (2.2), subject to the initial condition given by the amorphous track structure model for a given ion and scintillator, is implemented in the open-source repository `ExcitonQuenching`[9]. The scintillator parameters τ and A are listed in table 1 whereas the Blanc model parameters are given in Christensen and Andersen (2018) along with a detailed model explanation. The light emission from the scintillator caused by an incident ion is calculated by integrating over the fluorescence term in equation (2.2), and the QCF is subsequently computed as the ratio of the light emission excluding quenching (i.e. with $\alpha = 0$) to the light emission including quenching ($\alpha \neq 0$).

2.2.3. Quenching corrections in a mixed radiation field

A primary or secondary ion i depositing a dose $D_i(x)$ at the depth x will in a quenching-free case for $\text{QCF} \simeq 1$ give rise to a fraction $w_i(x) = D_i(x)/D_{\text{total}}(x)$ of the luminescence signal, where $D_{\text{total}}(x)$ denotes the total dose

[9] Available for download at https://github.com/jbrage/ExcitonQuenching.

at the given depth. Nonetheless, when quenching is present, the light output for the ion i is reduced with a factor $\mathrm{QCF}_i > 1$, corresponding to a quenched luminescence signal as $w_i(x)/\mathrm{QCF}_i(x) < 1$. Consequently, a common correction factor $\mathrm{QCF}_{\mathrm{total}}$ for the total quenched luminescence signal is computed as

$$\frac{1}{\mathrm{QCF}_{\mathrm{total}}(x)} = \frac{1}{D_{\mathrm{total}}(x)} \sum_i \frac{D_i(x)}{\mathrm{QCF}_i(x)}, \tag{2.3}$$

where the summation runs over primary and secondary protons ions, deuterons, tritons, and two isotopes of helium. The Birks and Chou models are not directly applicable when equation (2.3) is inserted into equation (2.1) as the quenching parameters for both models vary for each type of ion and require experimental determinations. Thus, only `ExcitonQuenching` is applied as it accounts for the varying radial energy deposition through amorphous track structure theory. The `ExcitonQuenching` calculation of ionization quenching in ion tracks with atomic number $z \leqslant 6$ was validated in Christensen and Andersen (2019).

2.2.4. Comparison of quenching models

The quenching corrections for the three organic plastic scintillators are calculated with five approaches:

(A) With `ExcitonQuenching` for the case where only the luminescence from primary protons is considered, and the LET_Φ for primary protons is used to correct the quenching.
(B) Using `ExcitonQuenching` where the quenching from both primary and secondary ions are taken into account and the quenched signal is corrected with a common correction factor according to equation (2.3).
(C) By fitting the linear Birks model to the experimentally determined QCFs as a function of LET_Φ for primaries and secondary protons in line with other studies (Wang *et al* 2012, Hoehr *et al* 2018).
(D) By fitting the second-order Chou model to the QCFs as a function of LET_Φ for primaries and secondary protons directly in equation (2.1).
(E) With a convolution of the the Chou model and the proton LET spectrum, which gives a QCF as a function of depth as

$$\mathrm{QCF}(x) = 1 + kB \cdot \mathrm{LET}_\Phi(x) + C\left(\mathrm{LET}_\Phi{}^2(x) + \sigma^2(x)\right),$$

as derived in appendix A.2. I.e. the second-order term in Chou model is no longer a function of the fluence-averaged LET in equation (2.1) alone but perturbed by the variance of the LET spectrum.

Goodness of fit

The quality of the quenching corrected scintillator signal S_{scint} with variance $\sigma^2_{\mathrm{scint}}$, compared to the dose distribution measured with an ionization chamber S_{IC}, is evaluated through the χ^2 per degree of freedom (dof) as

$$\chi^2 = \sum_{i=0}^{n} \frac{\left(S_{\mathrm{IC},i} - S_{\mathrm{scint},i}\right)^2}{\sigma^2_{\mathrm{scint},i}}, \tag{2.4}$$

where the sum runs over all data points n in the scintillator measurement and the dof is given as n minus the number of model parameters.

2.2.5. Exciton interactions between ion tracks

Overlapping ion tracks is a well-known phenomenon in dosimetry where e.g. initial and general recombination in gas-filled ionization chambers exposed to ion beams requires different correction methods and has previously been investigated numerically (Christensen *et al* 2016). The situation is similar in scintillators, although the higher material density and rapid decay time of organic plastic scintillators limits the track interactions. The five quenching corrections in section 2.2.4 all rely on the implicit assumption that the quenching in ion tracks are independent of each other. `ExcitonQuenching` enables a zeroth-order approximation of a fluence threshold where the ion tracks will overlap on average and increase the quenching non-linearly, and limit the applicability of the Birks and Chou models.

3. Results

3.1. Model and LET spectrum verification

The dose measured with the ionization chamber is compared to the `Geant4` results in figure 2, where the dose distributions have not been subject to a peak match. The LET is scored from the entrance to the 80% distal dose point (Bortfeld 1997) as illustrated in the figure with a vertical dashed line. The lower figure shows the ratio of the simulated to the measured dose where the discrepancy is less than 2%. Two measurements of the BCF-12

scintillator are normalized to the entrance and indicate the ionization quenched response relative to the dose measurements as well as alignment errors, which both are to be corrected.

The LET spectrum for both primary and secondary protons are shown in figure 3(a). The LET_Φ as a function of depth, corresponding to the arithmetic mean of the spectrum, is shown with a white, dashed line. The LET spectrum at the entry channel is sharply defined but gradually smeared out as the primary protons undergo scattering processes in the water. Figure 3(b) shows the LET spectrum extracted at three depths from figure 3(a), where the tail contributions from secondary protons are clearly visible at the two shallower depths whereas the LET spectrum at the Bragg peak is wide.

The `Geant4` simulated dose and LET contributions from several ions during the experiments are presented in figure 4. Figure 4(a) shows the LET_Φ and LET_D from primary and secondary protons along with deuterons, tritons, ^{3}He, and alpha particles with their contributions to the total dose in figure 4(b). Although secondary protons only constitute up to 8% of the total dose, the LET for secondary protons at the entry channel is several times larger than that of the primaries. Isotopes of helium contribute around 0.3% of the total dose but with elevated LET of more than two orders of magnitude at the entry channel. The total contribution to the dose from secondary ions thus amounts to several percent throughout the beam with an uneven LET distribution, giving rise to a non-linear common quenching correction as a function of depth.

3.2. Scintillation response

The scintillator response as a function of depth varies from the ionization chamber measurement not only due to ionization quenching but is furthermore subject to both an alignment offset with the ionization chamber as well as a volume averaged signal.

3.2.1. Volume averaging

The effect of volume averaging of the dose and LET distributions is investigated in appendix A.3, where the dose and LET_Φ are scored in 0.1 mm, 1 mm, and 3 mm volumes in `Geant4`. The deviation between the dose and LET_Φ scored in 1 mm wide voxels to the same quantities scored in 0.1 mm wide voxels is less than 2% and as such in agreement with the results in Archambault *et al* (2008). The 2% deviation for the 1 mm diameter scintillators is within the experimental uncertainties at the Bragg peak.

3.2.2. Scintillator alignment errors

The positioning of the scintillators in the holder is corrected for any misalignment in line with the approach suggested in Wang *et al* (2012): the QCFs are for a given depth shift of the scintillator measurement calculated as the ratio between the measured dose and the quenched scintillator signal. The linear Birks model is then fitted to the data as a function of LET_Φ and the quality of the particular shift is evaluated through χ^2/dof between the model and the experimentally determined QCFs. The best fit is found by interpolation as the shift minimizing χ^2/dof.

A similar approach was applied for method (D) with the Chou model, where the χ^2/dof was calculated after fitting a second-order function to the QCFs, to avoid comparing the quality of the quadratic Chou model to data shifted according to the linear Birks model. The scintillator shift corrections obtained for the Chou model in method (D) were applied to method (E) in order to compare the LET_Φ and spectrum corrected quenched luminescence. All scintillator measurements were shift corrected less than 1 mm, and the two measurements for each scintillator were subsequently concatenated into a single scintillator response curve.

3.3. Quenching corrections models

The experimentally determined QCFs as a function of LET_Φ for the BCF-12 scintillator are shown in figure 5, where the data were shifted according to the Birks model. The QCFs are calculated with `ExcitonQuenching` using methods (A), where only the LET_Φ from the primary protons in figure 3 is taking into account, and (B) which includes the six ions in figure 4 and calculates a common QCF as given by equation (2.3). Method (C) with the Birks model is fitted to the experimentally obtained QCFs with quenching parameter *kB* listed in table 1. The agreement between the models in figure 4 is representative for the results obtained for the BCF-60 and 81–81004 scintillators.

3.3.1. Mixed field quenching

The dose-weighted QCF_{total} for the relevant ions are calculated with `ExcitonQuenching` in approach (B) for the BCF-12 scintillator in figure 6. Secondary protons contribute 5% of the luminescence signal at 3 cm depth although the dose contribution is 8%, while the primary protons give rise to 95.4%–99.8% of the luminescence signal along the central beam axis. Constant quenching corrections along the beam axis, as the case approximately is for the alpha particles, are negligible for relative scintillator measurements.

Table 1. Comparison of quenching corrected scintillator measurements through χ^2/dof for the five methods (A)–(E). The light yield and decay time for the BCF scintillators are given by the manufacturer (Saint-Gobain, France). The fitted Birks and Chou quenching parameters kB and C in equation (2.1) are listed for the three scintillators for methods (C) and (D) with ($k = 2$) uncertainties. The quenching parameters are not included for method (E) as it is not a function of LET_Φ alone.

	Methods (A) and (B), `ExcitonQuenching`				Method (C), Birks	
Scintillator	Light yield (% Anthracene)	τ (ns)	χ^2/dof (A) primaries	χ^2/dof (B) all	kB (μm keV^{-1})	χ^2/dof
BCF-12	46	3.2	0.72	0.70	0.107 ± 0.003	0.66
BCF-60	41	7.1	1.33	1.26	0.103 ± 0.004	1.12
81-0084[a]	—	—	—	—	0.106 ± 0.001	0.26

	Method (D), Chou (LET_Φ)			Method (E), Chou (LET-spectrum)
Scintillator	C (μm^2 keV^{-2})	kB (μm keV^{-1})	χ^2/dof	χ^2/dof
BCF-12	0.007 ± 0.002	0.056 ± 0.009	1.08	1.01
BCF-60	0.004 ± 0.003	0.078 ± 0.010	1.21	1.20
81-0084	0	0.106 ± 0.001	0.27	0.27

[a] The light yield was unavailable and `ExcitonQuenching` as such not applicable.

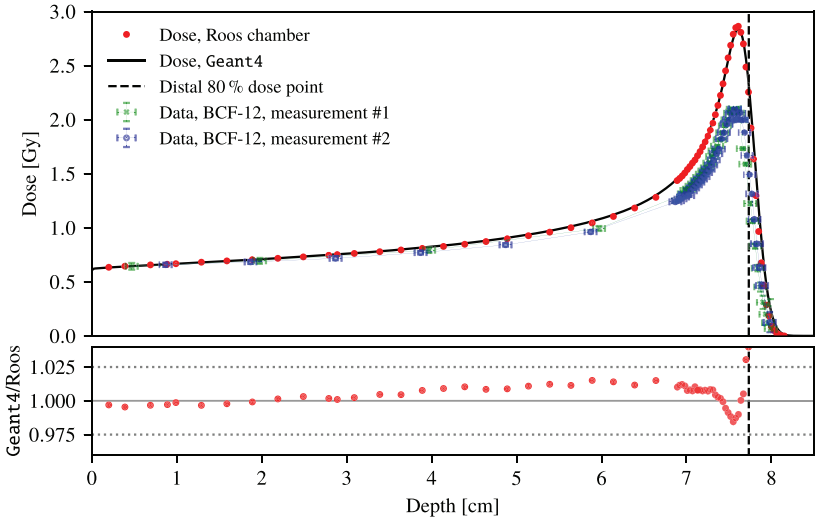

Figure 2. Comparison of the dose measured with an ionization chamber (dots) and scored in the `Geant4` model (solid line) in the water phantom. The ratio between the simulated and measured dose is shown below. The 80% distal dose threshold is delineated with a vertical, dashed line. The two measurements with the BCF-12 scintillators are shown with $k = 2$ statistical uncertainties for reference .

3.3.2. Quenching corrections

Each of the three quenched scintillator responses is corrected with the five quenching correction methods (A)–(E) and compared to the ionization chamber measurement resulting in the χ^2/dof values listed in table 1. The quenching corrected luminescence signal is compared to the dose measurement in figure 7 for methods (A), (C), and (E), where the corrected signals using methods (B) and (D) are omitted for the sake of clarity.

The discrepancies between the corrected scintillator signals and the dose measurement exhibit similar structures. The deviations from the dose measurements are for the entry channel around 2.5% for the BCF-scintillators and less than 1% for the 81-0084 scintillator. The deviation at the Bragg peak is for the BCF-12 scintillator within 5% except for an outlier, whereas the BCF-60 and 81-0084 scintillators both exhibit discrepancies as much as 10%.

3.4. Quenching thresholds

The quenching fluence threshold is computed by sampling ion tracks to resemble different fluences. The quenching between two parallel 100 MeV proton tracks in the BCF-12 scintillator is investigated in figure 8, where the spatial distance between the two tracks is shown on the abscissa, and the ordinate shows the time between the

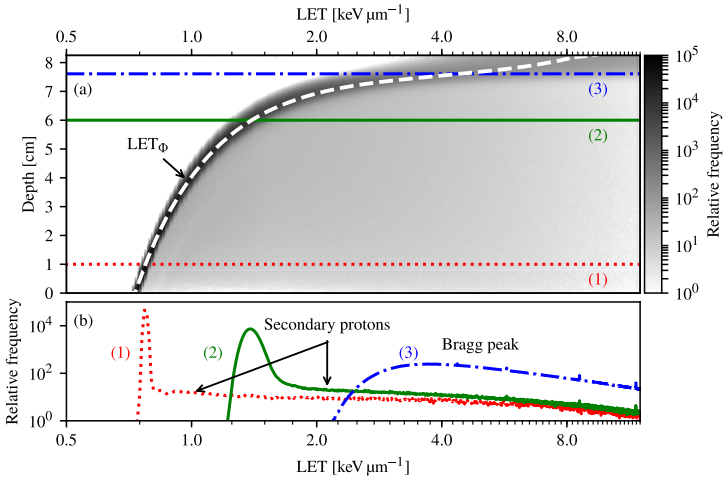

Figure 3. (a) Geant4 calculations of the LET spectrum for primary and secondary protons. The arithmetic mean, the LET_Φ, is delineated with a dashed, white line. The LET distributions at the three depths (1) 1 cm (dotted line), (2) 6 cm (solid line), and (3) the Bragg peak at 7.61 cm (dot-dashed line) are shown in (b). The mean and 1 standard deviation for the three non-normal distributions are (1) (0.780 ± 0.058) keV μm^{-1}, (2) (1.48 ± 0.42) keV μm^{-1}, and (3) (6.07 ± 2.90) keV μm^{-1}.

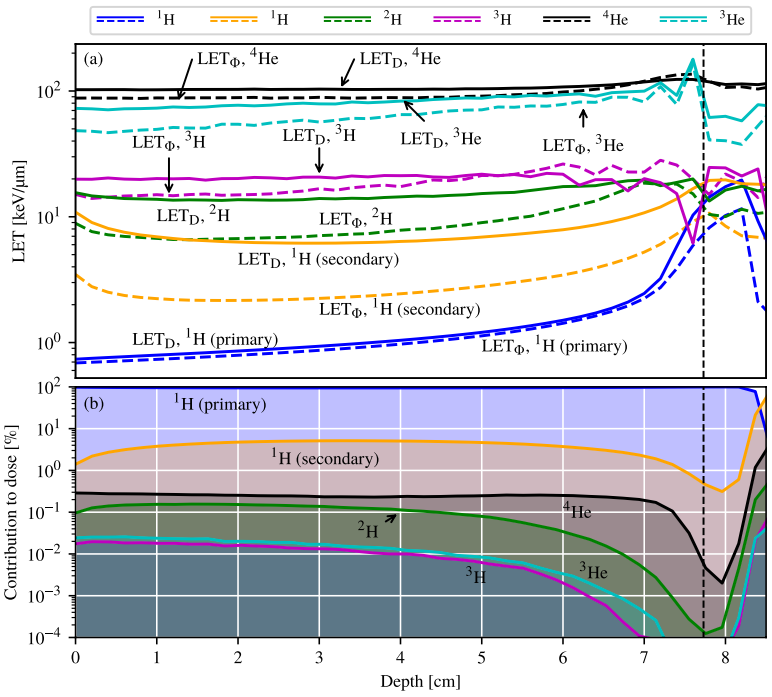

Figure 4. (a) LET distributions for primary and secondary protons, deuterons, tritons, ^{3}He, and alpha particles. The LET_Φ is plotted with dashed lines and the LET_D with solid lines. (b) The dose distributions of the six ions contributing the most to the dose deposition. The dashed vertical lines indicates the distal 80% dose threshold.

two protons. The QCF map is calculated by interpolating the QCF results of 5000 uniformly log-sampled points where only a fraction of the samples is shown in the figure. The fluence is approximated as the inverse of the square of the distance between the proton tracks. The QCF = 1.056 for a single ion track for the given proton energy and scintillator, and such a value in the QCF map corresponds to the case, where the quenching in the ion

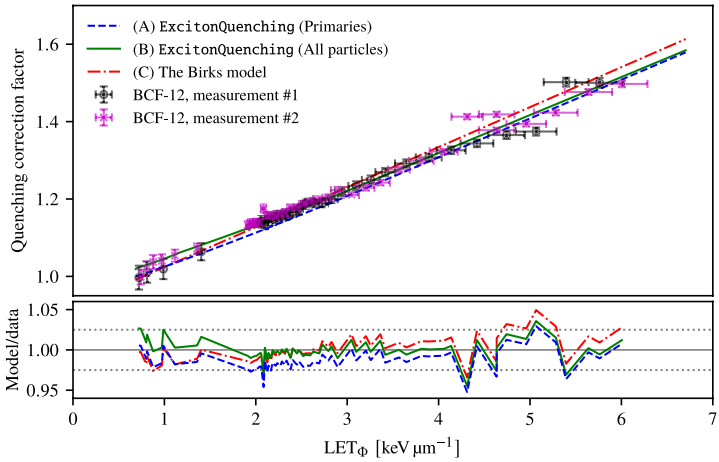

Figure 5. The experimentally obtained QCFs for the two BCF-12 measurements where the linear Birks model is fitted to the data. The QCFs are computed with `ExcitonQuenching` using methods (A) and (B). The ratios between the model-predicted to the experimentally determined QCF is shown below with the same line styles as given in the legend above.

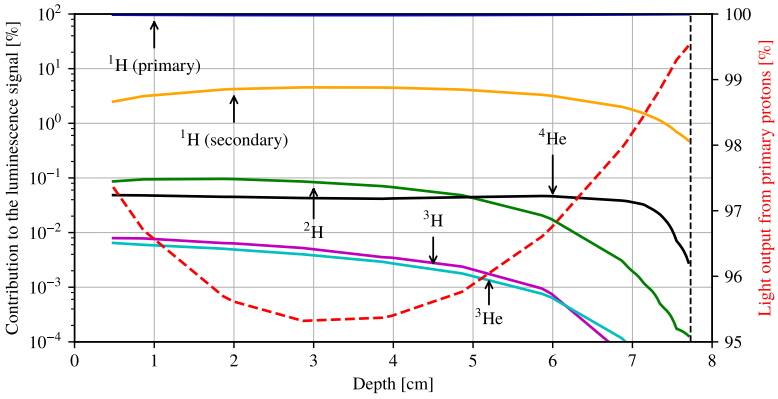

Figure 6. The percentage of the total luminescence signal for each of the included ions (solid lines) plotted on the left ordinate as predicted by equation (2.3) for the BCF-12 scintillator. The right ordinate shows the percentage of the luminescence signal caused by primary protons plotted with a dashed line. The distal 80% dose point is marked with a vertical, dashed line.

tracks are independent of each other. The horizontal, dashed line in the figure is the characteristic decay time of the scintillator, whereas the dashed, vertical line is the distance corresponding to twice the ion core radius in the Scholz–Kraft model in appendix A.1.

4. Discussion

4.1. Monte Carlo calculations

4.1.1. `Geant4` model validation

The agreement between the `Geant4` calculated dose and the ionization chamber measurements in figure 2 confirms the application of the `Geant4` model to calculate the LET and dose distributions in figures 3 and 4. Furthermore, the dose and LET scoring variations due to volume averaging in appendix A.3 are not corrected as the LET variations are below 2%, i.e. well below the experimental uncertainties.

4.1.2. Proton LET spectrum

The LET spectrum of primary and secondary protons in figure 3(a) exhibits a relative sharp fluence distribution at the entry channel as exemplified in figure 3(b) at the three depths. As the LET spectrum is sharp at the entry

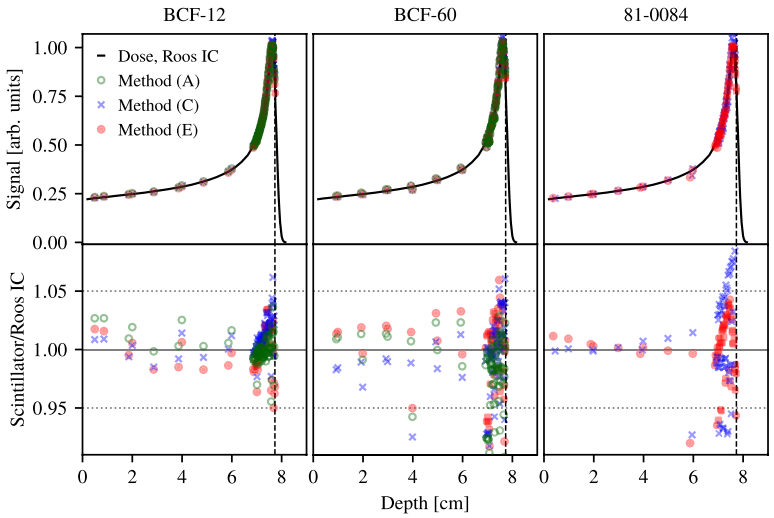

Figure 7. The quenched scintillator signal corrected with method (A), where `ExcitonQuenching` relies on the primary protons shown with open circles, method (C) with the Birks model plotted with crosses, and (E) the Chou model, shown with circles, taking the full proton spectrum into account. The ionization chamber measurement is plotted with a solid line. The lower figures show the ratio between each quenching corrected scintillator signal to the ionization chamber measurement where the dotted horizontal lines denote 5% discrepancies. The χ^2/dof for each method is given in table 1.

channel $\mathrm{LET}_\Phi{}^2 + \sigma^2 \approx \mathrm{LET}_\Phi{}^2$, i.e. equation (A.3*b*) reduces to the normal Chou model as a function of LET_Φ in equation (2.1) without the variance dependency. As such, the convolution of the Chou model and the LET spectrum in equation (A.3*b*) is redundant. The situation differs at the Bragg peak where $\mathrm{LET}_\Phi{}^2/\sigma^2 \simeq 4.4$ and the error on the second-order term in equation (A.3*b*) increases correspondingly if the variance of the LET spectrum is omitted. This shows, that the LET spectrum cannot be neglected at the Bragg peak for the Chou model, which is similar to the LET_D discussions and conclusion in Grün *et al* (2018).

4.2. Scintillator quenching

4.2.1. Quenching correction factors

The experimentally determined QCFs in figure 5 deviates 3% below 4 keV $\mu\mathrm{m}^{-1}$ for methods (A)–(C) except for an outlier. The quenching correction parameter *kB* in table 1 for the BCF-12 scintillator deviates 10% and 3% from the results published in Wang *et al* (2012) and Alsanea *et al* (2018), respectively. The *kB* value for the BCF-60 scintillator is between the two values reported by Hoehr *et al* (2018). The Chou model in method (D) provided the best fit to the data for $C \neq 0$ for the BCF scintillators, in agreement with (Torrisi 2000), and $C = 0$ for the 81-0084 scintillator in agreement with (Birks 1964). The quenching parameters *kB* and *C* were not extracted for method (E) since the QCFs are obtained as a function of depth rather than LET_Φ as the latter is perturbed by the variance of the LET spectrum.

4.2.2. Energy deposition by secondary, heavy ions

The contributions from deuterons, tritons, and helium isotopes constitute around 0.3% of the total dose, except for the dip at the Bragg peak with LETs ranging from 1 to 2 orders of magnitude larger than that of the primaries. The huge LETs combined with slow velocities lead to dense track structures with an enormous local energy deposition and thus ionization quenching. Consequently, the particles heavier than a proton will due to a low dose contribution give rise to a negligible quenching correction in proton beams as shown in figure 6 and equation (2.3). For relative measurements, the inclusion of the heavy secondary ions is negligible, as they contribute almost uniformly to the dose along the beam axis. However, if the light yield of the scintillator is to be calculated from the scintillator measurements as in Alsanea *et al* (2018), the quenched light emission from secondary protons needs to be considered and corrected, while the heavier secondary ions would give rise to less than a 1% luminescence correction. The situation is however different in heavy ion beams where the dose contribution from secondary, heavy ions is significantly larger and needs to be corrected. However, the elevated LET in the plateau region of a heavy ion beam would reduce the experimental uncertainties inevitable related

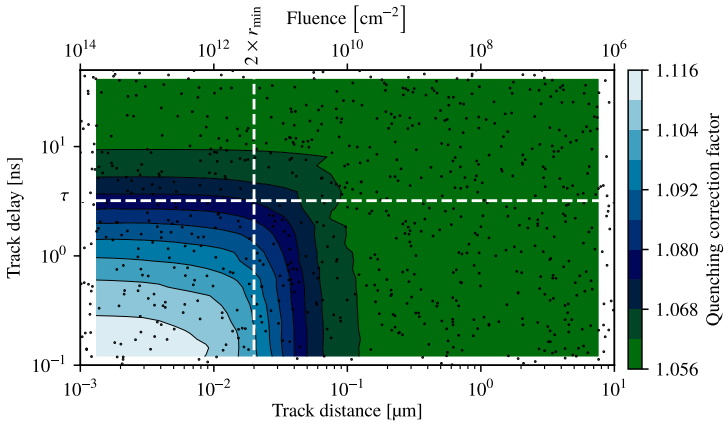

Figure 8. The QCF map for two 100 MeV proton tracks computed with `ExcitonQuenching` in the BCF-12 scintillator. The spatial distance between the two ion track centres is shown on the abscissa and the time between the two ions on the ordinate. The horizontal dashed line corresponds to the characteristic decay time of the scintillator τ whereas the vertical dashed line is twice the ion core radius r_{min}.

to measurements at the Bragg peak in a proton beam, and thus improve the possibilities for relating ionization quenching to LET and track structure theory.

The dose contribution from secondary protons is uneven and constitutes up to 8% of the total dose while the LET at the entry channel is comparable to the LET of the primaries at the Bragg peak. Thus, the secondary protons contribute unevenly to the quenching along the beam axis, which is reflected in the better fit for `ExcitonQuenching` method (B) than (A) in table 1, where the former method corrects the quenched signal from all particles.

4.2.3. Quenching models

The quenching corrected signals in figure 7 all exhibit a similar structure with a deviation around 2% from the entrance region to 6 cm depth with an increasing discrepancy to 5% for the BCF-12 scintillator and 9% for the BCF-60 and 81-0084 scintillators. The Birks model in method (C) gave the overall lowest χ^2/dof in table 1. A direct χ^2/dof comparison across the methods is however difficult as the data for the Birks and Chou models were shifted differently. The Birks model method (C) performs well for quenching corrections in proton beams due to its linearity; the convolution of the LET spectrum and the linear model yields exactly the LET_Φ see equation (A.4), and the Birks model, correcting the quenching with the LET_Φ and not LET_D, as such automatically incorporates the full proton LET spectrum. This is in contrast to the Chou model method (E) which relies on the variance of the LET spectrum rather than the arithmetic mean alone.

The inclusion of the secondary ions with `ExcitonQuenching` in method (B) gives a slightly better quenching correction than method (A) with primaries alone. However, the Birks model gives overall better corrections than `ExcitonQuenching`: the scintillation measurement data are shifted to match the Birks or the Chou quenching model, which furthermore are fitted directly to the data, i.e. a better fit from the Birks and Chou models are expected. As `ExcitonQuenching` relies on amorphous track structure and a kinematic model, the derived QCFs are general calculations rather than fits to the particular set of data. A drawback with `ExcitonQuenching` is observed for the 81-0084 scintillator, where the method could not be applied as the light yield of the scintillator is unavailable.

4.3. Fluence thresholds for quenching

The map of the QCF for two proton tracks separated at different distances and times in figure 8 shows a region where QCF > 1.056, i.e. where the excitons in the ion tracks interact significantly. The zeroth-order approximation enables an estimation of a fluence threshold for 100 MeV protons of $\Phi_{TH} = 10^{10}$ cm^{-2}, corresponding to 110 Gy, at which two proton tracks overlap sufficiently to modify the quenching. However, multiple tracks will overlap during an irradiation (Greilich *et al* 2014) and even the exciton density in the penumbras may consequently lead to substantial quenching, increasing non-linearly with the numbers of overlap. The QCF map indicates that two proton tracks should interact within 10 ns, corresponding to $\approx 3\tau$, for mutual quenching to occur. Such a pulse length is relevant for cyclotrons, where the quenching depends on the cyclotron frequency, in particular for high dose-rates. The fluence of the proton beam during the experiments

was thus more than an order of magnitude smaller than Φ_{TH}, which justifies the application of the quenching models, all relying on the quenching in ion tracks being independent of each other.

5. Conclusions

The differences between the LET-averaging and the LET spectrum on the quenched luminescence signal were investigated with three quenching models and three plastic scintillators. The open-source code `ExcitonQuenching` was applied to investigate how the heavy ion fragments in the proton beam affects the quenching and hence the luminescence during proton irradiation. The `ExcitonQuenching` results show, that while the primary protons constitute 92%–99% of the dose, the elevated LET of the secondary ions quenches the light emission in the secondary ion tracks more than the primary protons. Thus, the primary protons constitute more than 95% of the luminescence signal at the entry channel and close to 100% at the Bragg peak. The dose contribution from heavy secondary ions is too low in proton beams to require a quenching correction, but would be necessary to include for beams of heavier ions.

The quality of the five quenching correction methods were examined through χ^2/dof, accounting for the number of free model parameters. The results show that the Birks model, relying on the fluence-averaged LET, provides the best fit to the data as it includes the full proton LET spectrum due to its linearity. This is in contrast to the Chou method with an additional model parameter which depends on the both the mean and variance of the proton LET spectrum due to its non-linearity: the LET_Φ is much larger than the variance of the LET spectrum at the entry channel, and as such a good predictor for the quenching, but the large variance around the distal edge requires the inclusion of the spectrum at such a depth. The Chou model is not relevant for proton beams as its extra parameter relative to the Birks model is negligible, while the quenching correction factors are perturbed by the variance of the LET spectrum at the Bragg peak.

The volume averaging of a 1 mm diameter scintillator is numerically shown to give rise to a deviation less than 2% for the dose and LET_Φ calculations provided the analysis is truncated at the 80% distal dose point. The interactions between excitons from different tracks were investigated by varying both the distance between two ion tracks in an organic scintillator as well as the time between them. This led to an estimation of a fluence threshold of 10^{10} cm^{-2} for pulses of the order of 10 ns, where the quenching increases greatly, and above which the Birks model no longer is applicable.

Acknowledgments

The work was supported by the Danish Cancer Society and the Danish Council for Independent Research (grant FTP, DFF—4184-00151).

Appendix

A.1. Amorphous track structure model

The Scholz–Kraft track structure model consists of penumbral and core radii defined as

$$r_{max} = 0.05\,E^{1.7}\ \mu\mathrm{m}, \qquad r_{min} = 0.01\ \mu\mathrm{m},$$

respectively, where E (MeV/nucleon) is the kinetic energy of the projectile and the radii are scaled according to the density of the medium. The model governs an initial radial exciton density n of

$$n(r) = \begin{cases} \dfrac{C}{r_{min}^2} & \text{for} \quad r < r_{min} \\ \dfrac{C}{r^2} & \text{for} \quad r_{min} \leqslant r \leqslant r_{max} \\ 0 & \text{for} \quad r > r_{max} \end{cases}, \qquad \text{for} \quad C = A \cdot \mathrm{LET}\left(\pi\left[1 + 2\ln\frac{r_{max}}{r_{min}}\right]\right)^{-1}, \tag{A.1}$$

where A is the light yield.

A.2. LET spectrum quenching models

Let $\varphi(s,x)$ be the normalised intensity of the LET denoted with s at a depth x. The arithmetic mean (i.e. LET_Φ) and variance σ^2 of the spectrum at any depth is conventionally given as

$$\mathrm{LET}_\Phi(x) = \int_0^\infty s\,\varphi(s,x)\,\mathrm{d}s, \qquad \sigma^2(x) = \int_0^\infty s^2\,\varphi(s,x)\,\mathrm{d}s - \mathrm{LET}_\Phi{}^2(x), \tag{A.2}$$

respectively. Consequently, the convolution of the Chou model in equation (2.1) and the LET spectrum as a function of depth yields a QCF as a function of depth as

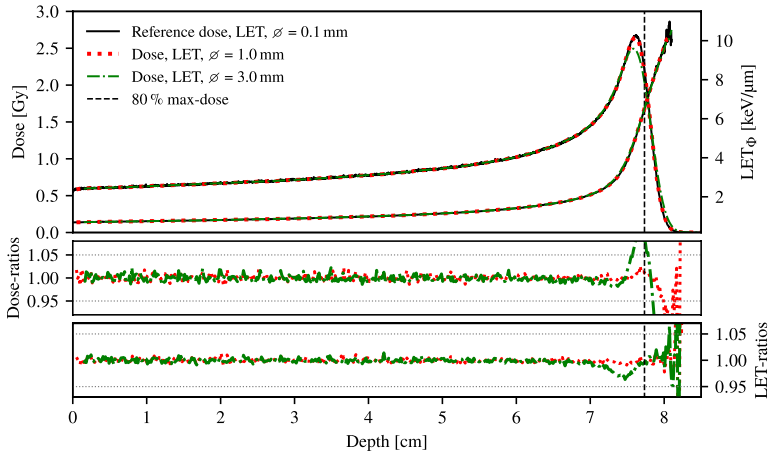

Figure A1. Geant4 calculations of dose and LET_Φ scored in volumes of different size. The reference dose is scored in 0.1 mm wide voxels. The ratios between the dose and LET_Φ scored in 1 mm and 3 mm diameter voxels to the reference calculations are shown in the two lower figures.

$$\mathrm{QCF}(x) = \int_0^\infty \left(1 + kB \cdot s + C \cdot s^2\right) \varphi(s,x)\, \mathrm{d}s \tag{A.3a}$$

$$= 1 + kB \cdot \mathrm{LET}_\Phi(x) + C\left(\sigma^2(x) + \mathrm{LET}_\Phi{}^2(x)\right) \tag{A.3b}$$

whereas the Birks model due to its linearity is unchanged as

$$\mathrm{QCF}(x) = \int_0^\infty (1 + kB \cdot s)\ \varphi(s,x)\, \mathrm{d}s = 1 + kB \cdot \mathrm{LET}_\Phi(x). \tag{A.4}$$

A.3. Volume averaging

The dose and LET_Φ scored in volumes of different diameter in Geant4 are shown in figure A1. The 1 mm diameter scoring yields differences smaller than 2% shallower than the 80% distal dose point.

ORCID iDs

Jeppe Brage Christensen https://orcid.org/0000-0002-6894-381X
Liliana Stolarczyk https://orcid.org/0000-0002-6333-3350
Anne Vestergaard https://orcid.org/0000-0003-1398-6377
Niels Bassler https://orcid.org/0000-0002-4160-1078
Claus E Andersen https://orcid.org/0000-0002-7356-9607

References

Agostinelli S *et al* 2003 GEANT4—a simulation toolkit *Nucl. Instrum. Methods* **506** 250–303
Almhagen E, Boersma D J, Nyström H and Ahnesjö A 2018 A beam model for focused proton pencil beams *Phys. Med.* **52** 27–32
Alsanea F, Therriault-Proulx F, Sawakuchi G and Beddar S 2018 A real-time method to simultaneously measure linear energy transfer and dose for proton therapy using organic scintillators *Med. Phys.* **45** 1782–9
Andersen C E 2011 Fiber-coupled luminescence dosimetry in therapeutic and diagnostic radiology *Concepts Trends Med. Radiat. Dosim.* **1345** 100–19
Archambault L, Polf J C, Beaulieu L and Beddar S 2008 Characterizing the response of miniature scintillation detectors when irradiated with proton beams *Phys. Med. Biol.* **53** 1865–76
Beddar A S, Mackie T R and Attix F H 1992a Water-equivalent plastic scintillation detectors for high-energy beam dosimetry: I. Physical characteristics and theoretical considerations *Phys. Med. Biol.* **37** 1883–900
Beddar A S, Mackie T R and Attix F H 1992b Water-equivalent plastic scintillation detectors for high-energy beam dosimetry: II. Properties and measurements *Phys. Med. Biol.* **37** 1901–13
Birks J B 1951 Scintillation from organic crystals: specific fluorescence and relative response to different radiation *Proc. Phys. Soc.* A **64** 874–7
Birks J B 1964 The Theory and Practice of Scintillation Counting: International Series of Monographs in Electronics and Instrumentation vol 27 (Amsterdam: Elsevier)

Blanc D, Cambou F and de Lafond Y G 1962 Kinetics of the fast component of scintillation in a pure organic medium. Application to anthracene *C. R. Acad. Sci., Paris* **18** 3187–9
Blanc D, Cambou F and de Lafond Y G 1964 Etude cinétique de la scintillation dans les cristaux organiques purs *J. Phys.* **25** 319–25
Boivin J, Beddar S, Bonde C, Schmidt D, Culberson W, Guillemette M and Beaulieu L 2016 A systematic characterization of the low-energy photon response of plastic scintillation detectors *Phys. Med. Biol.* **61** 5569–86
Bortfeld T 1997 An analytical approximation of the Bragg curve for therapeutic proton beams *Med. Phys.* **24** 2024–33
Chou C N 1952 The nature of the saturation effect of fluorescent scintillators *Phys. Rev. Lett.* **5** 904–5
Christensen J B and Andersen C E 2018 Relating ionization quenching in organic plastic scintillators to basic material properties by modelling excitation density transport and amorphous track structure during proton irradiation *Phys. Med. Biol.* **63** 195010
Christensen J B and Andersen C E 2019 Applications of amorphous track structure models for correction of ionization quenching in organic scintillators exposed to ion beams *Rad. Meas.* accepted (https://doi.org/10.1016/j.radmeas.2019.01.003)
Christensen J B, Tölli H and Bassler N 2016 A general algorithm for calculation of recombination losses in ionization chambers exposed to ion beams *Med. Phys.* **43** 5484–92
Cortés-Giraldo M A and Carabe A 2015 A critical study of different Monte Carlo scoring methods of dose average linear-energy-transfer maps calculated in voxelized geometries irradiated with clinical proton beams *Phys. Med. Biol.* **60** 2645–69
Grassberger C and Paganetti H 2011 Elevated LET components in clinical proton beams *Phys. Med. Biol.* **56** 6677–91
Greilich S, Hahn U, Kiderlen M, Andersen C E and Bassler N 2014 Efficient calculation of local dose distributions for response modeling in proton and heavier ion beams *Euro. Phys. J.* D **68** 4
Grün R, Friedrich T, Traneus E and Scholz M 2018 Is the dose-averaged LET a reliable predictor for the relative biological effectiveness? *Med. Phys.* **46** 1064–74
Grzanka L, Ardenfors O and Bassler N 2018 Monte Carlo simulations of spatial LET distributions in clinical proton beams *Rad. Prot. Dosim.* **180** 296–9
Hoehr C, Lindsay C, Beaudry J, Penner C, Strgar V, Lee R and Duzenli C 2018 Characterization of the exradin W1 plastic scintillation detector for small field applications in proton therapy *Phys. Med. Biol.* **63** 095016
Murray R and Meyer A 1961 Scintillation response of activated inorganic crystals to various charged particles *Phys. Rev.* **122** 815
Paganetti H 2002 Nuclear interactions in proton therapy: dose and relative biological effect distributions originating from primary and secondary particles *Phys. Med. Biol.* **47** 747–64
Scholz M and Kraft G 1996 Track structure and the calculation of biological effects of heavy charged particles *Adv. Space Res.* **18** 5–14
Torrisi L 2000 Plastic scintillator investigations for relative dosimetry in proton-therapy *Nucl. Instrum. Methods Phys. Res.* **170** 523–30
Wang L L, Perles L A, Archambault L, Sahoo N, Mirkovic D and Beddar S 2012 Determination of the quenching correction factors for plastic scintillation detectors in therapeutic high-energy proton beams *Phys. Med. Biol.* **57** 7767–81

Paper V

Title:

Mapping of initial and general recombination in scanning proton beams

Authors:

Christensen JB, Almhagen E, Stolarczyk L, Liszka M, Hernandez GG, Nørrevang O and Vestergaard A

Status:

To be submitted to Medical Physics

Mapping initial and general recombination in scanning proton pencil beams

Jeppe Brage Christensen[1], Erik Almhagen[2,3], Liliana Stolarczyk[2,4], Małgorzata Liszka[4], Guillermo Garrido Hernandez[5], Ole Nørrevang[6], Anne Vestergaard[6],

[1]Center for Nuclear Technologies, Technical University of Denmark, Roskilde, Denmark
[2]Skandionkliniken, Uppsala, Sweden
[3]Medical Radiation Sciences, Department of Immunology, Genetics and Pathology, Uppsala University, Uppsala, Sweden
[4]Institute of Nuclear Physics Polish Academy of Sciences in Krakow, The Bronowice Cyclotron Centre, Krakow, Poland
[5]Department of Physics and Astronomy, Aarhus University, Aarhus, Denmark
[6]Danish Center for Particle Therapy, Aarhus University Hospital, Aarhus, Denmark

jepb@dtu.dk

August 14, 2019

Abstract

The ion recombination is examined in parallel-plate ionization chambers in scanning proton beams at the Danish Centre for Particle Therapy and the Skandion Clinic. The recombination correction factor k_s is investigated for clinically relevant energies between 70 MeV and 244 MeV for dose-rates below 900 Gy min^{-1} in air. The Boutillon formalism is used to separate the initial and general recombination. The general recombination is compared to predictions from the numerical recombination software `IonTracks` and the initial recombination to the Jaffé theory. k_s is furthermore calculated with the two-voltage method (TVM) and extrapolation approaches. The TVM is in agreement with the Boutillon method and `IonTracks` for dose-rates above $\dot{D}_0 \approx 100$ Gy min^{-1}. However, the TVM calculated k_s is closer related to the Jaffé theory for initial recombination below $\dot{D}_0$, indicating limitations in scanning light ion beams. The recombination is mapped as a function of the dose-rate and proton energy at the two centres using the Boutillon formalism: the initial recombination parameter was found to be $A = (0.12 \pm 0.2)$ V at DCPT and $A = (0.11 \pm 0.2)$ V at Skandion which is larger than the Jaffé theory for initial recombination but lower than previously reported values. The general recombination parameter was estimated to $m^2 = (3.4 \pm 0.7) \cdot 10^3$ V^2 nA^{-1} cm^{-1} and $m^2 = (2.8 \pm 0.4) \cdot 10^3$ V^2 nA^{-1} cm^{-1}.

Keywords: Initial recombination, general recombination, scanned proton beams

V.1 Introduction

Gas-filled ionization chambers (ICs) retain the position as the recommended detector for photon, electron, and ion beams in protocols as the IAEA TRS-398 (Andreo et al. 2000) and AAPM TG-51 (Almond et al. 1999). ICs are attractive for both reference dosimetry and daily quality assurance (QA) but the charge collection efficiency remains an issue. The charge liberated between the electrodes is drifting towards the electrode of opposite polarity with a possibility of recombining with other charge carriers: the probability for two charge carriers to recombine depends on several factors but varies enormously with the center of mass energy between the charge carriers. Hence, the recombination cross sections are currently insufficient for Monte Carlo methods to be applied for recombination corrections in ICs.

The ion recombination is traditionally divided into two categories: the recombination between charge carriers liberated from the same particle (initial recombination) or the recombination between charge carriers from different particles (general or volume recombination). The former case depends strongly on the linear energy transfer (LET) and the ion track structure whereas the latter is more closely related to the dose-rate.

The initial recombination in parallel-plate ICs irradiated with ion beams was treated theoretically by Jaffé 1913, 1929 and extensively experimentally confirmed in light and heavy ion beams (Kanai et al. 1998; Rossomme, Hopfgartner, et al. 2016; Liszka et al. 2018). The Jaffé theory for initial recombination in an ion track was generalized numerically in the open-source code `IonTracks` (Christensen, Tölli, and Bassler 2016) to include the interaction between multiple ion tracks and thus to account for both initial and general recombination.

The general recombination was for several decades mainly studied in photon and electron beams and theories were developed accordingly for uniform charge carrier distributions and low-LET beams without initial recombination (Thomson 1899; Mie 1904; Boag 1950; Greening 1964). Boag and Currant 1980 developed the foundation for the widely applied two-voltage method (TVM) which is recommended by IAEA TRS-398 and AAPM TG-51 among other protocols to correct the recombination in clinically relevant beams. The model was later extended to include a free-electron component (Boag, Hochhäuser, and Balk 1996), which reduces the ion recombination, as the electrons are almost immediately collected. Rossomme, Horn, et al. 2017 observed that the TVM is not applicable to scanned light-ion beams in cases where the initial recombination cannot be neglected.

The recombination in a gas-filled parallel-plate IC is in the present work investigated experimentally at the Skandion Clinic (Uppsala, Sweden) and the Danish Centre for Particle Therapy (DCPT, Aarhus, Denmark) with Roos-type chambers.

The initial and general recombination is separated using the approach developed by Boutillon 1998 and extended by Palmans, Thomas, and Kacperek

2006. Monte Carlo models of each beam line is used to extract the LET along the central beam axis for all experiments, which is used to model the initial recombination with the Jaffé theory and `IonTracks`. Furthermore, the Monte Carlo models are used to estimate an effective dose-rate of the spot-scanning proton beams as suggested by Liszka et al. 2018. The IC is irradiated with protons at different energies and dose-rates in order to map the recombination as a function of dose-rate and perform an inter-comparison between the two proton therapy centres.

The mapping of the ion recombination as a function of proton energy and dose-rate enables an estimate of a lower dose-rate threshold, where initial recombination dominates, and the TVM is no longer applicable for daily QA. Furthermore, the mapping enables the prediction and correction of the recombination in spread out Bragg peaks.

V.2 Materials and Methods

V.2.1 Experimental setup and Monte Carlo

The recombination was measured at The Skandion Clinic and the DCPT with the same Roos-type IC irradiated in 10 cm × 10 cm fields consisting of 41 × 41 spots at 2 cm reference depth in water. The IC was irradiated three times for each dose-rate at each of the polarization voltages 50 V, 67 V, 83 V, 125 V, and 200 V to avoid charge multiplication at higher voltages. The ion collection time in the IC varied between 0.12 ms (at 200 V) and 0.5 ms (at 50 V).

The dose deposited for a given energy and number of Monitor Units (MUs) is measured with the IC and related to the energy deposition per proton through a Monte Carlo model of each beam line. The spot deposition time was for each beam structure extracted from the log files. The dose, spot deposition time, and beam configuration were converted into an effective dose-rate following the procedure given in Liszka et al. 2018. The LET is scored as the fluence-averaged LET (LET_Φ) following the recommendations of Cortés-Giraldo and Carabe 2015.

Measurements at the Skandion Clinic

The Roos-type IC was irradiated with 70 MeV, 150 MeV, and 226 MeV protons corresponding to the available energy range of the Proteus-235 cyclotron (IBA, Belgium). The cyclotron delivers the pulses with 106 MHz and the spot duration varied between 3 ms at 226 MeV and 20 ms an 70 MeV. The beam is treated as a continuous beam as the spot duration is much longer than the charge collection time in the IC which in turn is longer than the pulse length.

The Proteus-235 cyclotron system tries to optimize the beam delivery time, and the dose-rate is varied by increasing the number of MUs per spot. The dose-rate or beam current does not increase linearly with the number of MUs

per spot and is moreover limited by the maximum available beam current The recombination was investigated for each of the three energies for 0.08 MU/spot, 0.2 MU/spot, 0.4 MU/spot, and 1 MU/spot.

The energy deposition and proton LET in the IC and water at the Skandion Clinic is calculated with a `Geant4` (Agostinelli et al. 2003) Monte Carlo model of the gantry and water phantom as detailed in Almhagen et al. 2018.

Measurements at the Danish Centre for Particle Therapy

The ProBeam Proton Therapy System (Varian Medical Systems, USA) at DCPT was used to irradiate the IC at 70 MeV, 150 MeV, 226 MeV, and 244 MeV. The dose-rate in the 72.8 MHz ProBeam system is adjusted with the dose-rate factor (DRF), where e.g. DRF = 0.2 for a given energy approximately corresponds to 1/5 of the dose-rate relative to DRF = 1.0. The dose-rate is varied for DRF = 0.2, 0.5, and 1.0 in the present work. The spot duration times extracted from logfiles last from 2.6 ms (for 244 MeV and DRF = 1.0) to 22 ms (for 70 MeV and DRF = 1.0). The dose-rate for DRF = 1.0 for 70 MeV is so low that the DRF was not decreased any further as the general recombination already was close to negligible.

The dose deposition and LET at DCPT during the experiments are calculated using an in-house developed gantry model based on the `Geant4` toolkit `TOPAS` (Perl et al. 2012).

V.2.2 Theory

The general recombination of low-LET beams is occasionally corrected with means of extrapolation, where the collection efficiency f is related to the polarization voltage V. The recombination in pulsed beams exhibit a linear behaviour when f^{-1} is plotted versus V^{-1}, whereas a linearity is observed for continuous beams for f^{-1} as a function of V^{-2}. The TVM is applicable for a continuous beam and defined as

$$k_s = \frac{\left(\frac{V_1}{V_2}\right)^2 - 1}{\left(\frac{V_1}{V_2}\right)^2 - \frac{Q_1}{Q_2}}, \tag{V.1}$$

where Q_i is the charge collected at polarization voltage V_i. The TVM, however, is based on the approximately uniform charge carrier distribution in photon and electron beams and its application to recombination in light ion beams has been demonstrated to be questionable (Palmans, Thomas, and Kacperek 2006; Rossomme, Horn, et al. 2017).

The Jaffé theory for initial recombination

Jaffé 1913, 1929 investigated the initial recombination in ionization chambers exposed to ions and deduced the collection efficiency as

$$f_{\text{Jaffe}} = \frac{y_1}{y_2} \exp(-y_1) \left[\text{Ei}(y_1 + \ln(1 + y_2)) - \text{Ei}(y_2)\right] \tag{V.2}$$

with

$$y_1 = \frac{8\pi D}{\alpha N_0}, \quad y_2 = \frac{2dD}{\mu b^2 E}, \quad \text{and} \quad N_0 = \frac{\text{LET}}{W}, \tag{V.3}$$

where Ei denotes the exponential integral, d is the distance between the collecting electrodes, E is the strength of the electric field parallel to the ion tracks, and N_0 is the linear ion density where W is the mean energy expended in air per formed ion pair taken from IAEA TRS-398. The recombination coefficient α, ion mobility μ, and diffusion constant D are listed in Christensen, Tölli, and Bassler 2016. Kaiser et al. 2012 demonstrated that the Gaussian track structure applied in the Jaffé theory gave a better agreement with experiments than traditional amorphous track structure models. The Gaussian track radius b is depending on the LET and is implemented as suggested by Rossomme, Horn, et al. 2017.

The Jaffé theory is used to compute the initial recombination correction factor $k_s^{\text{Jaffé}}$ in a Roos-type IC in figure V.1(a) for the 4 relevant proton energies over a wide range of voltages, where the LET_Φ at 2 cm water depth, corresponding to the effective point of measurement in the IC, is calculated with `Geant4`.

Separation of initial and general recombination

An approach to separate initial and general recombination in a continuous beam was suggested by De Almeida and Niatel 1986, generalized by Boutillon 1998, and later extended (Palmans, Thomas, and Kacperek 2006) to include temporal variations in the beam structure. With I_V denoting the ionization current at polarization voltage V, the initial and general recombination can be estimated by measuring the current at lower voltages $I_{V/n}$, where $n > 1$, as

$$\frac{I_V}{I_{V/n}} \approx 1 + (n-1)\frac{A}{V} + (n^2-1)\frac{m^2 g}{V^2} I_V, \tag{V.4}$$

where the second term on the right-hand side is the contribution from initial recombination and the third term represents the general recombination. m^2 is related to the general recombination while A is a geometrical parameter related to initial recombination. $g = d^4/(6v)$ for a plane-parallel chamber with electrode gap d and nominal IC volume v (Palmans, Thomas, and Kacperek 2006). After the parameters A and m^2 have been experimentally determined, the recombination correction factor in the Boutillon approach is estimated as

$$k_s^{\text{B}} \simeq 1 + \frac{A}{V} + \frac{m^2 g}{V^2} I_{V,\text{eff}}, \tag{V.5}$$

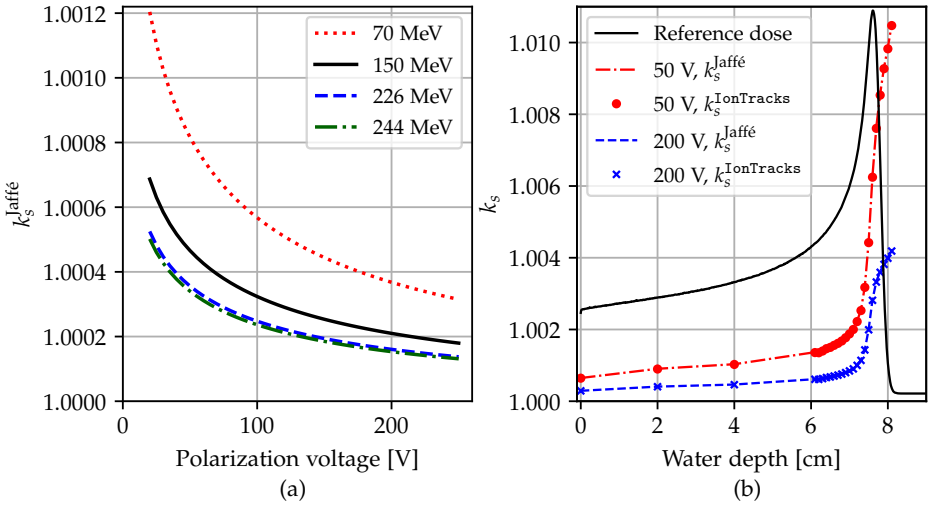

Figure V.1: (a) The correction for initial recombination as predicted by the Jaffé theory in a parallel-plate chamber with 2 mm electrode spacing for the relevant proton energies and chamber voltages. (b) The correction factor for initial recombination in the same air-filled IC along the central axis of a 100 MeV proton beam in water calculated with the Jaffé theory (lines) and `IonTracks` (markers) for 2 polarization voltages. The dose is shown in (b) for reference.

where $I_{V,\text{eff}}$ is the effective current in the IC at voltage V which is to be estimated through a combination of Monte Carlo calculations and dose measurements.

The contribution from initial recombination A/V, i.e. for small currents when the track overlap is insignificant, is traditionally regarded as a constant related to the IC (Boutillon 1998; Palmans, Thomas, and Kacperek 2006). However, the initial recombination varies with the proton energy along with several other factors, and the term A/V is in the present work assessed directly against the Jaffé theory through $A/V \approx k_s^{\text{Jaffé}} - 1$.

Numerical recombination calculations

The software `IonTracks` is able simulate the recombination in parallel-plate ICs by sampling ion tracks in time and space from distributions corresponding to a given dose-rate. `IonTracks` relies on amorphous track structure theory and models the density of charge carriers in a track as

$$n(r) = \frac{N_0}{\pi b^2} \exp\left(-\frac{r^2}{b^2}\right), \tag{V.6}$$

where r is the radial distance from the center, N_0 is given in eq. (V.3), and b is, as for the Jaffé theory, derived from Rossomme, Horn, et al. 2017 for a given proton LET. The movement of charge carriers in the IC in an electric field $\vec{E}$ is governed by

$$\frac{\partial n_{\pm}}{\partial t} = D\nabla^2 n_{\pm} \mp \mu \left(\vec{E} \cdot \vec{\nabla} n_{\pm} + n_{\pm} \vec{\nabla} \cdot \vec{E} \right) - \alpha n_{+} n_{-} \tag{V.7}$$

where $n_{\pm}$ denotes the densities of the positive and negative charge carriers respectively (Thomson 1899). The first term in the brackets corresponds to the charge carrier drift in the externally applied electric field whereas the last term in the brackets represents the space-charge screening of the charged particles exerted by neighbouring charge carriers. The space-charge screening effects in air are traditionally neglected for low-LET beams (Boag, Hochhäuser, and Balk 1996) corresponding to therapeutic relevant proton beams. The first term on the right-hand side is the charge carrier diffusion and the last a sink term corresponding to the recombination. `IonTracks` computes the recombination by solving eq. (V.7) subject to conditions given by the dose-rate and the ion track structures as modelled by eq. (V.6).

`IonTracks` is available for download along with an implementation of the Jaffé theory eq. (V.2) in a parallel-plate ionization chamber[1]. The LET_{Φ} along the central axis of a 100 MeV proton beam is used to calculate the initial recombination with `IonTracks` and the Jaffé theory in figure V.1(b) with geometrical parameters of a Roos-type IC. The LET_{Φ} is scored in water and converted to the electronic stopping power in air using `libdEdx` (Toftegaard et al. 2014).

V.3 Results and Discussion

V.3.1 Calculations of the effective dose-rates

The effective dose-rates in the ionization chamber exposed to the scanning proton beam as a function of dose-rate factor is shown in figure V.2 with typical standard uncertainties of 2 % as given in Liszka et al. 2018. The measurements with the Varian ProBeam at DCPT in figure V.2(a) show a linearly increasing dose-rate for an increasing DRF for the 150, 226, and 244 MeV energies. Thus, the recombination is expected to increase with the DRF.

The dose-rates of the Proteus-235 at the Skandion Clinic in figure V.2(b) exhibit a proportional increase with the number of MU/spot for the 150 MeV and 226 MeV energies until 0.4 MU/spot. However, the 70 MeV energy is relative constant as a function of MUs/spot as the system increased the spot duration time rather than the beam current. Consequently, the recombination is expected to be similar for the 70 MeV measurements at the Skandion Clinic.

[1] `https://github.com/jbrage/IonTracks`

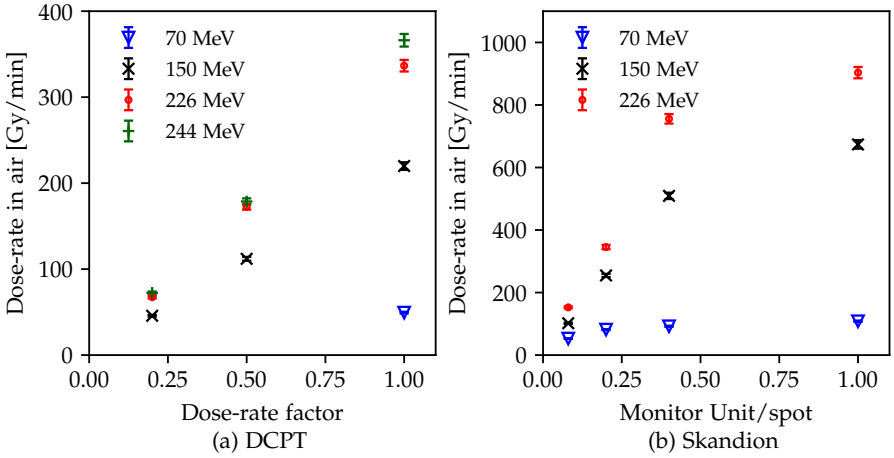

Figure V.2: The calculated effective dose-rates in the gas-filled IC as a function of the dose-rate variations at (a) DCPT and (b) the Skandion Clinic.

V.3.2 Recombination correction factors

Extrapolation and the TVM

An example of the charge collected in the IC during irradiation with 226 MeV protons at DCPT is shown in figure V.3 with 1 standard deviation statistical uncertainties. The collected charge is for each DRF normalized to the charge collected at 200 V where k_s, obtained from both linear and quadratic extrapolation, is given in each legend. The recombination correction factor obtained with quadratic extrapolation is however overall associated with huge uncertainties as shown in figure V.3(a) for all DRFs and energies and recombination correction methods.

The non-linearity of the recombination in figure V.3(a) as a function of the inverse voltage illustrates why the application of the TVM can be problematic: the Boag theory assumes a uniform charge carrier distribution with a linear relationship and the TVM may thus err in the present case. The inverse charge collection as a function of $1/V$ or $1/V^2$ in figure V.3 is representative for all measurements at DCPT and Skandion, and only the linear extrapolation as a function of $1/V^2$ in figure V.3(b) is used henceforth to extrapolate to k_s. The Jaffé theory in eq. (V.2) gives $k_s^{\text{init}} \simeq 1.0002$ for a 226 MeV proton in air at 200 V with electrode spacing $d = 0.2$ cm and $k_s^{\text{init}} \simeq 1.0004$ at 70 MeV with the same conditions as given in figure V.1(a).

The recombination correction factor is shown in figure V.4 for the linear extrapolation method and the TVM for each proton energy at 200 V polarization voltage. The Jaffé theory is used to estimate the initial recombination at 200 V which is plotted with horizontal dashed lines at each energy for reference. The

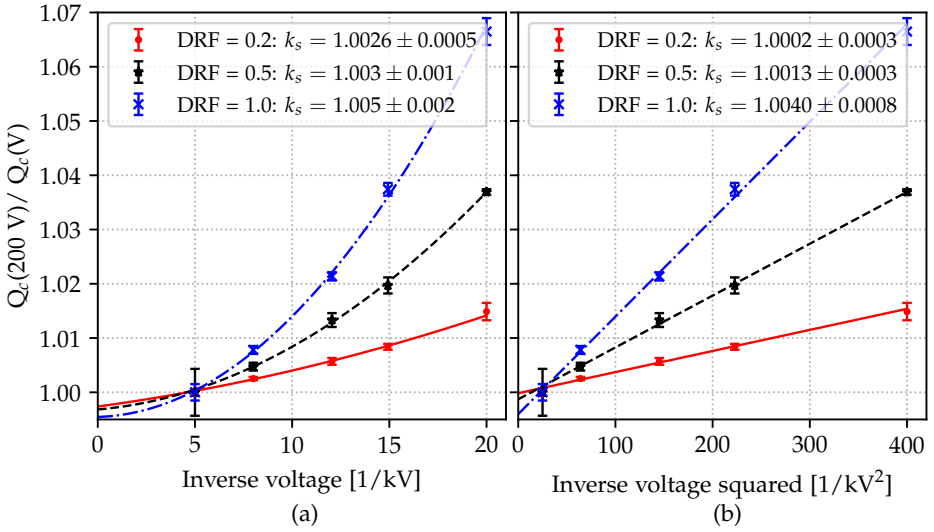

Figure V.3: The collected charge Q_c for the 5 voltages normalized to the charge collected at 200 V for 226 MeV protons at DCPT. The recombination correction factors k_s (with 1 standard deviation statistical uncertainties estimates from the fits) given in the legends are obtained from extrapolation using (a) a quadratic fit and (b) a linear fit.

plots for the measurements at DCPT in (a) and Skandion in (b) show that several of the k_s factors obtained with the linear extrapolation method are below the initial recombination contribution delineated. The discrepancy between k_s obtained with the TVM and linear extrapolation generally is of the order of 0.2 %.

The Boutillon approach

The relative collected charges as a function of the effective currents I_{eff} are shown in figure V.5 for the measurements at DPCT and Skandion. The Boutillon theory in eq. (V.4) is fitted to the data in each figure by minimizing the total least-square difference between the data and the fits. The initial and general recombination parameters obtained from each minimization is listed in table V.1. The initial recombination parameter A in the Boutillon formalism is compared to the initial recombination estimated with the Jaffé theory and estimates with two Roos-type chambers in a low-energy proton beam by Palmans, Thomas, and Kacperek 2006. Boutillon 1998 suggests a generic $A = 0.25$ value for photon beams, which is significantly larger than the initial recombination in proton beams as modelled in the Jaffé theory in eq. (V.2), which averaged over the relevant proton energies is $A = 0.041$ in a Roos-type chamber with collecting

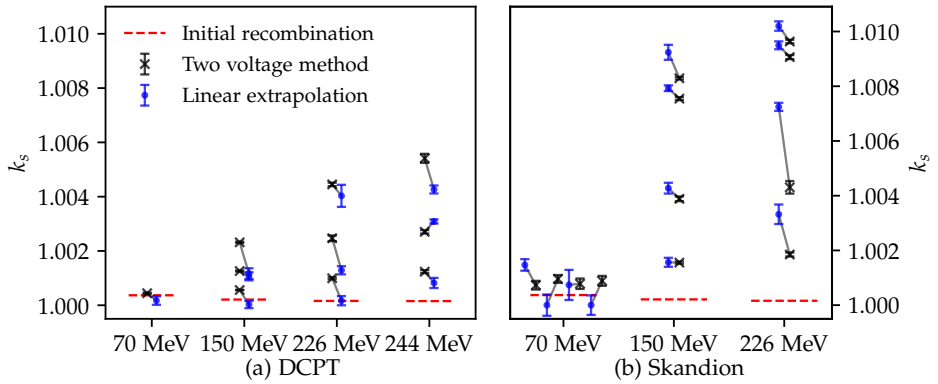

Figure V.4: The recombination correction factor k_s calculated with the TVM (crosses) and the linear extrapolation method (circles) at 200 V for all energies and dose-rates. The Jaffé theory for initial recombination is plotted for reference for each energy with horizontal dashed lines for each energy. Lines connect the k_s values obtained for the same energy and DRF to assist the eye. (a) The DCPT measurements contain for each energy—except for 70 MeV—the 3 DRFs. (b) The results from the Skandion Clinic for the 4 dose-rates for each proton energy with the same legend as in (a).

voltage of 200 V. The A values obtained at DCPT (for 150, 226, and 244 MeV) and Skandion (70, 150, 226 MeV) are both lower than the results presented by Palmans, Thomas, and Kacperek 2006 but larger than what the Jaffé theory predicts estimated as $k_s^{\text{Jaffé}} - 1$.

The general recombination parameter m^2 estimated from both the DCPT and Skandion data is, on the other hand, in good agreement with the values tabulated in by Palmans, Thomas, and Kacperek 2006.

V.3.3 Recombination versus dose-rate

The recombination correction factors with the Boutillon formalism with parameters listed in table V.1 are shown (with solid lines) for the DCPT data in figure V.6 and for the Skandion data in figure V.7. The Boutillon theory is compared to the recombination correction factors obtained with the TVM (shown with markers in each figure) calculated for a charge collected at 200 V relative to that at 67 V.

Both figures feature for comparison the theoretically calculated recombination correction factors obtained with `IonTracks` (dashed line), where the tracks were with a fluence-rate derived from the dose-rate and the Monte Carlo scored LET_Φ at 2 cm water depth. The Jaffé theory is in both figures plotted for the maximum (70 MeV) and minimum (226 MeV or 244 MeV) initial recombination

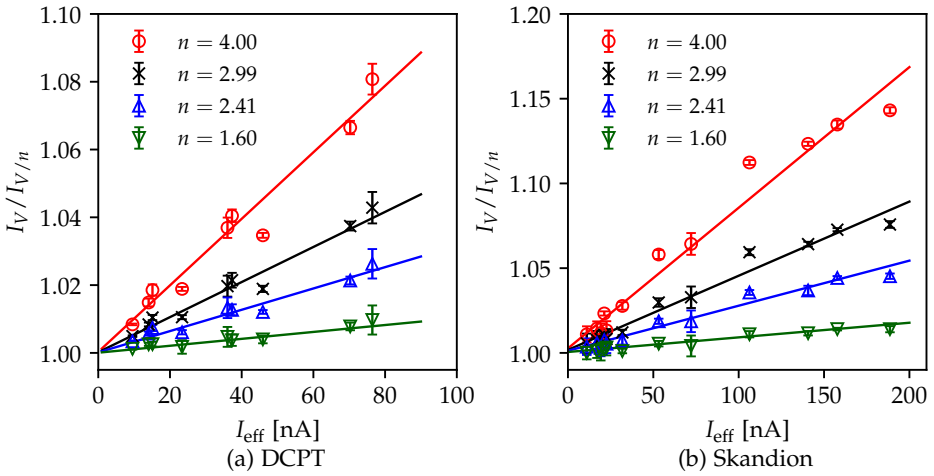

Figure V.5: Relative charge collection as a function of the effective current measured at (a) DCPT and (b) the Skandion Clinic. The Boutillon theory in eq. (V.4) has been fitted to all data in each case.

Table V.1: The initial recombination parameter (for $V = 200\,\text{V}$) in the Boutillon formalism estimated from the Jaffé theory and from measurements at DCPT and Skandion along with the general recombination parameter m^2. The listed standard uncertainties are estimated from the linear fits. The parameters are compared to the minimum and maximum values presented in Palmans, Thomas, and Kacperek 2006 obtained with two different Roos chambers.

	A [V]	g [µm]	m^2 [$\text{V}^2\,\text{nA}^{-1}\,\text{cm}^{-1}$]
Jaffé theory†	0.041	—	—
DCPT data	0.12 ± 0.02	7.62	$(3.4 \pm 0.7) \cdot 10^3$
Skandion data	0.11 ± 0.02	7.62	$(2.8 \pm 0.4) \cdot 10^3$
Literature	$0.35 - 0.46$	$6.63 - 6.86$	$(2.71 - 2.93) \cdot 10^3$

† Averaged over the 70, 150, 226, 244 MeV energies in the Roos-type chamber.

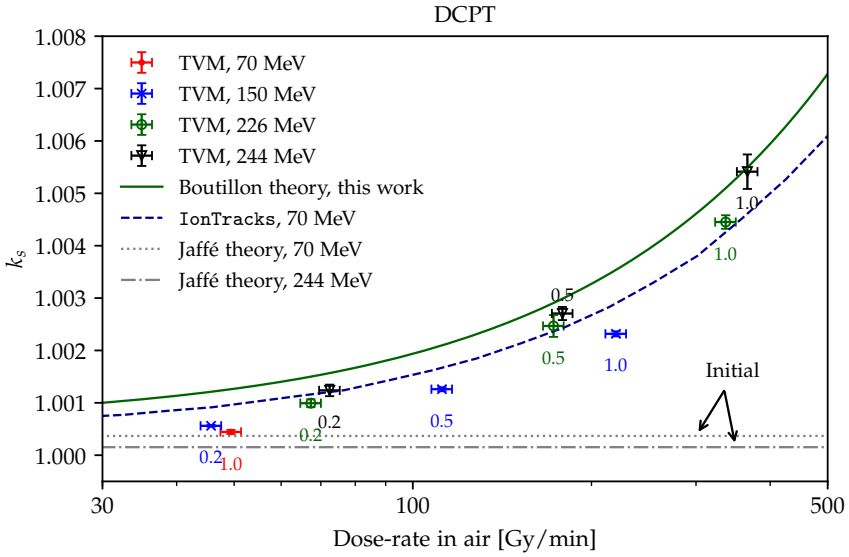

Figure V.6: The recombination correction factors k_s calculated with the TVM (markers) as a function of dose-rate in the IC for the DCPT measurements labelled with the DRF. The Boutillon theory (solid line) is plotted with the DCPT parameters listed in table V.1.

for reference at the 200 V polarization voltage.

The TVM agrees well with the Boutillon theory and `IonTracks` results above 200 Gy min^{-1} except for an outlier in the DCPT data for 150 MeV. However, the TVM seems to underestimate the recombination for low dose-rates, especially pronounced at the 70 MeV measurements at both DCPT and Skandion. The TVM calculated k_s values in both cases fall within 1-2 standard deviations of the initial recombination predicted by the Jaffé theory.

These results are in agreement with Rossomme, Horn, et al. 2017 where the TVM was demonstrated to err at low dose-rates with significant amounts of initial recombination. The TVM is, as shown in figure V.4, generally in good agreement with the extrapolation method. The linear extrapolation method, as the TVM, however seems to fail to predict the total recombination when the dose-rate is low and the general recombination is comparable to the initial recombination as observed for the lowest dose-rates for the 70, 150, and 226 MeV energies at DCPT and 70 MeV at Skandion.

Conclusion

The ion recombination in scanning proton beams at the Danish Centre for Particle Therapy and the Skandion Clinic is investigated with the Boutillon for-

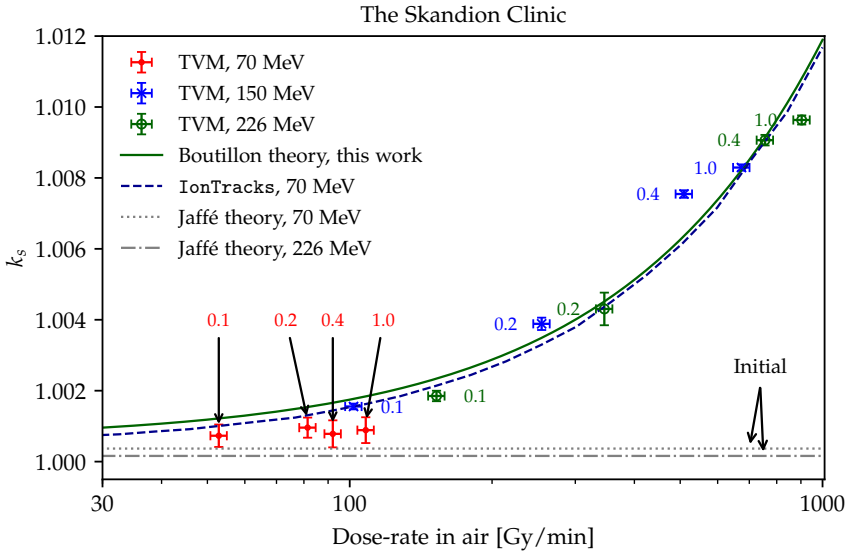

Figure V.7: The recombination correction factors k_s obtained with the TVM (markers) as a function of dose-rate in the IC for the Skandion measurements labelled with the MU-rate. The Boutillon theory (solid line) is plotted with the Skandion parameters listed in table V.1.

malism. The Boutillon theory enables a separation of initial and general recombination which is investigated for 70 MeV to 244 MeV and 45 Gy min^{-1} to 950 Gy min^{-1} dose-rates. The initial recombination parameter was found to be $A = (0.12 \pm 0.2)$ V at DCPT and $A = (0.11 \pm 0.2)$ V at Skandion, which is lower than previously reported values for photon and proton energies below 70 MeV but in better agreement with the Jaffé theory for initial recombination. The general recombination parameter was found to $m^2 = (3.4 \pm 0.7) \cdot 10^3$ V^2 nA^{-1} cm^{-1} with the DCPT data and $m^2 = (2.8 \pm 0.4) \cdot 10^3$ V^2 nA^{-1} cm^{-1} with the Skandion data, both in agreement with previously published results.

The recombination corrections predicted by the numerical approach `IonTracks` independently of the measurements were generally within 0.2 % agreement with the Boutillon formalism, hence validating the approach of computing the recombination based on amorphous track structure theory and a general diffusion-advection equation governing the movement and recombination of charge carriers in a parallel-plate IC.

The recombination correction factor k_s obtained with the two-voltage method was found to be in agreement with the theoretical `IonTracks` software and the Boutillon theory $\gtrapprox$ 100 Gy min^{-1}. However, the linear extrapolation method and the TVM underestimate the recombination below that threshold when the amount of initial recombination is comparable to the general recom-

bination, which is in agreement with previous findings in light ion beams.

The mapping of the recombination with the Boutillon formalism for the clinically relevant energies enables a general prediction of the correction factor k_s directly as a function of the dose-rate factor (the Varian system) or MU/spot (the IBA system) and proton energy.

References

Agostinelli S et al. (2003). `Geant4` – A simulation toolkit. *Nuclear Instruments and Methods in Physics Research, Section A* **506**(3), 250–303.

Almhagen E, DJ Boersma, H Nyström, and A Ahnesjö (2018). A beam model for focused proton pencil beams. *Physica Medica* **52**, 27–32.

Almond PR, PJ Biggs, BM Coursey, W Hanson, MS Huq, R Nath, and D Rogers (1999). AAPM's TG-51 protocol for clinical reference dosimetry of high-energy photon and electron beams. *Medical Physics* **26**, 1847–1870.

Andreo P, DT Burns, K Hohlfeld, MS Huq, T Kanai, F Laitano, V Smyth, and S Vynckier (2000). *Absorbed dose determination in external beam radiotherapy: an international code of practice for dosimetry based on standards of absorbed dose to water*. Vienna: International Atomic Energy Agency, Technical Report Series 398.

Boag JW (1950). Ionization measurements at very high intensities—Part I. *The British Journal of Radiology* **274**, 601–611.

Boag JW and J Currant (1980). Current collection and ionic recombination in small cylindrical ionization chambers exposed to pulsed radiation. *British Journal of Radiology* **53**(629), 471–478.

Boag JW, E Hochhäuser, and OA Balk (1996). The effect of free-electron collection on the recombination correction to ionization measurements of pulsed radiation. *Physics in Medicine and Biology* **41**(5), 885–897.

Boutillon M (1998). Volume recombination parameter in ionization chambers. *Physics in Medicine and Biology* **43**, 2061–2072.

Christensen JB, H Tölli, and N Bassler (2016). A general algorithm for calculation of recombination losses in ionization chambers exposed to ion beams. *Medical Physics* **43**(10), 5484–5492.

Cortés-Giraldo MA and A Carabe (2015). A critical study of different Monte Carlo scoring methods of dose average linear-energy-transfer maps calculated in voxelized geometries irradiated with clinical proton beams. *Physics in Medicine and Biology* **60**(7), 2645–2669.

De Almeida C and M Niatel (1986). *Comparison between IRD and BIPM exposure and air-kerma standards for cobalt gamma rays*. Sèvres: Bureau International des Poids et Mesures.

Greening JR (1964). Saturation characteristics of parallel-plate ionization chambers. *Physics in Medicine and Biology* **9**(2), 143–154.

Jaffé G (1913). Zur Theorie der Ionisation in Kolonnen. *Annalen der Physik* **347**(12), 303–344.

— (1929). Zur Theorie der Ionisation in Kolonnen II. *Annalen der Physik* **393**(7), 977–1008.

Kaiser FJ, N Bassler, H Tölli, and O Jäkel (2012). Initial recombination in the track of heavy charged particles: Numerical solution for air filled ionization chambers. *Acta Oncologica* **51**(3), 368–375.

Kanai T, M Sudo, N Matsufuji, and Y Futami (1998). Initial recombination in a parallel-plate ionization chamber exposed to heavy ions Initial recombination in a parallel-plate ionization chamber exposed to heavy ions. *Physics in Medicine and Biology* **43**, 3549–3558.

Liszka M, L Stolarczyk, M Klodowska, A Kozera, K Dawid, M Natalia, A Pedracka, MPR Waligorski, and P Olko (2018). Ion recombination and polarity correction factors for a plane–parallel ionization chamber in a proton scanning beam. *Medical Physics* **45**(1), 391–401.

Mie G (1904). Der elektrische Strom in ionisierter Luft in einem ebenen Kondensator. *Annalen der Physik* **318**(5), 857–889.

Palmans H, R Thomas, and A Kacperek (2006). Ion recombination correction in the Clatterbridge Centre of Oncology clinical proton beam. *Physics in Medicine and Biology* **51**(4), 903–917.

Perl J, J Shin, J Schumann, B Faddegon, and H Paganetti (2012). TOPAS: An innovative proton Monte Carlo platform for research. *Medical Physics* **39**, 6818–6837.

Rossomme S, J Hopfgartner, ND Lee, A Delor, RA Thomas, F Romano, A Fukumura, S Vynckier, and H Palmans (2016). Ion recombination correction in carbon ion beams. *Medical Physics* **43**(7), 4198–4208.

Rossomme S, J Horn, et al. (2017). Ion recombination correction factor in scanned light-ion beams for absolute dose measurement using plane-parallel ionisation chambers. *Physics in Medicine and Biology* **62**(13), 5365–5382.

Thomson J (1899). On the theory of the conduction of electricity through gases by charged ions. *The London, Edinburgh, and Dublin Philosophical Magazine and Journal of Science* **47**(286), 253–268.

Toftegaard J, A Lühr, N Sobolevsky, and N Bassler (2014). Improvements in the stopping power library `libdEdx` and release of the web GUI `dedx.au.dk`. *Journal of Physics: Conference Series* **489**(1), 012003.

DTU Nutech
Center for Nuclear Technologies
Technical University of Denmark
Risø Campus, Frederiksborgvej 399
DK-4000, Roskilde, Denmark

`http://www.nutech.dtu.dk/english`
Tel: (+45) 4677 4900